Hydrogen in the Nominally Anhydrous Phases and Possible Hydrous Phases in the Lower Mantle

by

Huawei Chen

A Dissertation Presented in Partial Fulfillment
of the Requirements for the Degree
Doctor of Philosophy

Approved May 2019 by the
Graduate Supervisory Committee:

Sang-Heon Shim, Chair
Edward Garnero
Mingming Li
Maitrayee Bose
Kurt Leinenweber

ARIZONA STATE UNIVERSITY

August 2019

ABSTRACT

The transport of hydrogen to the Earth's deep interior remains uncertain. The upper mantle minerals have a very low hydrogen solubilities (hundreds of ppm). The hydrogen storage capability in the transition zone minerals (2 wt%) is high compared to those of the upper mantle. The hydrogen storage in the lower mantle is not well known. The main minerals in the lower mantle bridgmanite and ferropericlase have very low hydrogen storage capacities (less than 20 ppm).

In order to further understand the hydrogen storage in the lower mantle, a series of experiments had been conducted to simulate the environment similar to the Earth's lower mantle.

The experiments with hydrous Mg_2SiO_4 ringwoodite (Rw) show that it converts to crystalline dense hydrous silica, stishovite (Stv) or $CaCl_2$-type SiO_2 (mStv), containing $\sim$1 wt% H_2O together with bridgmanite (Brd) and MgO at the pressure–temperature conditions expected for lower-mantle depths between approximately 660 to 1600 km. Brd would break down partially to dense hydrous silica (6–25 mol%) and (Mg,Fe)O in mid-mantle regions with 0.05–0.27 wt% H_2O.

The hydrous stishovite has a $CaCl_2$ structure, which is common among hydrous minerals in the lower mantle. Based on this observation, I hypothesize the existence of hydrous phases in the lower mantle. The experiments found a new hexagonal iron hydroxide (η-$Fe_{12}O_{18+x/2}H_x, x\simeq2$) between the stability fields of the ϵ- and pyrite-type FeOOH at 60–80 GPa and high temperature. The new phase contains less H_2O, limiting the H_2O transport from the shallow to the deep mantle in the Fe–O–H system.

Possible hydrogen storage in Ca-pervoskite was studied. CaPv could contain 0.5–1 wt% water and the water in CaPv could distort the crystal structure of CaPv from cubic to tetragonal structure.

In conclusion, hydrogen can be stored in hydrous stishovite in the shallower depth

lower mantle. At a greater depth, the new η phase and pyrite-type phase would take over the hydrogen storage. The role of CaPv in deep water storage need to be considered in future studies.

ACKNOWLEDGMENTS

The work of this dissertation would not have been possible without the guidance and support from a number of individuals. To begin with, I like to thank my advisors Sang-Heon Shim, Edward Garnero, Mingming Li, Maitrayee Bose and Kurt Leinenweber for their help over the last 5.5 years.

Secondly, I would like to thank Vitali Prakapenka, Eran Greenberg (APS) and Martin Kunz, Hans A. Bechtel (ALS) for giving us tremendous support in experiments. I want to acknowledge the help from Mingming Li, Shuxiang Zhou, Dane Morgan and Sheng-Yi Xie for Geodynamic or DFT calculation. I want to thank Depth of the Earth, SIMS, multi-anvil lab and the LeRoy Eyring Center for Solid State Science at Arizona State University.

Furthermore, I would like to thank my friends (Byeongkwan Ko, Shule Yu, Hongyou Lai, Helen Piet, Taehyun Kim, Harrison Allen-Sutter and many others) in Arizona State University and Yonsei University for the helpful discussions and generously sharing experimental data and ideas.

Many thanks to my wife Zixin Shi and my parents for their selfless support mentally and financially of these years.

H.C. was supported by the Keck Foundation (PI: P. Buseck). The results reported herein benefit from collaborations and/or information exchange within NASA's Nexus for Exoplanet System Science (NExSS) research coordination network sponsored by NASA's Science Mission Directorate.

TABLE OF CONTENTS

CHAPTER Page

LIST OF TABLES

LIST OF FIGURES

Figure Page

Figure Page

Chapter 1

INTRODUCTION

1.1 Composition of the Earth

Nucleo synthetic events are responsible to create the elements that forms the solar system. The composition of the Earth would be the same or similar to the chondrites that forms the Earth. From the study of meteorites, the composition of the Earth can be derived. The most abundant of elements in the Earth is oxygen, iron, magnesium and silicon, which make up about 90% of the total mass of the Earth (McDonough and Sun, 1995). The iron in the Earth represents most of the molten outer core and the solid inner core, which leave the mantle made of mostly magnesium, silicon.

We have direct samples from the crust of the Earth and top of the upper mantle. From the minerals of the upper mantle, we could also estimate the composition of the Earth by performing melting experiments. A.E. Ringwood estimated the upper mantle to be 60% olivine, 30% pyroxene and 10% garnet (Ringwood, 1975), which is also consistent with the composition made of magnesium, silicon, iron and oxygen.

For the deeper part of the Earth where we do not have direct samples to study, the composition has been assumed to be the same as upper mantle which is the peridotitic composition. Small changes in elemental ratio would affect the minerals assemblages in the deep mantle, for example, other possible composition was brought up in some other studies (Irifune *et al.*, 2008). The peridotitic model of the Earth are still representative of the mantle elements (Irifune *et al.*, 2008).

The trace elements in particular hydrogen has not been well constrained in the deep interior. The content of hydrogen in the deep interior vary from ppm to several

weight percent (Wittlinger *et al.*, 1997; Smyth *et al.*, 2003, 2006). It had not been well studied whether the trace elements would affect the mineralogy of the lower mantle.

1.2 Major Minerals in the Deep Interior

From the pyrolitic model of the Earth, the the mineralogy of the upper mantle is 60% olivine, 30% pyroxene and 10% garnet. Wadsleyite and ringwoodite are two major minerals in the transition zone depending on different depth (Frost, 2008). Garnet and Ca-pervoskite could also be stable at the transition zone (Frost, 2008). The lower mantle contains bridgmanite, ferropericlase and Ca-pervoskite (Kesson *et al.*, 1998a). Bridgmanite transforms to a post pervoskite phase at about 120 GPa and 2000 K (Murakami *et al.*, 2004). The outer core and inner core is made of iron-nickel alloy while some light elements likely exist there (Birch, 1952).

1.3 Water Content in the Deep Interior

The upper mantle contains less than 200 ppm water (Wittlinger *et al.*, 1997). The major mineral olivine and pyroxene had limited water solubility at mantle related pressure and temperature (Smyth *et al.*, 2003). The transition zone minerals– wadsleyite and ringwoodite– could contain large amount of water up to 3 wt% (Ye *et al.*, 2012, 2010). Bridgmanite and ferropericlase in the lower mantle had extremely low water solubility up to 20 ppm (Bolfan-Casanova *et al.*, 2003). The water content in Ca-pervoskite has not been well studied. Several possible hydrous phases had been synthesized in the experimental high pressure and temperature condition. For example, hydrous stishovite, phase D and phase H have been synthesized in the pyrolitic + water composition (Nishi *et al.*, 2014; Frost and Fei, 1998; Spektor *et al.*, 2011). These hydrous phases greatly expand possible water content in the lower mantle. However, the condition and possible existence of those phases at the lower mantle pressure and

temperature condition.

1.4 Laser Heated Diamond Anvil Cell

Diamond anvil cell could generate pressure up to 300 GPa (Loubeyre *et al.*, 2002). Two diamond anvils are glued to the seats and face oppositely in the diamond anvil cell. A rhenium gasket is placed in between two diamonds. The sample chamber is made by drilling a 90 or 120 μm diameter hole in a rhenium gasket indented by diamond anvils. Samples are placed in the chamber. We use pressure medium to fill into the empty space in the sample chamber. Ar or Ne were used as pressure medium for most experiments in the thesis. For some runs, water was used as a pressure medium.

Two infrared laser beams with a wavelength of $\sim$1 μm are focused on the sample through two opposite sides of DAC with a hot spot size of 20–25 μm diameter. Temperatures for laser heating are calculated by fitting the measured thermal radiation spectra to the Planck equation from both sides of the sample after subtracting backgrounds. We maintained the same temperature for both sides of sample by adjusting laser power.

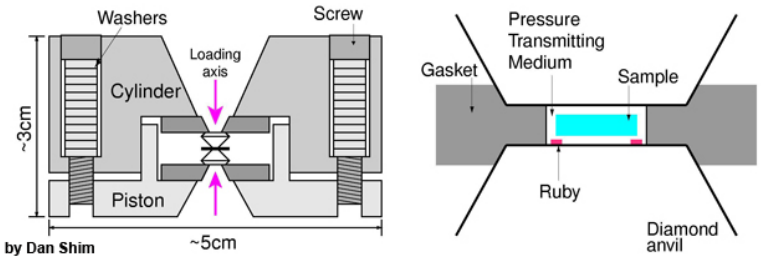

Figure 1.1: Scheme of Diamond Anvil Cell.

Original image from Sang-Heon Shim, ASU

1.5 Synchrotron X-ray Diffraction

X-ray diffraction provide information about phase identification and mineralogical portion in the samples. We used Rietveld refinement to identify and analyze the diffraction patterns. For a given mineral or solid phase, the X-ray diffraction pattern is measured at given pressure and temperature, which can be used for phase identification. The changes in X-ray diffraction pattern with pressure can be used to study the compressibility of the phase. We conducted synchrotron X-ray diffraction (XRD) experiments at beamlines 13IDD at APS and 12.2.2 at ALS (Prakapenka *et al.*, 2008b; Kunz *et al.*, 2005). We conducted XRD measurements during laser heating at the beamlines. We collected diffraction patterns from a monochromatic X-ray beam with a wavelength of either 0.3344, 0.4133, or 0.4959 Å. The sizes of the X-ray focus at the sample were 3×4 and 10×10 μm^2 at beamlines 13IDD and 12.2.2, respectively. Diffraction patterns were measured with MarCCD and Pilatus detectors at beamlines 12.2.2 and 13IDD, respectively. We integrated the measured diffraction images to 1D patterns in the Dioptas package (Prescher and Prakapenka, 2015). We performed phase identification and peak fitting in the PeakPo package (Shim, 2017).

1.6 Overview of the Thesis Chapters

The uncertainty of the deep water storage largely comes from the lower mantle. For studying water content in the lower mantle, it is important to fix starting water content. In chapter 2, we used multi–anvil press to synthesize hydrous ringwoodite with about 1 wt% water content. We then used the ringwoodite sample to study possible hydrogen storage in the lower mantle condition. We found that stishovite could be potential hydrogen storage phase in the lower mantle , which would requrie the breakdown of bridgmanite in the lower mantle condition. Thus under 1 wt%

water or relative low water content, hydrous stishovite rather than hydrous phases would be an important water storage phase to consider.

In chapter 3, we study the hydrogen storage in Fe-O-H system. We found that even though FeOOH could contain about 10 wt% water at high pressure condition. At 60–80 GPa, most of the water will be lost in this system due to a phase transition. A new phase with the composition $H_2Fe_6O_{19}$ can greatly impact the possible water storage in this Fe-O-H system.

In chapter 4, we study the crystal structure and possible water content in pyrite type PtO_2. The possible hydrogen storage in the pyrite type FeOOH is key to constrain deep hydrogen storage. We showed that similar to pyrite type FeOOH, pyrite type PtO_2 can have varying water storage depending on temperatures. The hydrogen storage properties is likely related to the varying oxidation state of Pt and Fe.

In chapter 5 and 6, we study the crystal structure and possible water content in Ca-pervoskite (CaPv). The crystal structure of CaPv is still under debate at mantle related pressure and temperature conditions. We used high resolution X-ray diffraction to study both cubic and tetragonal CaPv. We also started with water bearing Ca-silicate samples and we found that water could distort the crystal structure of CaPv even at mantle related temperatures, making it a possible hydrogen storage phase in the lower mantle. The possible water content in CaPv is about 0.5–1 wt%.

Chapter 2

STABILIZATION OF DENSE SILICA PHASE IN HYDROUS MID-MANTLE REGIONS

2.1 Introduction

Lines of evidence (Shim *et al.*, 2001, 2017; Kurnosov *et al.*, 2017) support that the lower mantle has a similar chemical composition to the upper mantle, that is pyrolite (McDonough and Sun, 1995). In a pyrolitic lower mantle, (Mg,Fe)(Al,Si)O_3 bridgmanite (Brd) and (Mg,Fe)O ferropericlase (Fp) are the dominant minerals (Kesson *et al.*, 1998a; Lee *et al.*, 2004). The high Mg/Si ratio of pyrolite stabilizes (Mg,Fe)O as a mineral phase (Fp) in the region. Fp would react with a free silica phase and forms Brd: (Mg,Fe)O (Fp) + SiO_2 $\rightarrow$ (Mg,Fe)SiO_3 (Brd). Therefore, it is believed that dense silica phases, such as stishovite (Stv), are not thermodynamically stable in the lower mantle.

In contrast, numerous studies have documented Stv coexisting with (Mg,Fe)O and Brd (pyroxene with a Brd-like composition) as inclusions in diamonds from the lower mantle (Kaminsky, 2012; Stachel *et al.*, 2005; Litvin *et al.*, 2014). Because the pyrolite model cannot explain the co-existence of Stv and (Mg,Fe)O, the diamond inclusions raise an important question about the mineralogy and composition of the lower mantle (Kaminsky, 2012). Alternatively, the inclusions may originate from non-pyrolitic sources. For example, Stv can exist with (Mg,Fe)O in a system with a much higher Fe content than pyrolite (Fei *et al.*, 1996). However, many of the (Mg,Fe)O inclusions do not have sufficient Fe for this scenario, and so Brd should be observed instead of Stv in those cases. Experiments have shown that subducted

basalt contains Stv together with Brd but not with Fp at the lower-mantle pressure–temperature (P–T) conditions (Hirose *et al.*, 2005a). Therefore, this cannot explain the diamond inclusion observations.

An important factor to consider is the possible presence of H_2O. Studies have shown that minerals in the mantle transition zone can store H_2O up to a few wt% (Smyth, 1994; Hirschmann, 2006; Pearson *et al.*, 2014). Indeed, some diamond inclusions indicated the premise that the mantle transition zone is hydrated at least locally (Pearson *et al.*, 2014; Tschauner *et al.*, 2018). However, recent high-pressure experiments have shown very low H_2O storage capacities for Brd and Fp in the lower mantle (Bolfan-Casanova *et al.*, 2003; Panero *et al.*, 2015). Therefore, H_2O transport via mantle convection across such a dramatic change in the H_2O storage capacity at 660-km depth can induce some important changes in the mineralogy of the lower mantle (Schmandt *et al.*, 2014; Tschauner *et al.*, 2018).

To understand the effect of H_2O on lower-mantle mineralogy, we have conducted laser-heated diamond-anvil cell (LHDAC) experiments on a synthetic hydrous ringwoodite (Mg_2SiO_4 with 1.1±0.5 wt% H_2O; hRw) starting material at the P–T conditions expected for the lower mantle (Method).

2.2 Methods

We synthesized Mg_2SiO_4 ringwoodite (Rw) from a molar mixture of forsterite, SiO_2 (glass), and brucite for synthesis of a Mg_2SiO_4 with 3 wt% H_2O in a 6-8 multi-anvil press combined with a 10/5 assemblies at Arizona State University (ASU) (Leinenweber *et al.*, 2012). The starting mixture was loaded into a platinum capsule. We compressed the mixture to 20 GPa and subsequently heated to 1573 K for 30 minutes. After the synthesis, pure ringwoodite was confirmed from X-ray diffraction (XRD). From infrared (IR) spectra, we obtained 1.1±0.5 wt% H_2O for

the amount of H_2O in Rw following the methods in (Smyth *et al.*, 2003) (Fig. 2.4b).

A powdered form of the hydrous Rw sample was pressed to a foil and loaded into a symmetric diamond-anvil cell (DAC). We used diamond anvils with 200 μm (flat) and 150 μm (beveled) cullets for experiments at pressures below and above 50 GPa, respectively. The sample chamber was made by drilling a 90 or 120 μm diameter hole in a rhenium gasket indented by diamond anvils. For the CO_2 laser heating experiments, we cryogenically loaded an Ar medium in a DAC. A ruby chip was loaded at the edge of the sample chamber for pressure measurements, but away from the sample foil in order to avoid any chemical reaction. We compressed the samples with type-II diamond anvils and focused a CO_2 laser beam on the sample foil in the DAC. Single-sided heating was conducted at 1200 to 2420 K using a laser heating system at ASU. Note that we did not mix the ringwoodite powder with any metals in the CO_2 heating experiments, because silicate samples couple directly with the CO_2 laser beam. The size of the laser heating spot was $\sim$50 μm. Temperatures were calculated by fitting the measured thermal radiation spectra to the Planck equation from one side of the sample after the subtracting backgrounds from optics in the system. Pressure was measured using the ruby fluorescence line shift or the first-order Raman mode from the tips of the diamond anvils (Mao *et al.*, 1978; Akahama and Kawamura, 2006). For the NIR measurements, we mixed the Rw starting material with 10 wt% Pt. Platinum was mixed for the laser coupling and internal pressure standard (Ye *et al.*, 2017). We loaded Ne as a pressure medium using the gas-loading system at the GSECARS, APS(Rivers *et al.*, 2008). The NIR laser heating was conducted at GSECARS(Prakapenka *et al.*, 2008b). Two near-infrared laser beams ($\sim$1 μm wavelength) were focused on the sample through two opposite sides of DAC with a hot spot size of 20–25 μm^2. The laser beams were aligned co-axially with the X-ray beam. Temperatures were calculated by fitting thermal radiation spectra to

the Planck equation from both sides of the sample after subtracting backgrounds.

We conducted synchrotron X-ray diffraction (XRD) experiments at beamlines 13IDD at APS and 12.2.2 at ALS (Prakapenka *et al.*, 2008b; Kunz *et al.*, 2005). For the samples heated with a CO_2 laser beam at ASU, we conducted the measurements at high pressure and 300 K. In the case of the NIR heating, we conducted XRD measurements during laser heating at the beamlines. We collected diffraction patterns from a monochromatic X-ray beam with a wavelength of either 0.3344, 0.4133, or 0.4959 Å. The sizes of the X-ray focus at the sample were 3×4 and 10×10 μm^2 at beamlines 13IDD and 12.2.2, respectively. Diffraction patterns were measured with MarCCD and Pilatus detectors at beamlines 12.2.2 and 13IDD, respectively. We integrated the measured diffraction images to 1D patterns in the Dioptas package (Prescher and Prakapenka, 2015). We performed phase identification and peak fitting in the PeakPo package (Shim, 2017). The data obtained from the GSECARS and the 12.2.2 beamlines agreed well with each other. Rietveld refinements were performed using the GSAS-II package (Toby and Von Dreele, 2013). We refined phase fractions first, then atomic positions, lattice parameters and spherical harmonic terms for the preferred orientation. After reaching a good visual fit, we refined all the parameters together to further reduce residuals after background subtraction, $R_{wp-bknd}$ (Fig. 2.2).

We conducted IR measurements on hydrous Rw starting material and the recovered samples (Fig. 2.4b) at beamlines 1.4 of ALS and U2A of NSLS-II. At ALS, the system consists of a Nicolet Magna 760 FTIR spectrometer and custom IR microscope with a HgCdTe detector and KBr beamsplitter. At U2A, we used a Bruker Vertex 80v FTIR spectrometer and Hyperion 2000 microscope with HgCdTe detectors. Spectral resolution was 4 cm^{-1}. Spectra were recorded for 256 scans. The beam-size was ∼10 μm at the sample. We conducted spectral fitting for the IR data using the LMFIT package (Newville *et al.*, 2016).

We performed geodynamic modeling to understand the effects of the reduced density of hydrated slabs in the mid mantle. The equations of the conservation of mass, momentum, and energy were solved under the Boussinesq approximation using the Citcom code (Moresi and Solomatov, 1995). The models were in 2D Cartesian, with an aspect ratio of 2:1. The model domain was divided into 512×256 (horizontal × vertical) elements, leading to a spatial resolution of approximately 11 km. Both the top surface and the bottom (i.e., the core-mantle boundary, CMB) of the models were free-slip, and the periodic boundary condition was employed for side boundaries. The temperature boundary condition was $T = 0$ on the top surface, and we used zero heat flux from the CMB. Our models were 100% internally heated with an internal heating rate of $Q = 20$ (non-dimensional). In this model setup, we choose to suppress the formation of hot mantle plumes from the CMB. The reasons were (1) we focus on the effects of subducting slabs and (2) the sheet-like geometry of plumes in 2D models is not realistic. Initially, the whole mantle has a temperature of $T = 0.6$, except at the center of the models where we introduced a 'cold slab' to drive initial convection, which extends from the surface to the CMB with a homogeneous temperature of $T = 0.4$ and a thickness of 180 km. However, the effects of initial condition were lost quickly and were not our focus in our study. The mantle viscosity depends on both temperature and depth, which is expressed as $\eta = \eta_0 \exp[A(0.5 - T)]$, where $A = 6.91$ is the activation coefficient which leads to changes in viscosity less than $1,000\times$ due to temperature changes, and $\eta_0 = 1.0$ and 30.0 for the upper mantle and the lower mantle, respectively. We performed simulations for six different cases. The Rayleigh numbers (Ra) for cases 1, 3 and 5 were 1×10^7, 5×10^7 and 1×10^8, respectively, while other parameters were the same in these cases. Cases 2, 4 and 6 had the same parameters as cases 1, 3, and 5, respectively, but we made the slabs neutrally buoyant in these cases at 660 to 1600 km depths. For each depth, the slabs

are defined in regions where the temperature satisfies:

$$T < T_{bg} - f(T_{bg} - T_{min}), \tag{2.1}$$

where T_{bg} is the background mantle temperature which is similar to the horizontally averaged temperature T_{avg} at a given depth, but excludes hot regions with $T > T_{avg}$, and T_{min} is the minimum temperature. $f = 0.1$ is a constant which sets the threshold temperature for slabs. Our criteria for defining slabs leads to a slab thickness of approximately 100 to 150 km in the upper mantle for most of the time.

2.3 Results and Discussion

Ringwoodite has an Mg/Si ratio of 2. Thus, heating converts Rw to Brd ($MgSiO_3$) and MgO (periclase, Pc) without silica at the P–T conditions expected for the lower mantle (Shim *et al.*, 2001). All the diffraction patterns we measured after CO_2 laser heating between 35 and 55 GPa, however, showed the peaks of silica (either Stv or its orthorhombic modification in $CaCl_2$ type structure, mStv) together with those of Brd and MgO (Fig. 2.1a,b and Fig. 1.1). The most intense diffraction line of Stv and mStv exists at 2.8–2.9 Å. Because Brd and MgO do not have diffraction lines at the range, the appearance of the intense silica line allows us to unambiguously identify Stv or mStv. In addition, some high-angle lines of Stv or mStv were identified, such as 101, 211, and 220. However, those features are less unambiguously as diagnostic features because of possible overlaps with the Brd and MgO lines. We also found Stv (or mStv) together with Brd and MgO in the NIR heating experiments. The indirect heating of the silicate samples in NIR laser heating resulted in larger thermal gradient across the sample. Given those conditions, we focused on the CO_2 laser-heating results for detailed analysis.

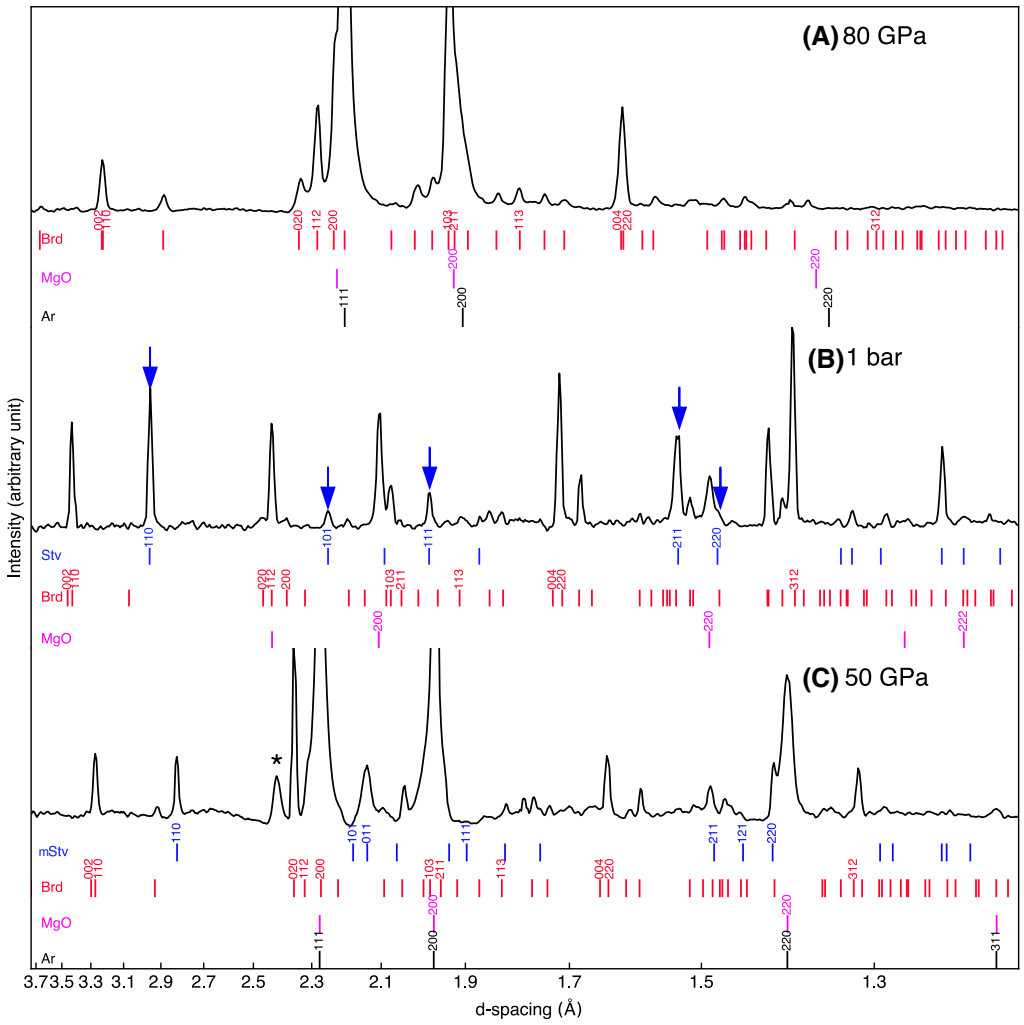

Figure 2.1: High-pressure X-ray Diffraction Patterns of Lower-mantle Minerals Transformed From Hydrous Ringwoodite.

a, a separate sample at 80 GPa after laser heating to 2179 K (X-ray wavelength of 0.4133 Å) b, 1 bar after recovery (X-ray wavelength of 0.3344 Å) and c, 50 GPa after heating at 1200 K. The colored ticks below the patterns indicate the expected peak positions (Brd: bridgmanite, Pc: periclase (MgO), Stv: stishovite, Ct-SiO_2: $CaCl_2$-type silica (or mStv), Ar: argon, $*$: hcp-Ar. The blue arrows highlight the peaks from Stv (or convered from mStv). The Miller indices are provided for the lines with significant intensities ($\geq$10%). Diffraction patterns at different pressures are presented in Fig. 1.1.

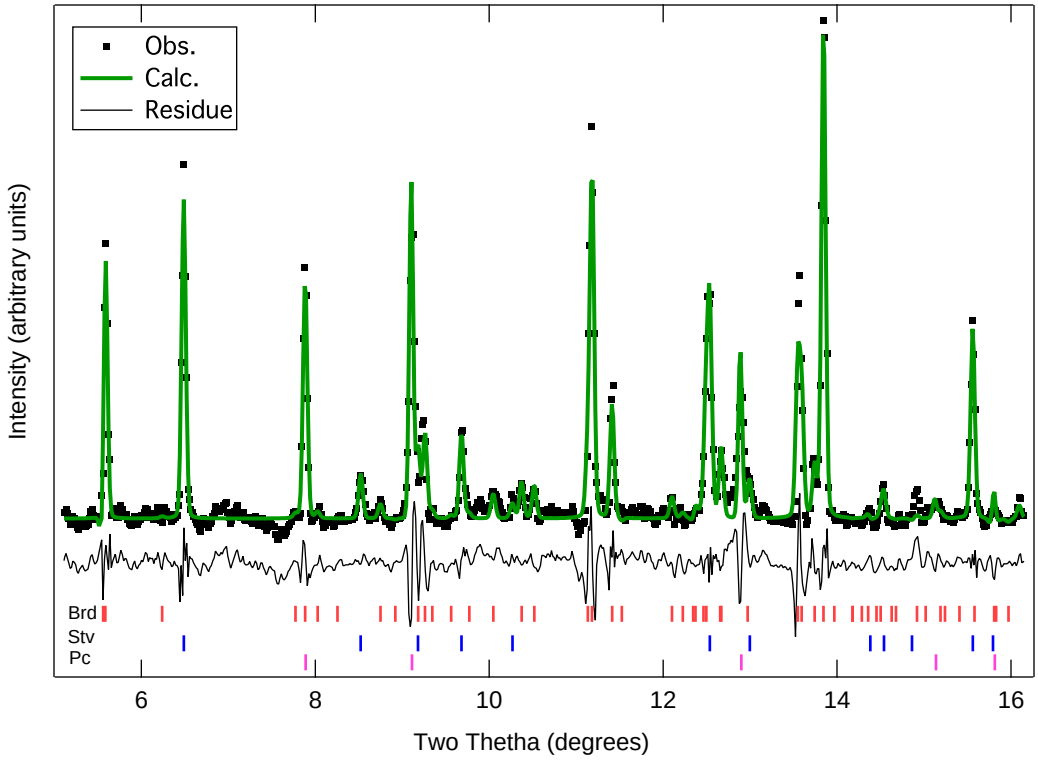

Figure 2.2: A Rietveld Refinement Result for the X-ray Diffraction Pattern of the Sample Recovered after Synthesis at 50 GPa 1200 K.

The squares are the measured diffraction intensities. The green line is the calculated diffraction pattern after fitting in the GSAS-II software. The black line is fit residue after the Rietveld refinement. The wavelength of the X-ray beam is 0.3344 Å. The fit residue ($R_{\mathrm{wp-bgnd}}$) is 2.98%.

We have successfully quenched most of the samples synthesized at 35–55 GPa and measured their diffraction patterns at 1 bar (Fig. 2.1 and Figs 2.2 and 2.3). All three phases observed at high pressure, Stv, Brd, and MgO, remained present after the pressure quench. The diffraction lines of silica were indexed well with the tetragonal

rutile type, that is Stv. The unit-cell volumes of Brd and MgO at 1 bar were in agreement with their anhydrous counterparts within ±1.0‰ (Tab. 2.2). However, for Stv, we found much larger unit-cell volumes than the value reported for anhydrous Stv by 1.7–5.2‰.

Table 2.1: Conditions and Run Products of the High-pressure Experiments. Pressure was calculated from the equations state of Ar (Errandonea *et al.*, 2006) and Pt (Dorogokupets and Dewaele, 2007) for the CO_2 and NIR laser heated samples, respectively.

Run number	Pressure (GPa)	Temperature (K)	Synthesized phases	H_2O content in silica (wt%)
		CO_2 laser heating		
517	35(1)	1870(100)	Stv, Brd, Pc	0.36(13)
203	37(1)	1930(100)	Stv, Brd, Pc	0.77(14)
604	43(1)	2116(100)	Stv, Brd, Pc	1.26(18)
717	44(1)	1630(100)	Stv, Brd, Pc	1.09(16)
331	50(2)	1200(100)	mStv, Brd, Pc	0.60(15)
302	55(2)	2080(100)	mStv, Brd, Pc	1.19(19)
803	65(3)	1740(100)	Brd, Pc	
408	80(4)	2179(100)	Brd, Pc	
571	94(5)	2420(100)	Brd, Pc	
		NIR laser heating		
111a	29(1)	1552(100)	Stv, Brd, Pc (Rw)	
111b	33(1)	1770(100)	Stv, Brd, Pc (Rw)	
111c	35(1)	2028(100)	Stv, Brd, Pc (Rw)	
312a	37(1)	1700(100)	Stv, Brd, Pc (Rw)	
312b	38(2)	1840(100)	Stv, Brd, Pc (Rw)	
312c	40(2)	1700(100)	Stv, Brd, Pc (Rw)	
433a	53(3)	1700(100)	mStv, Brd, Pc (Rw)	
433b	58(3)	1990(100)	mStv, Brd, Pc (Rw)	
433c	59(3)	2300(100)	mStv, Brd, Pc (Rw)	

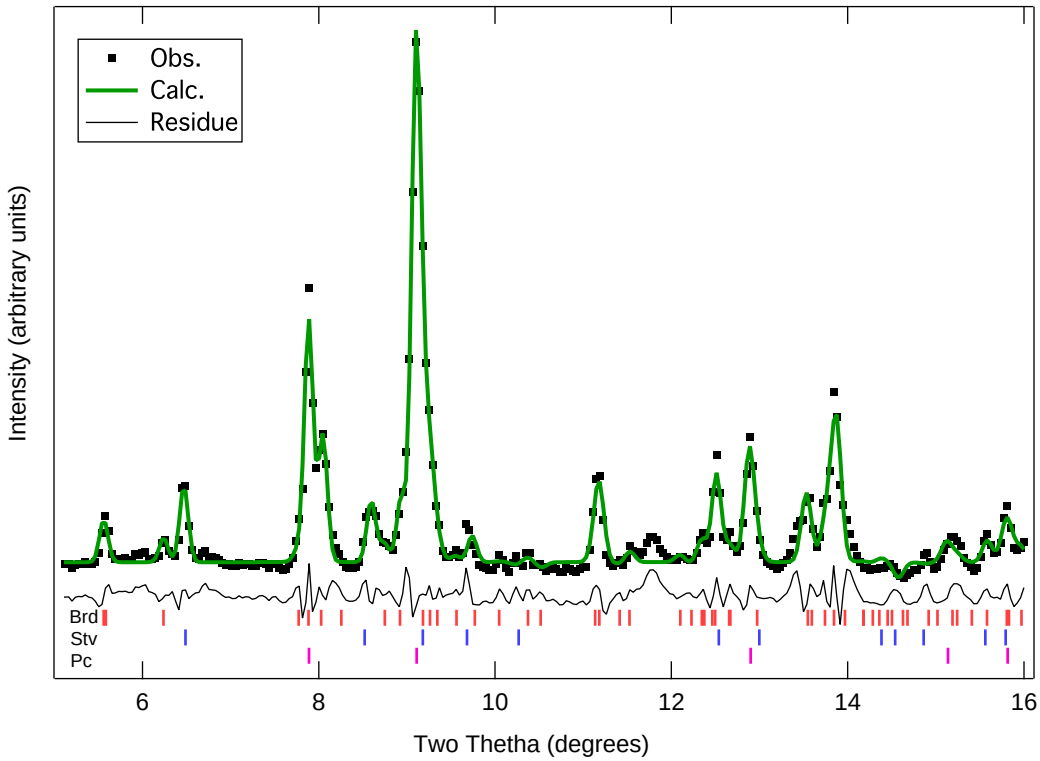

Figure 2.3: A Rietveld Refinement Result for the X-ray Diffraction Pattern of the Sample Recovered after Synthesis at 55 GPa 2080 K.

The squares are the measured diffraction intensities. The green line is the calculated diffraction pattern after fitting in the GSAS-II software. The black line is fit residue after the Rietveld refinement. The wavelength of the X-ray beam is 0.4133 Å. The fit residue ($R_{\mathrm{wp-bgnd}}$) is 3.5%.

Table 2.2: The Unit-cell Volumes of Bridgmanite (Brd), Periclase (Pc), And Stishovite (Stv) Measured at 1 Bar after Pressure and Temperature Quench.

The unit-cell parameters of Brd, Pc, and Stv are compared with those reported for pure $MgSiO_3$ (162.349 Å^3), MgO (74.778 Å^3), and anhydrous Stv (46.502 Å^3), respectively, at 1 bar (Ross and Hazen, 1990; Dorogokupets and Dewaele, 2007; Andrault *et al.*, 2003).

Run	P (GPa)	T (K)	Brd	$\Delta V/V$ (‰)	Pc	$\Delta V/V$ (‰)	Stv	$\Delta V/V$ (‰)
302	55	2080	162.47(7)	0.7(3)	74.75(4)	−0.2(3)	46.74(1)	5.2(1)
203	37	1930	162.31(6)	−0.2(1)	74.83(1)	0.7(1)	46.66(3)	3.4(7)
331	50	1200	162.35(6)	0.0(2)	74.82(3)	0.7(2)	46.63(3)	2.7(7)
517	35	1870	162.48(9)	0.8(5)	74.76(6)	−0.2(6)	46.58(3)	1.7(6)
604	43	2116	162.40(6)	0.3(1)	74.73(1)	−0.6(1)	46.74(2)	5.2(3)
717	44	1630	162.36(8)	0.0(3)	74.86(2)	1.0(2)	46.72(2)	4.7(4)

Incorporation of H_2O increases the unit-cell volume of Stv and the relationship between the H_2O content and the volume expansion was measured quantitatively(Nisr *et al.*, 2017a; Spektor *et al.*, 2011, 2016a). From the volume and H_2O content relationship found in other studies (Spektor *et al.*, 2016a; Nisr *et al.*, 2017b), we obtained 0.4–1.3 wt% H_2O for the recovered Stv (Tab. 2.1).

Stishovite has a tetragonal unit cell with two independent lattice parameters, a and c. When Stv is hydrated, the a-axis expands while the c-axis remains essentially unchanged. Such changes could be related to the bonding of hydrogen to the underbonded oxygen in the silicon defects in the crystal structure (Spektor *et al.*, 2011; Nisr *et al.*, 2017b). We found a strong linear correlation between the c/a ratio and the unit-cell volume of the recovered Stv (Fig. 2.4a). The trend in our dataset is in agreement with that found in previous studies on hydrous Stv (Spektor *et al.*, 2011, 2016a).

Infrared (IR) spectroscopy is sensitive to even a trace amount of hydroxyl incorporated in the crystal structures of mineral phases (Rossman, 1996). We measured the IR spectra of the samples recovered from the CO_2 lasers where we found complete conversion to the lower-mantle mineral phases, and did not find any Rw diffraction peaks after heating. We found multiples of OH vibrational modes from the recovered samples (Fig. 2.4b). The detected modes are significantly different from those of hRw (our starting material), MgO, and Brd in both wavenumber and intensity distribution (Pearson *et al.*, 2014; Panero *et al.*, 2015; Bolfan-Casanova *et al.*, 2002, 2003).

H_2O can significantly reduce the transition pressure of Stv to its orthorhombic modification (the $CaCl_2$ type, mStv), for example from ∼55 GPa to ∼25 GPa by 3 wt% H_2O (Lakshtanov *et al.*, 2007b; Nisr *et al.*, 2017a). However, the differences in diffraction pattern between the phases are subtle, particularly if the incorporated H_2O contents are low. In some diffraction patterns, we were able to identify some

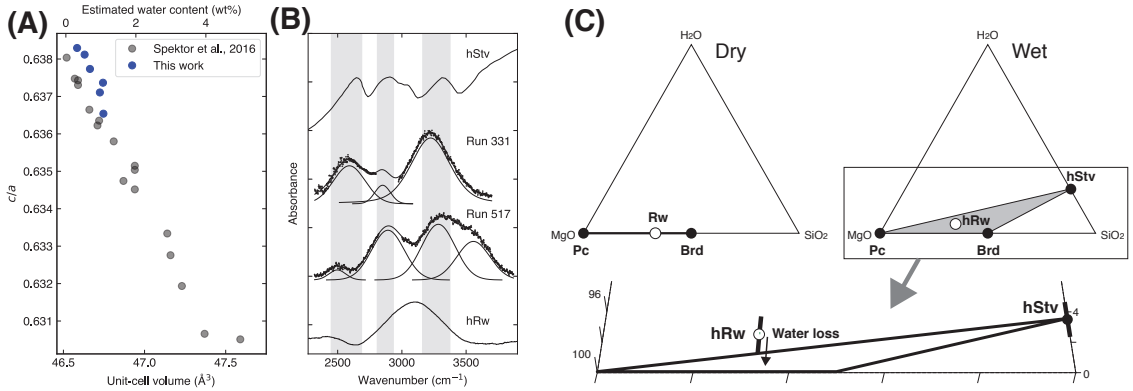

Figure 2.4: H_2O Solubility in Stv (or Mstv) and Its Effects on the Lower-mantle Mineralogy.

a, The c/a ratio and the unit-cell volume of the recovered Stv co-existing with Brd and MgO. For comparison, we plot the data for hydrous Stv (Spektor *et al.*, 2016a). b, The IR spectra of the samples recovered from the CO_2 heating experiments (dots) with spectral fitting results (black curves). We also present the IR spectra of the starting material (hydrous Rw) and hydrous Stv (Spektor *et al.*, 2011). The gap at 2800–3000 cm^{-1} is a region for C-H modes from CH contaminants on diamond anvils. After opening the diamond-anvil cell, we measured IR through one diamond anvil to prevent accidental loss of the sample. c, The MgO–SiO_2–H_2O ternary system and the formation of the lower-mantle minerals from anhydrous and hydrous Rw (left, Eq. 2.2, and right, Eq. 2.3). The H_2O contents in the top two ternary diagrams are exaggerated for the visibility of the expected phase assemblages. We present the properly scaled compositions of our starting material and recovered sample in the bottom diagram.

diagnostic features of the orthorhombic distortion. However, the severe peak overlaps of the Stv or mStv diffraction lines with Brd, MgO, and Ar at d-spacings smaller than 2.5 Å, made the unambiguous detection challenging. Therefore, we do not rule out the possibility of a $CaCl_2$-type distortion in the silica phase (therefore mStv) in our pressure range.

Previous studies have reported IR spectra of hydrous Stv (Spektor *et al.*, 2011, 2016a). However, these samples were synthesized at pressures lower than 10 GPa and therefore within the stability of Stv without a $CaCl_2$ type distortion. In contrast, our samples, all of which are synthesized above 35 GPa, may have experienced a transition from $CaCl_2$ type (mStv) to Stv during the decompression for the recovery. Therefore, comparison of our IR spectra to those of hydrous Stv from low-P experiments should be made with caution. Nevertheless, three modes at approximately 2550, 2870, and 3250 cm^{-1} from our samples show good agreement in frequency with those reported for a hydrous Stv sample (Spektor *et al.*, 2011), although the intensity distribution is different (Fig. 2.4b). Our IR spectra are measured on a much smaller area, and therefore significantly fewer grains in the samples, recovered from the LHDAC experiments, whereas the former study (Spektor *et al.*, 2011) was conducted for much larger sample synthesized in a multi-anvil press. In fact, as shown in Fig. 2.4b, the intensity distribution varies among different samples in our experiments, while mode frequencies are consistent with each other within $\pm 50\,cm^{-1}$, indicating the OH mode intensities of our samples are sensitive to crystallographic orientations and therefore preferred orientation. Different synthesis pressure and the sample history, discussed above, may explain the small but noticeable shift of the trend in the c/a and unit-cell volume relationship and the small but systematiicaly lower frequencies (by 30–100 cm^{-1}) of the major IR-active OH modes of our samples compared with hStv from low-P synthesis (Fig. 2.4a,b).

From the Gibbs phase rule, $F = C - \phi + 2$ (F is degrees of freedom, C is chemical components, and ϕ is number of phases in a system), for an MgO–SiO_2 system with two independent components (MgO and SiO_2; $C = 2$) at a range of P and T ($F = 2$), the maximum number of phases should be two ($\phi = 2$). This is the case for anhydrous Rw in MgO–SiO_2 and thus explains the following phase change in the lower mantle:

$$Mg_2SiO_4 \text{ (Rw)} \rightarrow MgSiO_3 \text{ (Brd)} + MgO \text{ (Pc)} \tag{2.2}$$

In our experiments, Rw contained H_2O and therefore we should consider a ternary system, MgO–SiO_2–H_2O ($C = 3$). In this case, the Gibbs rule predicts a ternary phase assemblage ($\phi = 3$) at a range of P and T. We indeed observed the stability of the Brd + Pc + Stv (or mStv) ternary phase assemblage at pressures between 35 and 59 GPa. Some phases in our final products should contain H_2O and as shown above Stv (or mStv) plays such a role. As shown in Fig. 2.4c, hydrous Stv (or mStv), together with Pc and Brd, can form a triangle in the ternary phase diagram for a stable phase assemblage. Because Brd is the phase with Si, in order to form hydrous Stv (or mStv), a partial breakdown is needed:

$$Mg_2SiO_4{\cdot}xH_2O \text{ (hRw)} \rightarrow (1-y)MgSiO_3 \text{ (Brd)} + (1+y)MgO \text{ (Pc)} + ySiO_2{\cdot}xH_2O \text{ (hStv)}, \tag{2.3}$$

where x is the amount of H_2O originally in Rw and y is the molar fraction of the Brd breakdown to Pc + Stv (or mStv).

In Fig. 2.4c, our starting composition is slightly above the triangle formed by the three lower-mantle phases after the transition. We note that the distance between the Rw composition and the phase assemblage triangle of Brd + Pc + Stv is within the estimated uncertainty of the H_2O content. The H_2O contents were estimated using different methods for Rw and Stv (IR and XRD, respectively) and therefore the systematic differences in these two methods may have contributed more than

the estimated error presented in Fig. 2.4c. The ternary phase diagram we presented here assumes that the system was closed with no interaction between Rw and the surrounding medium, either Ar or Ne. However, some amounts of H_2O could have been released to the pressure medium during heating. The noble gas medium escaped from the sample chamber during recovery, therefore we could not measure the amount of H_2O in the medium. If our hydrous Rw lost H_2O to the medium during the initial stage of laser heating, the composition point would shift toward the MgO–SiO_2 line, and possibly lied within the Brd–Pc–Stv triangle.

A recent high-pressure experiment (Walter *et al.*, 2015) observed Stv at lower-mantle related pressures in MgO–Al_2O_3–SiO_2–H_2O even when Mg/Si > 1, which is similar to our study. The study (Walter *et al.*, 2015) documented that Stv appeared at temperature above 1300 K and remained stable to at least 1900 K at 30 to 50 GPa together with Brd and MgO. Although the H_2O content in Stv was not reported, the observation of Stv in the Mg-rich system is consistent with our study and supports the important role of H_2O for the lower-mantle mineralogy. At lower temperatures, phase D and phase H were observed in the former study (Walter *et al.*, 2015), which was not the case in our experiments. However, their samples contained a factor of 3–5 greater amounts of H_2O than our samples, which could change the phase behavior. The amount of H_2O in our experiments is more consistent with recent estimations for H_2O content in the mantle transition zone (Pearson *et al.*, 2014; Fei *et al.*, 2017).

An experimental study (Schmandt *et al.*, 2014) of a $(Mg_{0.9}Fe_{0.1})_2SiO_4$ Rw sample with 1.1(1) wt% H_2O reported the observation of Brd, (Mg,Fe)O, and brucite after laser heating to 1873±100 K at 30 GPa. That study (Schmandt *et al.*, 2014) identified small amorphous regions in the TEM analysis of the quenched samples and attributed them to hydrous melting. Their XRD pattern does not show any silica peaks and their reported IR spectra for OH are different from Stv. The melting temperature

of silicates generally increases with pressure. Their pressure was lower than our experiments (Fig. 2.5). In addition, Fe in their Rw sample could reduce the melting temperature.

For a pyrolitic CaO–MgO–Al_2O_3–SiO_2, a multi-anvil press study showed that 2 wt% of H_2O, which is twice more than we have, reduces the melting temperature to ∼2400 K at 25 GPa (Litasov and Ohtani, 2002). Because it increases with pressure (Litasov and Ohtani, 2002), the melting temperature should be higher than 2400 K at the pressure range of our experiments. All of our experiments were conducted at temperatures below 2400 K, and we observed the formation of dense silica polymorph at temperatures as low as 1200–1630 K (Fig. 2.5). We also did not find any IR modes of brucite which has been often related to melting in high-pressure samples (Schmandt *et al.*, 2014). Therefore, I conclude that the silica observed in our study was a product of a solid-state reaction.

Our result indicates a stability of dense crystalline hydrous silica (Stv or mStv) even in a system with Mg/Si = 2.0 at the P–T conditions expected for the mid-mantle (top 800 to 1000 km depths of the lower mantle; Fig. 2.5). The pyrolitic composition model, believed to be representative of the mantle, has a lower (Mg+Fe)/Si ratio (1.5) but still more Mg than Si. Therefore, our observation of dense crystalline hydrous silica is still applicable for the pyrolite composition. Studies have shown that Fe does not significantly increase the solubility of H_2O in Brd and Fp (Panero *et al.*, 2015; Bolfan-Casanova *et al.*, 2002). Aluminum can dissolve in Stv as an AlOOH component and increase the solubility of H_2O in Stv even further (Pawley *et al.*, 1993). If Al partitions to Stv over Brd, Al could further stabilize silica in the Mg-rich mantle compositions. We note that that Stv or mStv formed even at the mantle geotherm temperatures, and contained percent levels of H_2O in our experiments (Fig. 2.5). This high temperature stability makes silica a favorable H_2O storage phase even in

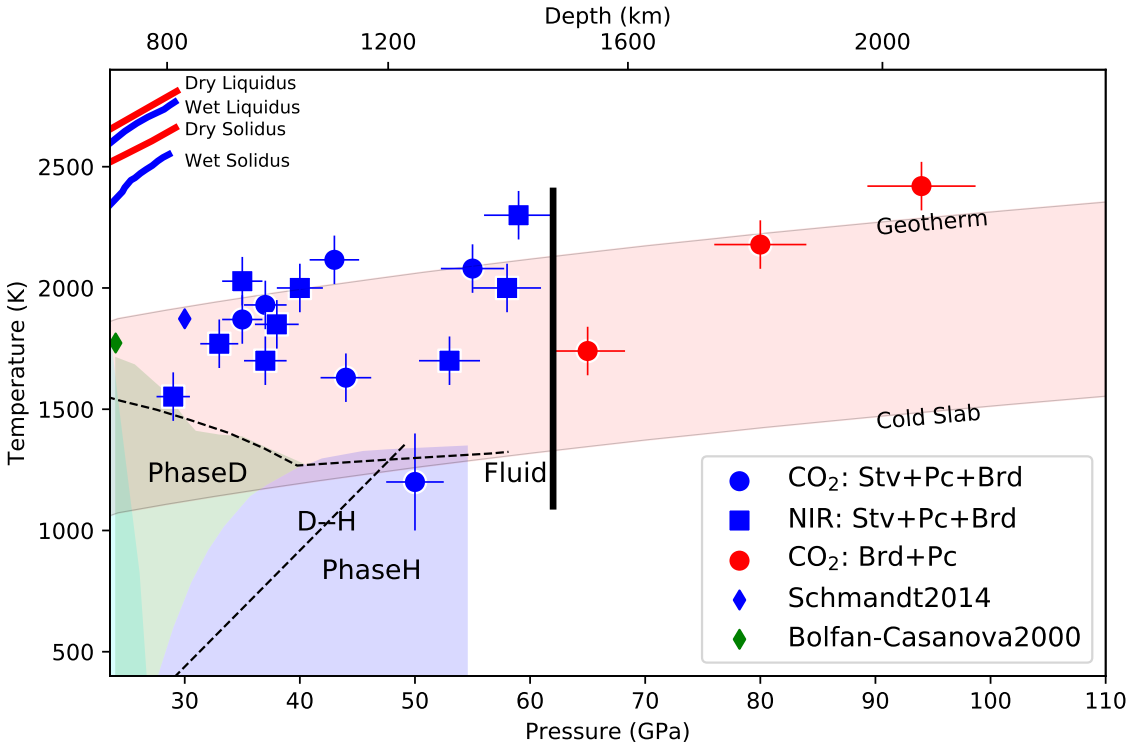

Figure 2.5: Pressure and Temperature Conditions for the Experimental Runs with the Observed Phase Assemblages.

We plot the expected temperature ranges at different depths between the cold subducting slabs and the mantle geotherm (Brown and Shankland, 1981a; Syracuse *et al.*, 2010). Melting temperatures for wet and dry mantle composition were taken from (Litasov and Ohtani, 2002; Boehler, 1996). We also plotted data points from former studies (Schmandt *et al.*, 2014; Bolfan-Casanova *et al.*, 2000). The black vertical line indicates the changes in the observed phases from dense silica phase (Stv or mStv) + bridgmanite (Brd) + periclase (Pc) to Brd + Pc (CO_2: CO_2 laser-heating experiments, and NIR: NIR laser-heating experiments).

the normal regions of the mid-mantle.

We conducted additional experiments at higher pressures (65 to 94 GPa) to further explore H_2O storage in the deeper mantle. Unlike our results below 59 GPa, there were no diffraction peaks of dense crystalline hydrous silica observed in these experiments (Fig. 2.5). Instead, the diffraction patterns were indexed completely with the peaks from Brd and MgO (Fig. 2.1c). These results suggest that H_2O storage mechanism undergoes changes at a depth of approximately 1500 to 1600 km (Fig. 2.5). Although hypothetical, some explanations are possible for the absence of a silica phase. First, this may indicate that the H_2O storage capacities of Brd and MgO can undergo a significant increase at higher pressures. However, a study (Panero *et al.*, 2015) has explored the H_2O solubility in Brd up to 65 GPa but did not find any H_2O solubility increase. Second, it is possible that an extremely H_2O rich phase (much higher than that of Stv or mStv) may become more stable at pressures above 65 GPa. In this instance, the required phase fraction of the H_2O-rich phase would be accordingly low, because the total amount of H_2O in our investigated system is fixed to 1 wt%. Therefore, it is possible that this phase may exist in our sample but with a volume fraction below the detection limit of the XRD, perhaps less than 1%. The detection of that type of H_2O-rich phase would require high-pressure experiments with much higher H_2O contents in the system to overcome the detection limit issue. However, the amount of H_2O in our starting material (Rw) is similar to that of the Rw inclusions in the diamonds from the mantle transition zone (Pearson *et al.*, 2014). Furthermore, the possibility of a small fraction in a H_2O-rich phase at this pressure range would not be sufficient to affect the physical properties of the mantle and slab, which we discuss below. Lastly, the limited amount of H_2O stored in Stv (or mStv) would require a relatively large amount of Stv (or mStv) to form in a Mg-rich system.

Numerous studies have documented Stv coexisting with (Mg,Fe)O and Brd (py-

roxene with Brd-like composition) as inclusions in diamonds from the lower mantle (Kaminsky, 2012; Stachel *et al.*, 2005; Litvin *et al.*, 2014). As shown in Eq. 2.2, the coexistence of Stv is very difficult to explain in the anhydrous pyrolitic lower mantle. Diamond inclusions have been often related to fluids or H_2O (Kaminsky, 2012; Kohn *et al.*, 2016; Tschauner *et al.*, 2018). Here we showed that Stv (or mStv) can form an equilibrium phase assemblage with Fp and Brd in an Mg-rich system if H_2O is present. Our observation, therefore, provides a new explanation for the coexistence of Stv with Fp and Brd in the lower-mantle diamonds. If so, those diamonds should originate from hydrous regions in the mid-mantle. We proposed that future studies measure the H_2O content of the Stv inclusions in lower-mantle diamonds.

To understand the effects of the partial breakdown of Brd and the formation of Stv (or mStv) induced by the presence of H_2O, we calculated density and velocity profiles for the mid-mantle regions with different hydration levels. Because we are primarily interested in properties changes, we used "simplified" pyrolite models with Brd and (Mg,Fe)O (Fp) with a pyrolitic ratio in the MgO–FeO–SiO_2–H_2O system. We conducted calculations for a range of simplified pyrolitic models where Brd and Fp (also stishovite, Stv, or its orhothormic modification, mStv, for hydrous systems) formed in a MgO–FeO–SiO_2 (+ H_2O) system with pyrolitic ratios for the considered chemical components:

$$\begin{aligned} & z[(1-x)(\mathrm{Mg}_{1-r}\mathrm{Fe}_r)_2\mathrm{SiO}_4 \cdot x\mathrm{H}_2\mathrm{O}]\ (\mathrm{Rw}) + (1-z)(\mathrm{Mg}_{1-m}\mathrm{Fe}_m)\mathrm{SiO}_3\ (\mathrm{Mj}) \\ & = (1-zx)(1-y)(\mathrm{Mg}_{1-b}\mathrm{Fe}_b)\mathrm{SiO}_3\ (\mathrm{Brd}) + [(1-zx)y + z(1-x)](\mathrm{Mg}_{1-f}\mathrm{Fe}_f)\mathrm{O}\ (\mathrm{Fp}) \\ & + [(1-zx)y\mathrm{SiO}_2 \cdot zx(1-k)\mathrm{H}_2\mathrm{O}]\ (\mathrm{Silica}) + zxk\mathrm{H}_2\mathrm{O}\ (\mathrm{Fluid}) \end{aligned} \tag{2.4}$$

where z is the molar fraction of Rw in the mantle transition zone ($z \simeq 0.5$ for pyrolite), x is the molar fraction of H_2O in Rw, and y is the molar fraction of Brd broken into silica and Fp by the H_2O effect. The atomic molar fractions of Fe in Rw, Mj, Brd, and

Fp are r, m, b, and f, respectively. $CaSiO_3$ perovskite was not included because it has only a minor impact for the properties (Shim *et al.*, 2000a) and did not participate in the reaction we considered here. Because Fe will not partition into silica, the formation of Stv by the partial breakdown of Brd will result in different amounts of Fe in Brd and Fp in a pyrolitic composition. We considered the Fe partitioning between Brd and Fp using the partitioning coefficient reported in ref.
citepirifune2010iron. The partitioning of Al is unknown at the moment between Brd and Stv (or mStv) and therefore we did not consider Al. If Al partitions into Stv (or mStv), it is known to increase the H_2O solubility and therefore will promote the partial breakdown of Brd and stabilization of a free silica phase even further (Pawley *et al.*, 1993). We assumed that H_2O exists only in Rw at the base of the mantle transition zone. Although other main minerals in the region, such as majorite and akimotoite, are known to contain some amounts of H_2O, the reported amounts are much lower than Rw (Bolfan-Casanova *et al.*, 2000). This assumption decreases the amount of H_2O in the mantle transition zone in our calculation and therefore underestimated the H_2O possibly stored in the lower mantle and the amount of free silica phase formed through the partial breakdown of Brd. Thus, our calculation provided conservative estimates for the changes in the physical properties. We calculated the density and seismic profiles along the mantle geotherm (Brown and Shankland, 1981a) using the Burnman package (Cottaar *et al.*, 2014a) and the SLB2011 physical parameter set for the minerals (Stixrude and Lithgow-Bertelloni, 2005). Although the dense silica polymorphs (Stv and mStv) had higher bulk modulus than Brd, the formation of Fp with very low bulk modulus by the partial breakdown of Brd was responsible for the decrease in bulk sound speed. Furthermore, H_2O reduced the bulk modulus of Stv and mStv (Nisr *et al.*, 2017a), which we take into account in our calculations. Dense silica polymorphs (Stv and mStv, or $CaCl_2$ type phase) have much high shear

modulus than Brd and Fp (Weidner *et al.*, 1982; Kurnosov *et al.*, 2017). Therefore, even a small amount of free silica phase formed through the partial breakdown of Brd would increase the shear velocity. H_2O tends to decrease the shear modulus, but the effects are not well known and therefore the effects on shear velocity remain uncertain. The combined effects of Al_2O_3 ($\sim$5 wt%) and H_2O ($\sim$0.25 wt%) reduced the shear modulus by $\sim$7% (Lakshtanov *et al.*, 2007a). Al_2O_3 itself decreased the shear modulus of dense silica polymorphs much more severely ($\sim$15% for $\sim$5 wt% of Al_2O_3) than the combined case (Gréaux *et al.*, 2016), suggesting that the reduction found in the combined case was mostly from Al and H_2O effect was much smaller. The solid lines shown in Fig. 2.6 are for the reduction estimated from the combined case. In Fig. 2.7, we present calculations with and without the H_2O effects on the physical properties of free silica phase.

We assumed that H_2O is stored only in dense silica, while Brd and Fp do not store any H_2O. We took into account a possible loss of H_2O from the mantle transition zone to the lower mantle, as either a fluid or a melt phase (Schmandt *et al.*, 2014; Tschauner *et al.*, 2018). In our "dry" lower-mantle model, no H_2O is stored in the lower mantle, which forms the Brd + Fp mineralogy. This model provides reference values to calculate possible changes in the physical properties by hydration (Fig. 2.6a). For the hydrated mantle models, we fixed the contents of H_2O in Rw and silica phase to 1.0 and 1.1 wt% based on our results combined with the diamond inclusion observation (Pearson *et al.*, 2014). In Fig. 2.6a, we present the two different hydration cases where 50% and 90% of H_2O is lost across the 660-km discontinuity. These two cases result in the formation of 25 and 6 mol% of silica as a free phase, and thus total H_2O amounts in the mid-mantle of 0.27 and 0.05 wt%, respectively (Tab. 2.3).

The formation of free silica phase by a the partial breakdown of dense Brd results in the reduction of density. In addition, H_2O also decreases the density of the silica phase

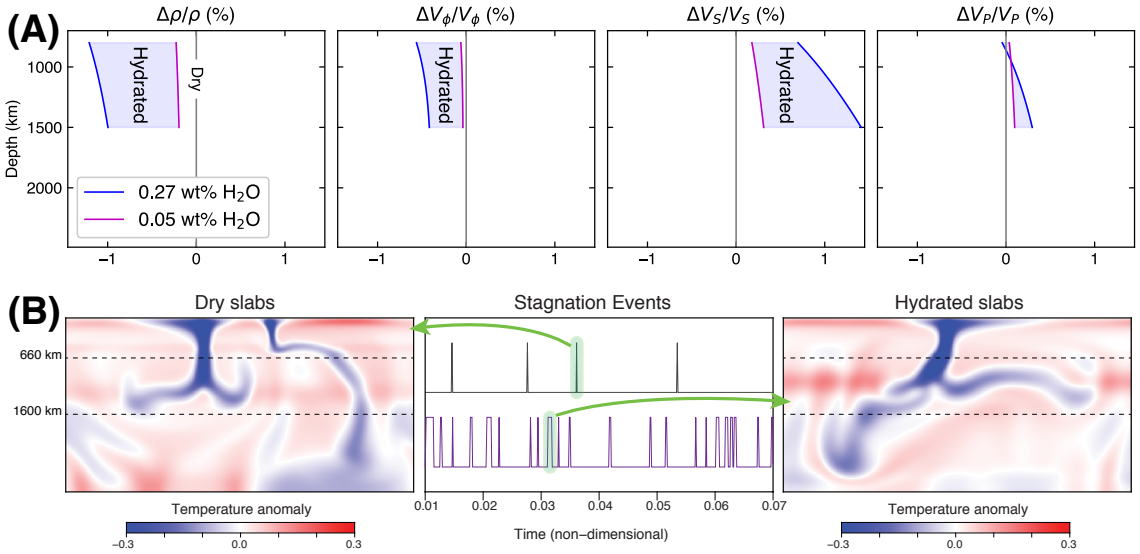

Figure 2.6: Geophysical Implications of the Mineralogical Changes Induced by Hydration in the mid Mantle.

a, Effects of hydration on the density (ρ) and seismic velocities (V_ϕ: bulk sound speed, V_S: S-wave velocity, and V_P: P-wave velocity). The magenta and blue curves represent percent changes in the properties for 0.05 and 0.27 wt% H_2O, respectively, at mantle-geotherm temperatures (Brown and Shankland, 1981a). b, Snapshots of slab thickening events found for dry (left) and hydrated (right) slabs in our geodynamic simulations. We present the temperature field for Rayleigh number (Ra) of 1×10^7. The center panel shows the timing of the slab stagnation events for the dry (gray) and hydrated (purple) slabs. The green areas indicate the stagnation events shown in the left and right panels. The slab stagnation (blue regions) occurs much more frequently with longer durations for the hydrated slabs.

itself (Nisr *et al.*, 2017a) (Fig. 2.6a). Combined, these effects results in a decrease in the density by 0.2–1% of hydrated regions in the mid-mantle compared with the "dry" regions. The most likely hydrated regions in the mantle are the subducting lithosphere (Ranero *et al.*, 2003). Because of its low temperature, the subducting lithosphere is denser, and thus negatively buoyant. For example, for a 500-K lower temperature, the subducting lithosphere is denser by approximately 0.75–1%, considering a thermal expansion parameter of $1.5{-}2{\times}10^{-5}\,\mathrm{K}^{-1}$ for mantle silicates. Our calculation shows that the hydrated subducting lithosphere (0.05–0.27 wt% H_2O) would have a lower density than dry surroundings by 0.2–1% in the mid-mantle if the temperature is the same. Combining the competing effects from low temperature and hydration, this means that the subducting slabs would be less negatively buoyant or even neutrally buoyant in the mid-mantle, depending on the level of hydration. In the deep mantle (depths greater than 1500 to 1600 km), because of the disappearance of the dense silica phase as observed in this study, the hydrated subducting slabs would regain negative buoyancy.

We conducted geodynamic simulations to explore the effects of H_2O on subducting slabs (Methods). Compared to the regular models, in which the slabs are negatively buoyant throughout the mantle because of lower temperatures (dry slabs), the models in which the slabs were made neutrally buoyant at 660 to 1600 km depths (hydrated slabs) exhibited a 10–15% reduction of the average mantle flow velocity. Both hydrous and dry slabs generally have an increased thickness in the lower mantle compared to the upper mantle in all of our models because of the increased viscosity in the lower mantle (Gurnis and Hager, 1988). However, we found that the hydrated and thus neutrally buoyant slabs are on average ∼30 to 40% thicker than the dry slabs at depths of 660 to 1600 km. This may be due to the longer residence of the hydrous and less dense slabs, which therefore results in more heat diffusion than the dry slabs

at this depth range. The thickness of slabs in the upper mantle was not affected. The convection pattern changes with time in our models, which is accompanied by changes in the morphology of slabs. Temporary stagnation of slabs at variable depths in the mid-mantle were found in both hydrous and dry slabs, prompted by factors which includes the viscosity increase in the lower mantle and trench motion on the surface. However, the stagnation of slabs occurred much more frequently and generally lasted for longer time for hydrous slabs than dry slabs (Fig. 2.6b), which may be due to the hydrous slabs sinking more slower, allowing more time for them to be passively and horizontally extends in response to the changing of mantle convection pattern.

It is intriguing that the depth range expected for the H_2O-induced mineralogy change and the slab stagnation found in our study (Figs 2.5 and 2.6) coincides with the depths at which seismic studies found a thickening and horizontal extension of some subducting slabs (Fukao and Obayashi, 2013; Waszek *et al.*, 2018). At the depth range of 660 to 1600 km, a viscosity increase was inferred from the Fe content in Brd (Shim *et al.*, 2017) and the properties of Fp (Marquardt and Miyagi, 2015; Deng and Lee, 2017), which would further enhance such slab behaviors. However, seismic studies have also found diverse behaviors of the slabs at the depth, from stagnation to deeper penetration (Kárason and Van Der Hilst, 2000; Fukao and Obayashi, 2013). In reality, subducting slabs may have a range of different degrees of hydration, depending on factors including the age and velocity of subduction (van Keken *et al.*, 2011). Because the density decrease is proportional to the degree of hydration (Fig. 2.6a), the diverse behaviors and structures of the slabs at the mid-mantle found in seismic imaging studies can be explained by the effect of H_2O and different H_2O contents in the subducting slabs.

Our calculation also showed that the hydration decreases the bulk sound speed by 0.1–0.5% in the mid-mantle (Fig. 2.6a). Although less certain due to the paucity of

data (Methods), hydration may increase shear velocity, while compressional velocity may not be affected. Hydrated slabs will remain as high-velocity regions due to lower temperatures, but the bulk sound speed contrast will be smaller. The shear velocity contrast can be enhanced for hydrated slabs in the mid-mantle. For mid-mantle regions without temperature differences, the variation in hydration can result in a negative correlation between bulk sound speed and shear velocity. According to our experiments, such negative correlations should be limited to the mid-mantle.

2.4 Conclusion

Our experiments demonstrate that Stv or mStv becomes thermodynamically stable in the hydrated subducting lithospheric mantle. Furthermore, if the mantle transition zone is hydrated globally, the transport of such hydrated minerals across the 660-km discontinuity by convective mantle flow away from the subducting slabs can produce free silica in Stv or mStv as a thermodynamically stable phase in the mid-mantle. In those mid-mantle regions, free silica phase will contain H_2O and exist with a significant fraction, even if a few hundreds of ppm of H_2O (for example, 6 mol% free silica phase for 500 ppm of H_2O) is transported because of either a limited amount of H_2O in the mantle transition zone, or release of H_2O at the 660-km discontinuity. The hydrous (and therefore silica-containing) regions in the mid-mantle will have a higher shear velocity even if the temperature is similar to the surrounding mantle. Such structures can explain the high shear-velocity anomalies documented in the mid-mantle regions away from the slabs and plumes in a recent seismic study (Waszek *et al.*, 2018).

Table 2.3: The Parameters for the Calculation of the Density and Seismic Velocity Profiles.

k is the H_2O loss factor in molar fraction and y is the molar fraction of Brd that breaks down by H_2O. x(Fe) is the atomic molar fraction of Fe in a mineral. Our dry model produces a 8:2 ratio in volume between Brd and Fp, which is consistent with the pyrolitic model (Jackson, 1998).

	Inputs		Mineral fraction (mol)			x(Fe)		wt% H_2O
Model	k	y	Brd	Fp	Stv	Brd	Fp	
Large H_2O storage	0.5	0.5	0.25	0.50	0.25	0.06	0.14	0.27
Small H_2O storage	0.9	0.1	0.57	0.37	0.06	0.08	0.17	0.05
Dry	1.0	0.0	0.67	0.33	0.00	0.08	0.18	0.00

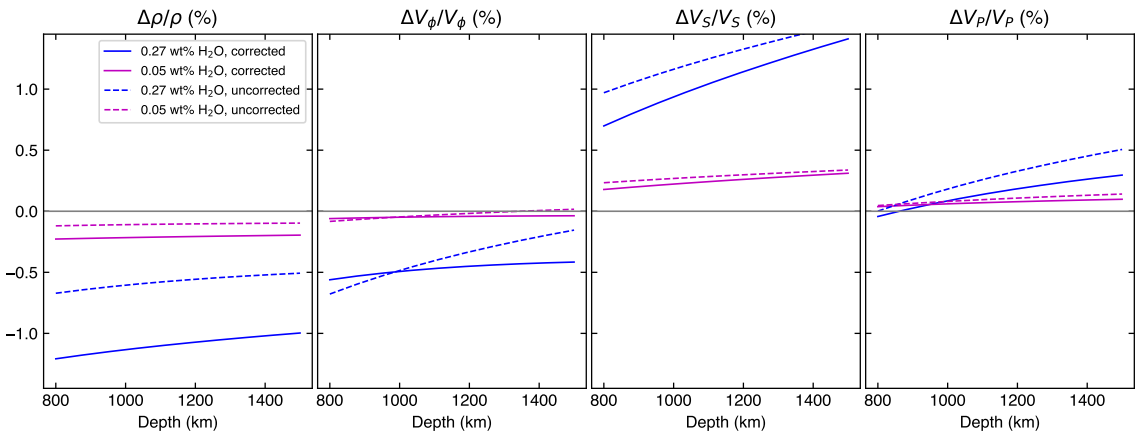

Figure 2.7: The Calculated Changes in the Density and Seismic Velocities by the Hydration of the mid Mantle Regions in the mid Mantle.

The magenta and blue curves show percent changes in the properties by 0.05 and 0.27 wt% of H_2O in the hydrous mantle regions, respectively, at mantle-geotherm temperatures (Brown and Shankland, 1981a) (Methods). The solid and dashed curves show property changes with and without considering the effects of H_2O on the physical properties of the dense high-pressure SiO_2 polymorphs.

Chapter 3

A NEW IRON HYDROXIDE PHASE STABLE IN HYDROUS LOWER-MANTLE SYSTEMS

3.1 Introduction

Hydrogen is the most abundant element in the solar system. However, the amount of hydrogen stored in the Earth's interior, which is volumetrically dominant, remains uncertain. The upper mantle to 410-km depth may contain a small amount of H, in the form of OH at 100–500 ppm H_2O (Michael, 1988). Laboratory experiments and diamond inclusion studies have shown that the mantle transition zone between 410 and 660 km depths may contain much more H as OH in the main mineral phases (wadsleyite and ringwoodite) and as a separate H_2O fluid phase (Pearson *et al.*, 2014; Kohlstedt *et al.*, 1996; Tschauner *et al.*, 2018) at least locally.

The lower mantle represents 55% of the Earth's volume and therefore possible storage of H in this region is important. However, the dominant minerals in the lower mantle, bridgmanite and ferropericlase, have extremely low H_2O storage capacities (Bolfan-Casanova *et al.*, 2002; Panero *et al.*, 2015). On the other hand, a series of hydrous phases have been recently found in studies at the high pressure–temperature (P–T) conditions of the lower mantle, most notably $CaCl_2$-type structured phases, such as δ-AlOOH, ϵ-FeOOH, and H-(Mg,Si)OOH (phase H), and pyrite-type structured phases, such as py-FeO_2H_x ($x < 1$) and py-FeOOH (Nishi *et al.*, 2014; Liu *et al.*, 2017; Nishi *et al.*, 2017; Sano *et al.*, 2004). These phases appear to form solid solutions in mantle-related chemical systems (Ohira *et al.*, 2014; Pamato *et al.*, 2015). Therefore, although not abundant, the high concentration of H in the phases provides

possible storage for a significant amount of H in the lower mantle.

Recent studies have shown that the py phase is stable above 80 GPa in Fe–O–H (Liu *et al.*, 2017; Nishi *et al.*, 2017). However, far fewer data points exist at the mid-mantle P–T conditions with large gaps between data points. It is unclear if ϵ-FeOOH (a low-pressure polymorph) transitions directly to py-FeOOH or an intermediate phase exists between the ϵ and py phases. This uncertainty raises an important question, whether Fe hydroxides can play a role in the H_2O cycle for a large depth range of the mantle. Recently a Fe-rich hexagonal phase was found in a Fe–Al–O–H system at the P–T conditions related to the mid to lowermost mantle, named as HH-phase (Zhang *et al.*, 2018). However, the crystal structure of HH-phase is unknown. Another mysterious Fe-rich hexagonal phase was documented in different system, Mg–Fe–Si–Al–O, also at the P–T conditions related to the mid to the lowermost mantle, named as H-phase (Zhang *et al.*, 2014) (Note that this H-phase is different from phase H. While H refers to its hexagonal structure for H-phase, H refers to an orthorhombic (Mg,Si)OOH in the $CaCl_2$ type structure (Nishi *et al.*, 2014). In order to avoid confusion, we will use H-(Mg,Si)OOH for phase H in this paper). The crystal structure of H-phase also remains unknown. Here, I report a series of experiments on Fe–O–H conducted at the P–T conditions of the mid-mantle in the laser-heated diamond-anvil cell (Table 3.1. We discovered a new hexagonal phase (hereafter η) in the system at 60–80 GPa and high temperatures. The amount of H stored in the new phase appears smaller than the ϵ and py phases. I also found that the new η phase can explain the enigmatic hexagonal phases found in mantle-related compositions (Zhang *et al.*, 2018, 2014).

3.2 Materials and Methods

We loaded pure hematite, goethite (Alfa-Aesar), or olivine $(Mg_{0.94}Fe_{0.06})_2SiO_4$ pre-pressed foil to a symmetric diamond anvil cell (DAC) chamber. Either H_2O or Ne was loaded as a pressure medium. Detailed information on experimental runs can be found in (Table 3.1). Diamond anvils with 200 μm culets and 150 μm beveled culets were used for experiments at pressures lower and higher than 65 GPa, respectively. An indented rhenium gasket was drilled for a sample chamber with a 90 or 120 μm in diameter, depending on the cullet size. We loaded a gold particle in the sample chamber for pressure calculation from the measured unit-cell volume (Ye *et al.*, 2017). In order to prevent potential alloying between Fe and Au at high pressures, the Au grain is separated from the sample foils. We placed a few spacer grains less than 10 μm below and above the sample foil to form layers of pressure medium between the sample and diamond anvils for thermal insulation. The spacer grains were chosen from the starting materials.

We measured X-ray diffraction (XRD) patterns of the sample in the laser-heated diamond-anvil cell at beamline 13ID-D and 13BMC at the GeoSoilEnviroCARS (GSE-CARS) sector (Prakapenka *et al.*, 2008b) of the Advanced Photon Source. Monochromatic X-ray beams with beam sizes of 3×4 μm^2 and 12×18 μm^2 at 13IDD and 13BMC, respectively, were focused on the sample. We have collected diffraction data for samples with an X-ray wavelength of 0.4133 or 0.434 Å with a Pilatus detector.

For heating, two near-infrared laser beams ($\sim$1 μm wavelength) were focused on the sample through both sides of DAC with a hot spot size of 20–25 μm^2 at beamline 13IDD. The laser beams were aligned co-axially with the X-ray beam so that we can measure diffraction patterns from the center of the heating spots. Temperatures of the sample were calculated by fitting the thermal radiation spectra to the Planck

equation from both sides of the sample. In each run, we heated the samples for at least 10 min. In run 612, in order to obtain a single phase, we heated the sample for two hours. We conducted diffraction pattern measurements both during laser heating and at 300 K before and after laser heating. At high temperatures, we calculated thermal pressures from the thermal expansion factor of ice VII (Fei *et al.*, 1993). Except for heating run 104 which was conducted at Arizona State University, all the heating was conducted at APS.

The measured diffraction images were integrated to diffraction patterns in the Dioptas package (Prescher and Prakapenka, 2015). We performed phase identification and peak fitting using a pseudo-Voigt profile shape function in the PeakPo package (Shim, 2017). The crystal structure was obtained from powder patterns in Endeavour, Fox, and Superflip (Putz *et al.*, 1999; Favre-Nicolin and Černỳ, 2002; Palatinus and Chapuis, 2007). Rietveld refinements were performed with the general structure analysis system (GSAS-II) (Toby and Von Dreele, 2013). We refined phase fractions first, then atomic positions, lattice parameters and spherical harmonic terms for preferred orientation. After reaching a good visual fit, we refined all the parameters together to further reduce residuals after background subtraction, $R_{wp-bknd}$. We achieved $R_{wp-bknd} < 1.8\%$ in all the refinements.

Table 3.1: Experimental Runs Conducted in This Study.

We include unit-cell parameters of the observed phases at high pressures and 300 K after laser heating. Temperature uncertainty is approximately 100 K. Other estimated 1σuncertainties are provided in parentheses. P: Pressure, T: temperature, S.M.: starting materials, Med.: pressure transmitting medium, Ol: olivine, Hem: hematite, Goe: goethite, η: $Fe_{12}O_{18}H_2$, py: pyrite-type FeOOH, and ϵ: $CaCl_2$-type FeOOH.

Runs	P (GPa)	T (K)	S.M.	Med.	η			py	ϵ
					V (Å^3)	a (Å)	c (Å)	V (Å^3)	V (Å^3)
103a	82(4)	1558	Hem	H_2O	221.24(4)	10.01(1)	2.549(1)	88.33(2)	47.7(2)
103b	83(4)	1720	Hem	H_2O	218.12(7)	9.93(3)	2.554(3)	87.79(7)	47.7(1)
204	51(3)	1420	Hem	H_2O					49.5(1)
204b	85(4)	1880	Hem	H_2O				88.09(6)	47.6(1)
204c	93(5)	2008	Hem	H_2O				87.08(4)	47.2(1)
204d	96(5)	1845	Hem	H_2O				86.94(7)	
301a	96(5)	1675	Hem	H_2O				86.89(7)	47.3(2)
301b	106(5)	2051	Hem	H_2O				86.12(5)	
417a	56(3)	1576	Hem	H_2O	233.51(10)	10.23(5)	2.576(1)		49.6(1)
417b	63(3)	1556	Hem	H_2O	230.82(10)	10.18(4)	2.572(2)		49.2(1)
504	74(4)	1631	Hem	H_2O	224.15(20)	10.07(5)	2.552(2)		47.9(1)
104	64(3)	1700	Goe	Ne	234.21(15)	10.16(5)	2.624(2)		48.9(1)
612	67(3)	1500	Goe	H_2O	233.29(15)	10.14(5)	2.620(2)		
ol18a	99(3)	2160	Ol	H_2O	230.8(15)			85.64(10)	
ol18b	106(3)	2176	Ol	H_2O				85.39(10)	

3.3 Result and Discussion

In our laser-heated diamond-anvil cell (LHDAC) experiments with a hematite starting material in an H_2O medium at 63 GPa and 1556 K, we observed at least nine new diffraction lines while the diffraction peaks from hematite disappeared (Fig. 3.3D). The new peaks appeared within 2 minutes of laser heating and grew steadily with heating. After temperature quench, we removed the laser mirrors from the X-ray beam path for better coverage toward the lower 2θ angles (i.e., higher d-spacings), enabling the detection of high d-spacing lines up to 9.6 Å. We found a diffraction line at $d-$spacing $\simeq$ 8.856 Å. This low angle line is key in constraining the shape of the unit cell. We found that the new lines are not associated with any known polymorphs of Fe_2O_3 (including post-perovskite, ppv, and Rh_2O_3-II type phases), FeH_x (dhcp and fcc), FeOOH (ϵ and py phases), and H_2O.

Weak ϵ-FeOOH peaks were observed at 56–83 GPa and 1400–1720 K in the beginning of laser heating. With further heating, the peaks of the ϵ phase become weaker while the intensity of the new phase increases at the pressures. We successfully synthesized a single phase of the η phase with laser heating for 2 hours, demonstrating the stability of the η phase over the ϵ and py phases at the pressure and temperature condition (Fig. 3.3D). For this sample, we obtained high precision X-ray diffraction patterns by oscillating the diamond-anvil cell around the incident X-ray beam by $\pm 23^\circ$. Such a measurement reduces the preferred orientation effect. From the high-quality powder diffraction patterns, we successfully assigned Miller indices for all the observed new lines with a hexagonal unit cell (Fig. 3.3).

Although first principles and experimental studies have discovered some new iron oxide phases at high pressures (Weerasinghe *et al.*, 2015; Bykova *et al.*, 2016), none of the structures can fit our diffraction patterns. Therefore, we conducted a separate

synthesis for thin starting hematite in an H_2O medium to obtain multi-grain type textured diffraction images at 82 GPa and 1558 K. In order to solve the crystal structure of the η phase, we conducted a series of analysis presented here using both powder diffraction patterns and textured diffraction images. Briefly, we first found candidate space groups from the systematic absence of some diffraction lines, resulting in $P6_3$ and $P6_3/m$. We then conducted simulated annealing and ab initio assisted Monte Carlo method to solve the crystal structure from powder diffraction patterns in the Endeavour and the Fox packages (Putz *et al.*, 1999; Favre-Nicolin and Černỳ, 2002). The crystal structure model we obtained in this way was then used for a starting structure model for Rietveld refinements in GSAS-II (Toby and Von Dreele, 2013). The new crystal structure model yields a 12:19 molar ratio between Fe and O. The crystal structure solution was confirmed through comparison with textured multi-grain type diffraction images (Fig. 3.1 and Table 3.2).

Given the fact that the η phase was synthesized in an H_2O medium, the phase may contain some amount of hydrogen. Because of the extremely weak scattering from H atoms, it is not possible to fit the observed diffraction patterns for H atoms in the η crystal structure. The observed unit-cell volume of the η phase is smaller than those of ϵ- and py-FeOOH when the unit-cell volume is normalized with respect to the number of Fe atoms in the unit cell, suggesting a lower amount of H_2O in the η phase (Fig. 3.2).

The larger volume of the η phase compared with the ppv phase suggests that the η phase contains some amount of H_2O. Although uncertain, we estimated a possible amount of H_2O in the η phase from the observed volume differences between the η phase and other phases (such as ϵ-FeOOH, py-FeOOH, and Fe_2O_3), similar to the method used for py-FeO_2H_x (Hu *et al.*, 2017). This calculation indicates a stoichiometry of $H_2Fe_{12}O_{19}$ for the η phase.

Table 3.2: Selected Diffraction Intensities and Angles (2θ) from the Textured Diffraction Patterns.

We observed weaker intensities for spots along the 010 direction due to the slightly misoriented crystal. They are noted with "w". ϕ is the azimuthal angle of the diffraction spot.

h	k	l	2θ (°)	ϕ (°)	Intensity	Note	I_{avg}	I_{calc}
1	0	0	2.739	155.00	787.4		0.05	0.03
0	1	0	2.739	95.00	205.3	w		
-1	1	0	2.745	35.00	749.6			
-1	0	0	2.739	-25.00	919.3			
0	-1	0	2.740	-85.00	400.0			
1	-1	0	2.745	-145.00	956.6			
1	1	0	4.772	127.00	101.6		0.01	0.02
-2	1	0	4.780	7.00	128.0			
2	-1	0	4.771	-173.00	91.0			
-2	0	0	5.487	-85.00	63.2		0.01	0.01
2	-2	0	5.489	-145.00	113.3			
2	1	0	7.253	138.00	216.9	w	0.04	0.11
3	-2	0	7.265	18.00	346.0			
-2	-1	0	7.267	-42.00	416.2			
1	-3	0	7.255	-102.00	330.5			
3	-2	0	7.259	-162.00	314.4			
1	2	0	7.255	108.00	106.1		0.01	0.01
3	0	0	8.231	155.00	245.16		0.03	0.02
0	3	0	8.233	95.00	100.5	w		
-3	3	0	8.247	35.00	310.4			
-3	0	0	8.231	-25.00	300.8			
0	-3	0	8.237	-85.00	180.2			

This estimation of low H_2O content in the η phase can be further supported by our experiments with a goethite (α-FeOOH) starting material in a Ne medium at 64 GPa and 1900 K. In that experiment, we observed the formation of H_2O ice by heating, suggesting that the η phase contains less H_2O than the starting material, α-FeOOH. We found that the η phase is not quenchable, which prevents us from conducting further analysis on the amount of H_2O in the η phase.

Our structural models for the η phase have two crystallographic sites for Fe. A half of Fe is 6-fold coordinated and the other half is 7-fold coordinated (Fig. 3.3C). The 7 coordinated Fe has a capped trigonal prism arrangement of six O atoms with one more O atom (i.e., 6+1 coordinated Fe). Similar coordination of Fe was also found in a Fe-oxide polymorph at 80 GPa (Bykova *et al.*, 2016). The crystal structure has the corner sharing FeO_6 octahedra and the six FeO_6 octahedra form a hexagonal channel at the [001] edges of the unit cell, which is similar to the structure documented in a high-pressure polymorph of $CaMg_2Al_6O_{12}$, so-called NAL phase (Miura *et al.*, 2000). The FeO_7 polyhedra are connected with the FeO_6 octahedra by edge-sharing. Two layers of FeO_7 have face sharing. This type of face sharing is also shown for the Mg sites with trigonal prism arrangement in the NAL phase (Miura *et al.*, 2000).

In order to further examine the stability of the η phase and its possible H_2O content, we have conducted first-principles calculations for $Fe_{12}O_{18}$, $HFe_{12}O_{18.5}$, and $H_2Fe_{12}O_{19}$ in the crystal structure we found in our experiments. In the H_2O-bearing crystal structure models, we located H and O atoms with a 2:1 ratio in the channels. Our experimentally observed unit-cell parameters are consistent with those calculated for $HFe_{12}O_{18.5}$ and $H_2Fe_{12}O_{19}$. We also found that $H_2Fe_{12}O_{19}$ is more stable than a ppv-Fe_2O_3 + Ice VII mixture at 40–85 GPa and 0 K (Fig. 3.7).

We also have measured a synchrotron Mössbaurer spectrum for the η phase at 62 GPa and 300 K (Fig. 3.6 and Table 3.6). The spectral fitting identified two domi-

nant sites for Fe with nearly equal fractions, which agrees with the crystal structure model of the η phase from our experiment. The Mössbauer parameters of both Fe sites are consistent with low-spin Fe^{3+} which was also found in our first-principles calculations.

We found that py-FeOOH appears together with the η phases at 83 GPa and 1720 K (also a small amount of ϵ). Above this pressure, the η phase disappeared and py-FeOOH became dominant with a small amount of the ϵ phase in diffraction patterns (Runs 103 and 301 in Table 3.1). Therefore, the stability field of the η phase is located at a lower pressure than that of the py phases, while likely at a higher pressure than the ϵ phase (Fig. 3.5).

The Fe–O–H system has been investigated at high P–T in recent years (Hu *et al.*, 2017, 2016; Liu *et al.*, 2017; Nishi *et al.*, 2014). These studies, however, explored mostly higher pressures than where the η phase is stable. A study reported py-FeO_2H_x at 72 GPa and 2300 K (Hu *et al.*, 2017), close to where we begin to observe a transition from the η phase to the py phase (Fig. 3.5). However, diffraction patterns were not reported for those P–T conditions. Another study examined FeOOH, reporting it to possible be the ϵ phase at 59 GPa and 2000 K and 79 GPa and 2100 K (Hu *et al.*, 2016), but the phase identification and X-ray pattern for the observation were not reported.

Recently a new hexagonal phase was documented in Al–Fe–O–H at 110–136 GPa and 2200–2400 K (named HH-phase) (Zhang *et al.*, 2018). However, no crystal structure was identified for HH-phase. The HH phase appeared for similar starting compositions and at similar $P-T$ conditions as the η phase, therefore we attempted to fit the reported diffraction peak positions of HH-phase to the η phase. We found that the η phase explains most of the reported diffraction lines very well, except for a few lines that may have resulted from peak overlaps with other phases (Table 3.4).

Table 3.3: Fitting H-phase Peak Positions with the η Phase Structure.

The diffraction peak positions are from (Zhang *et al.*, 2014), d_{obs}, for H-phase at 85 GPa and 300 K. The peak positions can be well explained by the η phase, d_{calc}, with $a = 10.26(4)$ Å and $c = 2.51(6)$ Å. Zhang *et al.* (Zhang *et al.*, 2014) assigned $a = 5.01(2)$ Å and $c = 2.86(3)$ Å for the same data. Δd is the fit residue ($= d_{\text{calc}} - d_{\text{obs}}$). The lines existing outside of the reported 2θ angle range are noted as "N.R.".

Zhang *et al.* (Zhang *et al.*, 2014)				Fit to the η phase					
d_{obs} (Å)	h	k	l	d_{calc} (Å)	h	k	l	Δd (Å)	Overlap
N.R.				8.8921	0	1	0		
N.R.				5.1339	1	1	0		
4.4495	1	0	0	4.4422	0	2	0	−0.0073	
2.5663	1	1	0	2.5647	2	2	0	−0.00159	py 111
2.4186	1	0	1	2.41536	0	1	1	−0.00324	
2.2266	2	0	0	2.2211	0	4	0	−0.0055	
1.9133	1	1	1	1.9147	0	3	1	0.00143	
1.7601	2	0	1	1.7583	1	3	1	−0.00176	
1.6791	2	1	0	1.6790	2	4	0	−0.00001	
1.4832	3	0	0	1.4807	0	6	0	−0.00247	
1.4511	2	1	1	1.4502	0	5	1	−0.00086	
1.3728	1	0	2	1.3549	1	6	0	0.02274	py113
1.3194	3	0	1	1.3466	1	5	1	0.02719	Brd
1.2850	2	2	0	1.2824	4	4	0	−0.00265	
1.1733	2	2	1	1.1768	1	7	0	0.00347	

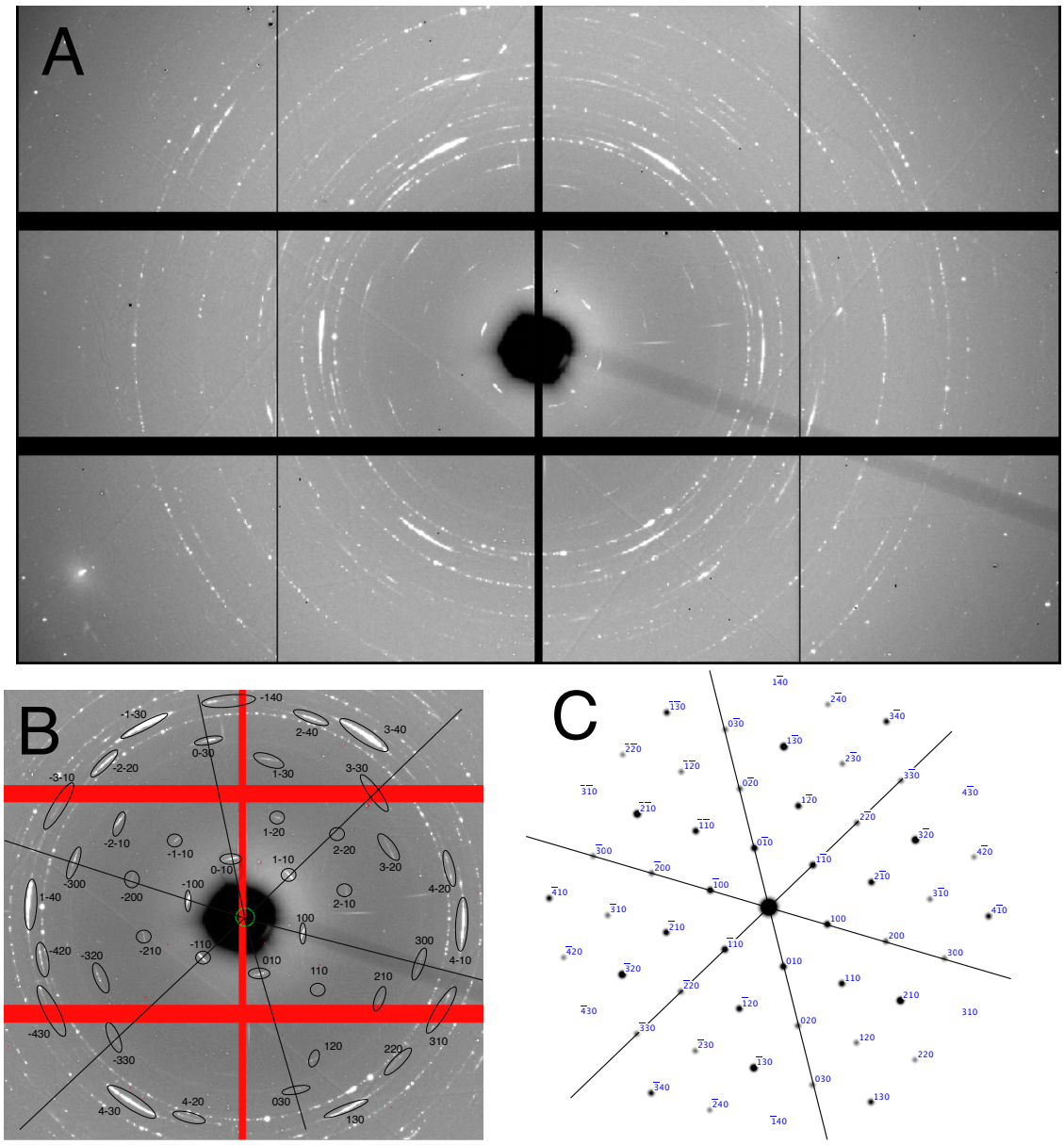

Figure 3.1: X-ray Diffraction Images of the Textured η Phase Sample at 80 GPa. (A) A diffraction image from run 103a. (B) A diffraction image from run 103a with the Miller indices assigned to thediffraction spots. (C) A calculated single crystal diffraction image for the η phase with the c axis parallel to the loading axis of the DAC and the incident X-ray beam direction.

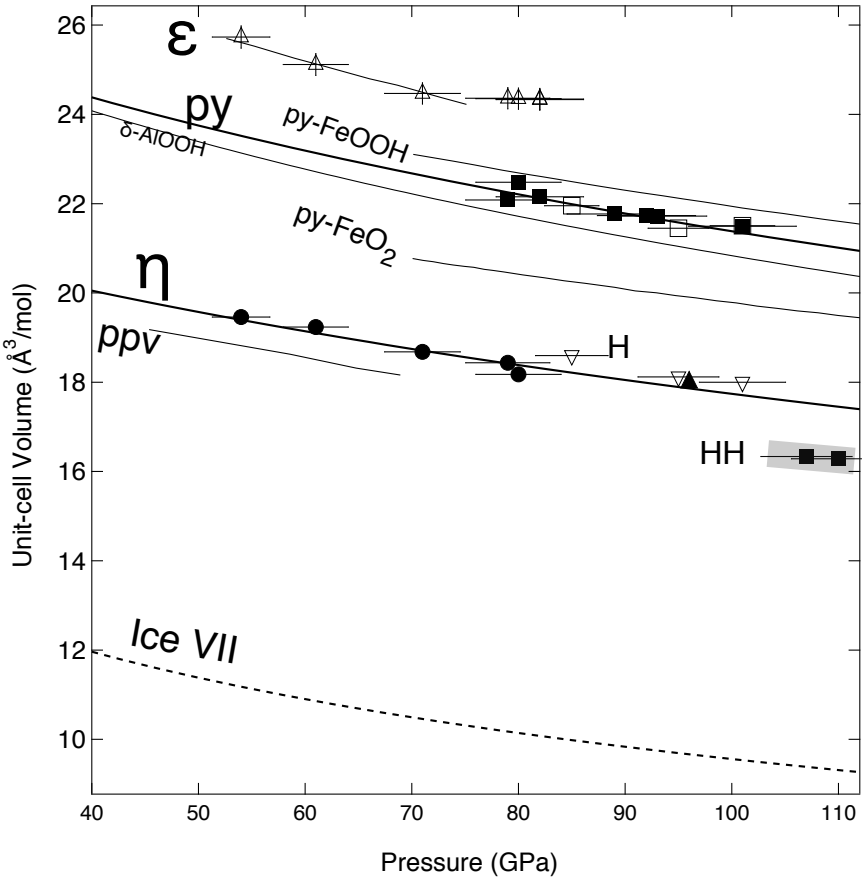

Figure 3.2: The Unit-cell Volume of the η Phase at High Pressure and 300 K. The unit-cell volumes are normalized by the number of Fe atoms in the unit cells. We also show the unit-cell volumes of ϵ-FeOOH and py-FeOOH measured in this study, and the unit-cell volume of H- and HH-phases (Zhang *et al.*, 2014, 2018) refit to the η phase structure. We include the compressional curves of py-FeO_2 (Hu *et al.*, 2016), py-FeOOH (Hu *et al.*, 2016), ϵ-FeOOH(Gleason *et al.*, 2013), ppv-Fe_2O_3 (Bykova *et al.*, 2013), and ice VII (Wolanin *et al.*, 1997) for comparison.

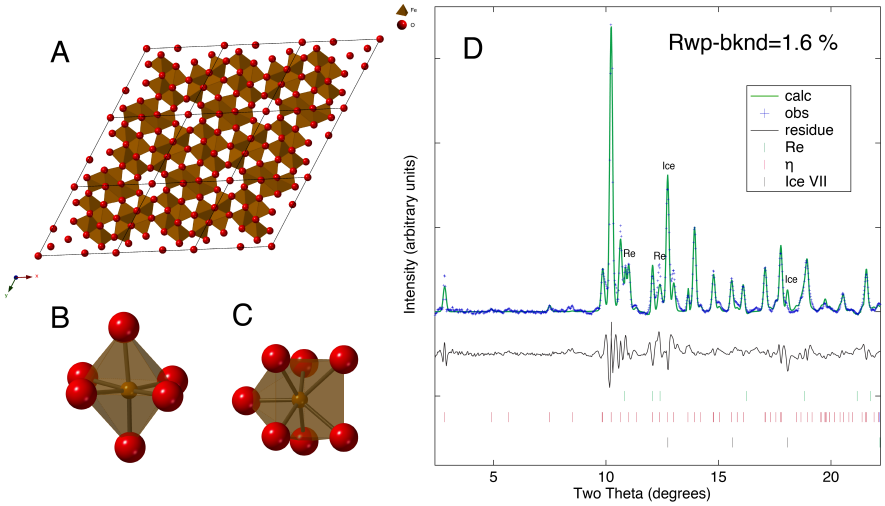

Figure 3.3: The Crystal Structure Model for the η Phase from Rietveld Refinements. (A) The crystal structure of the η phase along the c axis, (B) and (C) the Fe–O polyhedral with 6 and 7 coordination, respectively. (D) The Rietveld refinement for a diffraction pattern measured at 62 GPa and 300 K after laser heating: $a = 10.14(1)$ Å and $c = 2.62(1)$ Å for the η phase, $a = 2.70(1)$ Å for ice. The wavelength of the X-ray beam was 0.434 Å.

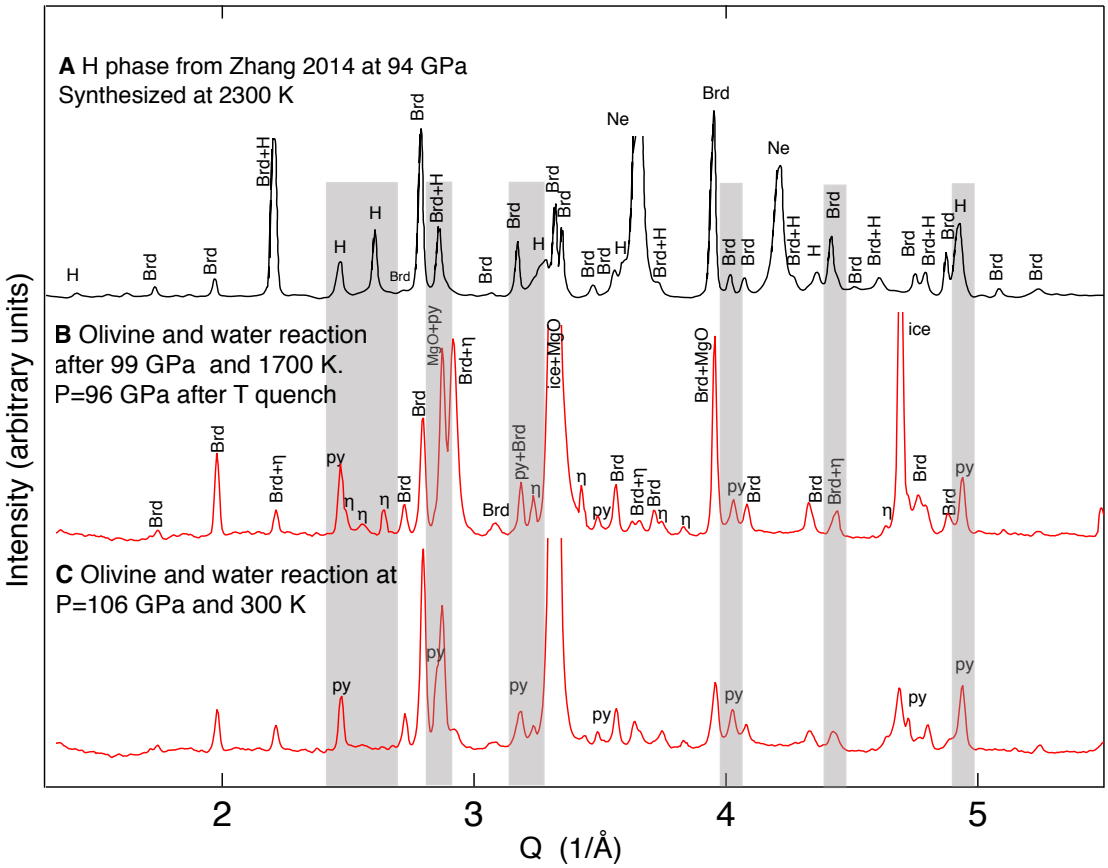

Figure 3.4: X-ray Diffraction Patterns from Olivine + H_2O Experiments Compared with a Pattern Reported for H-phase

(A) diffraction pattern of Brd and H-phase at 94 GPa reported in(Zhang *et al.*, 2014). The label for phase identification was taken from (Zhang *et al.*, 2014).(B) diffraction pattern of Brd, Fp, η and py phases at 96 GPa and (C) diffraction pattern of Brd, Fp, and pyrite phase at 106 GPa in our experiments. In the plot, Q(Q=2π/d) is used instead of two theta for the x-axis.

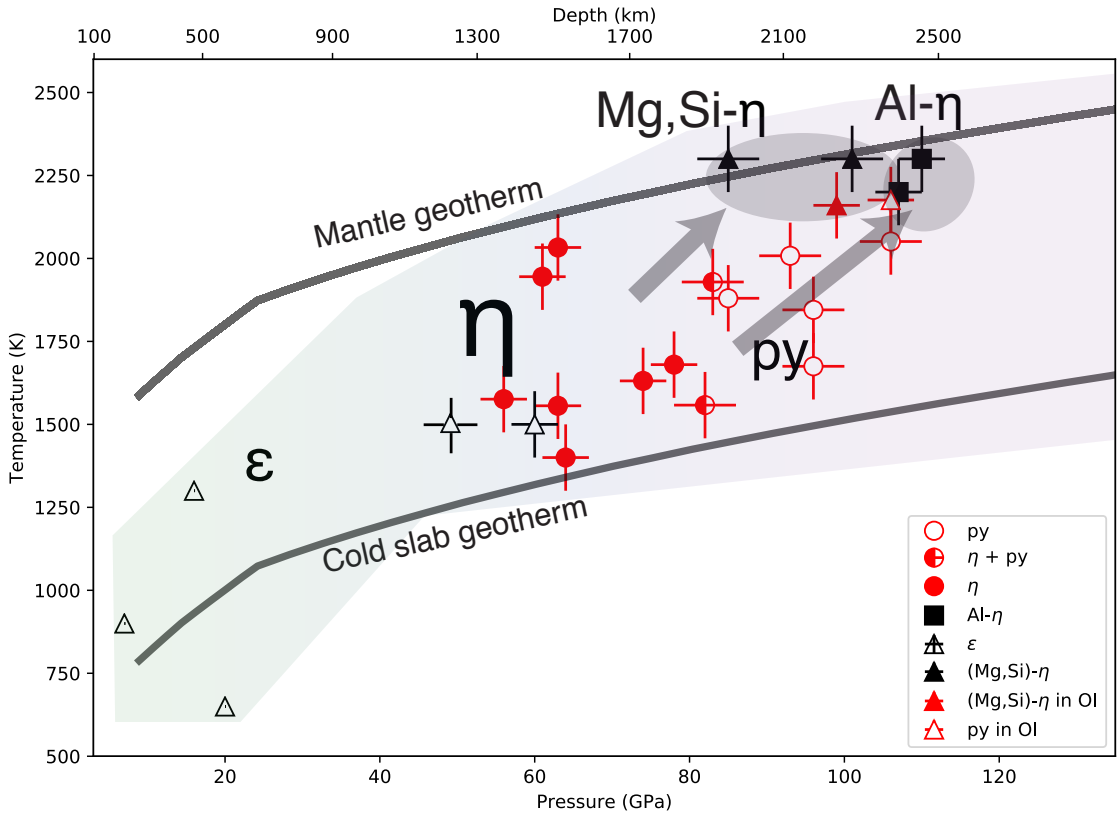

Figure 3.5: The Pressure-temperature Conditions for the Observation of Different Phases in Fe–O–H.

The closed and open circles indicate the observations of the η and py phases in our experiments. The half-filled circles are for observations of the η+ py + ϵ phases in our experiments. Some data points from former studies are shown for the ϵ and py phases (Gleason *et al.*, 2008; Dyuzheva *et al.*, 2006; Nishihara and Matsukage, 2016; Zhang *et al.*, 2014, 2018; Nishi *et al.*, 2017). We also included the data points for the Mg,Si-bearing η (former H-phase) and Al-bearing η (former HH-phases) phases (Zhang *et al.*, 2018, 2014). The mantle geotherm is from (Brown and Shankland, 1981a).

Table 3.4: Fitting HH-phase Peak Positions with the η Phase Structure.

The diffraction peak positions are from (Zhang *et al.*, 2018), $d_{\rm obs}$, for HH-phase at 107 GPa and 300 K. The peak positions can be well explained by the η phase, $d_{\rm calc}$, with $a = 9.52(4)$ Å and $c = 2.27(1)$ Å. Zhang *et al.* (Zhang *et al.*, 2018) assigned $a = 10.588(4)$ Å and $c = 2.596(1)$ Å for the same data. Δd is the fit residue $(= d_{\rm calc} - d_{\rm obs})$.

Zhang *et al.* (Zhang *et al.*, 2018)				Fit to the η phase				
$d_{\rm obs}$ (Å)	h	k	l	$d_{\rm calc}$ (Å)	h	k	l	Δd (Å)
2.2899	4	0	0	2.2867	0	2	1	−0.0032
2.0745	2	1	1	2.0612	1	2	1	−0.0133
1.8504	2	2	1	1.8352	1	3	0	−0.0152
1.8138	3	1	1	1.7992	0	3	1	−0.0146
1.6317	3	2	1	1.6430	0	4	0	0.0113
1.4415	4	2	1	1.4533	2	3	0	0.0118
1.1265	4	0	2	1.1248	1	4	0	−0.0018

We emphasize that the unit-cell shape of the η phase is different from the hexagonal unit cell proposed for HH-phase in Zhang *et al.* (Zhang *et al.*, 2018). They assigned the unit cell based on a multi-grain method for diffraction patterns measured at different tilting angles of a diamond-anvil cell. However, the reported diffraction patterns in (Zhang *et al.*, 2018) do not include sufficiently low 2θ angles for the detection of a few high d-spacing lines of the η phase. We found that it is extremely difficult to find the unit-cell shape without these high d-spacing peaks (in particular the 010 line). The unit-cell volume of HH-phase fitted to the η structure is 4.8–4.9% smaller than that expected for the Fe-endmember η phase at the same pressures (Table 3.4). The smaller unit-cell volume can be easily explained by Al existing in their

samples (20–40%), because of the smaller ionic size of Al^{3+} compared with Fe^{3+}.

Another enigmatic hexagonal Fe-rich phase was documented in different compositions, Mg–Si–Fe–Al–O, at 85–110 GPa and 2200-2400 K, named H-phase. Zhang *et al.* (Zhang *et al.*, 2014) proposed that H-phase forms from the disproportionation of Fe-bearing bridgmanite to Fe-poor bridgmanite + Fe-rich H-phase. According to the report, Fe-rich H-phase contains some amounts of Mg and Si. Similar to the case for HH-phase, the study did not find any plausible crystal structure for H-phase. However, in more recent studies using Fe-rich bridgmanite stoichiometry starting materials, such disproportionation and therefore H-phase have not been observed and Fe-rich bridgmanite remained stable at similar P–T conditions (Dorfman *et al.*, 2013; Wolf *et al.*, 2015; Ismailova *et al.*, 2016).

We also conducted an experiment on olivine in an H_2O medium at 96–106 GPa and 1950 K. The diffraction patterns from this experiment are surprisingly similar to the diffraction pattern from Zhang et al., 2014. As shown in Fig. 3.4, the H phase could be a mixture of the η and the py phases. At 106 GPa, we only observed pyrite-type FeOOH, consistent with our interpretation that py-FeOOH exists at higher pressures than the η phase.

The c/a ratio of 0.244 from refitting the diffraction peaks of H-phase to the η phase is slightly smaller than that of the Fe-endmember η phase (0.257), which is likely because of the different chemical composition (Mg, Si, and Fe^{2+} in H-phase, or now Mg,Si-bearing η phase). The unit-cell volume of the Mg,Si-bearing η phase is slightly larger than the Fe-endmember η phase (Fig. 3.2). Because the Mg,Si-bearing η phase was formed from Fe^{2+}-rich starting materials, the larger ionic size of Fe^{2+} could explain the observed unit-cell volume. If the spin state of Fe is different between the Fe-end member η phase and the Mg,Fe-bearing η phase, it can also change the unit-cell volume.

The formation of the η phase in (Zhang *et al.*, 2014) requires some amount of H_2O. However, it is unclear how much H_2O existed in the experiments and if the anhydrous form of the η phase could exist similar to the case of py-FeO_2(Hu *et al.*, 2016). Because the H_2O content in the η phase is about 2 wt%, thousands of ppm water could be enough to explain the result from (Zhang *et al.*, 2014).

While the stability of py-FeOOH is potentially significant for the storage of H in the lowermost mantle, it has been unclear how H can be delivered to the stability field of py-FeOOH. The new η phase is stable at the lower pressure side of the py-FeOOH stability field. According to our study, some substantial amount of H_2O will be lost during the transformation from the ϵ phase to the new η phase. If the η phase is stable at the P–T conditions of the subducted slabs in the mid mantle, as supported by our data (Fig. 3.5), the η phase will limit the transport of H_2O deeper into the lowermost mantle, where py-FeOOH would be stable. In addition, the possible explanation for the enigmatic observations of hexagonal phases found in other mantle related systems have important implications for the H_2O storage and mineralogy in the deep mantle: HH-phase in Al–Fe–O–H and H-phase in Mg–Si–Fe–Al–O. If the H- and HH-phases are the η phase (and therefore Mg,Si-bearing η and Al-bearing η phases, respectively), as supported by our results, these enigmatic observations now can support the stability of the η phase in a range of mantle-related compositions. In fact, similar solid-solution relationships have been found among similarly compositioned hydroxide phases at lower pressures, δ-AlOOH, H-(Mg,Si)OOH, and ϵ-FeOOH, all of which have essentially the same crystal structure, $CaCl_2$ type (Ohira *et al.*, 2014; Nishi *et al.*, 2015).

It is also notable that the Al-bearing η phase and the Mg,Si-bearing η phase have been found at higher pressures and higher temperatures than the Fe-endmember η phase (Fig. 3.5). The AlOOH component in H-(Mg,Si)OOH is known to stabilize the

phase to higher P–T (Ohira *et al.*, 2014) and such Al effect was also found for phase D (Pamato *et al.*, 2015). According to Zhang *et al.* (Zhang *et al.*, 2014), H-phase (Mg,Si-bearing η phase) contains Mg and Si. The effects of Mg and Si in Fe^{3+} dominant hydroxide are not well known. However, the trend we found in Fig. 3.5 indicates that the stability field of the η phase can be further expanded to the lowermost mantle with the incorporation of Mg, Si, and Al, which are major rock-forming elements in the mantle. Furthermore, both Al-bearing and Mg,Si-bearing η phases were observed at temperatures close to the mantle geotherm in the lowermost mantle.

We found that a primitive hexagonal unit cell matches all the new peaks well. For example, for the diffraction patterns measured after laser heating at 59 GPa, we observed a peak at 8.85 Å (the lowest angle diffraction line), which provides an important constraint on the a axis. We can index the a axis of the new structure to be 10.227 Å. All the diffraction lines observed at low 2θ angles of 2.5–7.1° can be well indexed with Miller indices of $hk0$ from the a parameter. This fitting result indicates that the c axis needs to be much smaller in length. We chose lines that cannot be indexed as $hk0$ in search for the c cell parameter. For example, a line with a d-spacing of 2.51 Å cannot be indexed with $hk0$. Among the many attempts we made, we found the most satisfactory results when we assign 011 to a line at 2.51 Å. From this unit cell assignment ($a = 10.227(5)$ Å and $c = 2.576(1)$ Å at 59 GPa and 300 K), we can index all the diffraction lines between 2.5°2θ and 25°2θ (or a d-spacing range between 9.4 and 0.95 Å). Our Miller index assignment was then tested with EXPO2004(Altomare *et al.*, 2004), which confirmed the a and c axis.

We found the systematic absence of lines with $00l$ for $l = 2n + 1$, indicating a 6_3 screw axis in the crystal structure of the new η phase. Thus, the space group of the new structure can be $P6_3$ (173), $P6_3/m$ (176), or $P6_3/22$(182). The three space groups can be distinguished from Laue symmetry $6/m$ or $6/mmm$, which we examine

below.

In order to obtain a pure sample for the η phase, we heat a sample in diamond-anvil cell for an extended period of time at a temperature between 1300–1500 K and 66 GPa. The attempt was successful after two hours of laser heating. In the diffraction patterns, only the η phase existed together with ice VII (medium) and weak Re peaks (gasket) as shown in (Fig. 2D). The diffraction peaks from Re and ice VII only contribute 3 peaks. We oscillated the diamond anvil cell around the X-ray beam by $\pm 23^\circ$ during diffraction measurements. We found such an operation can enhance random orientation for crystals during diffraction measurements.

For this diffraction pattern, we used simulated annealing and ab initio assisted Monte Carlo method to solve the crystal structure from powder diffraction in Endeavour and Fox (Putz *et al.*, 1999; Favre-Nicolin and Černỳ, 2002). Two separate methods yielded the same result with a crystal structure showed in (Fig. 3) with a composition of $Fe_{12}O_{18}$ in a space group of either $P6_3$ or $P6_3/m$. We could not achieve a reasonable crystal structure with $P6_3/22$, which we will discuss below using Laue symmetry. When the $P6_3$ space group was used as a starting point, the final structure solution would end up with the $P6_3/m$ space group. Thus the space group can be assigned as $P6_3/m$. A charge flipping method was also tested, which could not figure out the crystal structure but correctly resolved the 12 Fe atoms (Palatinus and Chapuis, 2007). The charge flipping method requires high-quality diffraction patterns without preferred orientation, which might be the reason for not resolving the structure. We believe some degree of preferred orientation may still exist despite the effort of oscillating the diamond-anvil cell. When we compared the obtained unit-cell volume of the η phase with py-FeOOH (or $Fe_{12}O_{24}H_{12}$), we found that the number of O atom should be smaller than 24 (Fig. 3.2). Otherwise, the density of the lower-pressure phase η becomes higher than that of py-FeOOH.

We conducted Rietveld refinements in order to obtain the atomic positions of Fe and O atoms (Table 3.5). A composition $Fe_{12}O_{19}$ was achieved from fitting the powdered pattern. Based on the electron density map in Rietveld refinement, we found another oxygen position in the tunnel in the crystal structure (Fig.2D) This oxygen is very likely to be hydrated since it is unlikely to have single oxygen in the tunnel. The stoichiometry ($Fe_{12}O_{19}$) of this phase also needs two more hydrogens to balance the extra negative charge. Thus, we indicate this oxygen as Ow in (Table 3.5). The justification of water content will be discussed below.

Table 3.5: The Crystal Structure of the η Phase from Rietveld Refinements of a Pattern Measured at 66 GPa and 300 K.

The unit cell parameters are: $a = 10.14(5)$ Å and $c = 2.62(2)$ Å. The space group is $P6_3/m$.

Atoms	x	y	z	Occupancy
Fe1	0.384(2)	0.552(4)	0.25	1
Fe2	0.942(1)	0.694(2)	0.25	1
O1	0.393(3)	0.407(3)	0.75	1
O2	0.883(5)	0.781(2)	0.75	1
O3	0.492(1)	0.720(4)	0.75	1
Ow	0.0	0.0	0.0	0.5(1)

Diamond-anvil cell is a uni-axial device and therefore often results in preferred orientation of a powdered sample. Such a preferred orientation can be particularly strong depending on the morphology of crystals and pressure transmitting medium (Chen *et al.*, 2018). We note that the unit-cell shape of the η phase has a flat shape with much larger a axes than the c axis. In order to obtain a multi-grain type sample, we prepared a separate sample with a very small thickness (1μm thick) (run 103).

The patterns obtained from this experiment suggest that the sample consists of a few single crystals of the η phase with their c axis aligned parallel to the loading axis of diamond-anvil cell and incident X-ray beam. In our 2D diffraction images, the well-crystallized η phase produces spotty Debye diffraction rings (Fig. 3.1). In particular, for the rings at lower angles, we found six main diffraction spots separated by 60° to each other, for example, the ring at 8.66 Å of d-spacing, forming a hexagonal shape. The intensities of the six diffraction spots are nearly the same, confirming the hexagonal crystal structure of the η phase. For the Laue symmetry, the difference between $6/m$ and $6/mmm$ lies in the intensity distribution that is overlapped and thus not possible to distinguish in powder diffraction. For example, the intensities of 210 or 120 spot should be different in $6/m$ but same in $6/mmm$. We can take advantage of the textured or multi-grain type diffraction patterns to confirm the space group and crystal structure solution. The diffraction spots and corresponding intensities from this textured sample were shown in (Table 3.2 and Fig. 3.1). The existence of two groups of intensity distributions of the 130 and 310 peaks confirm the $6/m$ Laue symmetry. Thus the space group can be assigned to $P6_3/m$.

The single crystal diffraction spot positions and intensities were calculated with $Fe_{12}O_{19}$ in (Table 3.2) with the c axis parallel to the X-ray beam. We then compared the calculation with our textured X-ray diffraction patterns. The intensity partition of overlapped diffraction peaks matched well with the calculation, supporting the crystal structure solution. The textured diffraction pattern showed 37 individual diffraction spots. The crystal structure solution or atomic position will affect every single diffraction spot and intensity. The averaged diffraction intensity for the equivalent diffraction spot in the $6/m$ Laue symmetry confirmed the crystal structure solution. The c axis of crystals is not exactly parallel to the beam, which can cause some directions to have lower intensities. For example, the 010 direction shows lower

intensity than other directions (Fig. 3.2). To be able to resolve a crystal structure, coverage of large d-spacing is needed in single crystal diffraction. However, the aperture of the used diamond anvil cell limits the angular coverage to a maximum $35°2\theta$. A multi-grain type diffraction can be affected by overlapping of diffraction spots from twined or polycrystals, making it difficult to extract intensity from diffraction spots. The powder diffraction method has successfully solved crystal structures up to 7562 $Å^3$ with 234 atoms (Corma *et al.*, 2010). It is often very difficult to obtain sufficient quality single crystal for crystal structure determination at high pressure. In addition, for the phases which are only stable at high pressure, such as the η phase in this study, the d-spacing information is limited because of the diamond-anvil cell geometry. In this study, we demonstrated that a combination of powder diffraction and multi-grain diffraction can be a powerful method to obtain the crystal structure of such high-pressure phases.

For experiments with starting materials of Fe_2O_3 and H_2O, products of the possible chemical reaction between them should exist on a tie line between these two compositions. The final product should be then: $Fe_2O_3 \cdot xH_2O$.

$$Fe_2O_3 + xH_2O \rightarrow Fe_2O_{3+x}H_{2x} \text{ (or } Fe_2O_3 \cdot xH_2O) \tag{3.1}$$

For example, when $x = 1$, the reaction will produce FeOOH.

In contrast, for the laser heating of a goethite starting material in a Ne medium, H_2O exists only in the starting α-FeOOH and therefore the amount of H_2O is limited. In this experiment, we observed the formation of ice VII as well as the η phase. Tiny anhydrous ppv-Fe_2O_3 peaks were also observed in some of the diffraction patterns. The reaction in this experiment can be written as:

$$12FeOOH(\alpha) \rightarrow 5H_2O(IceVII) + Fe_{12}O_{19}H_2(\eta) \tag{3.2}$$

We reported the unit cell volumes in (Fig. 3.2) from all the experiments we had performed. Our measured unit-cell volumes of the ϵ and pyrite-type phases are consistent with the reported values (Gleason *et al.*, 2013; Nishi *et al.*, 2017) at high pressure and 300 K (Fig. 3.2). For the pyrite-type phase, our unit-cell volume values are close to the fully hydrated version of the phase, py-FeOOH. The unit-cell volume of the η phase is smaller than both ϵ and pyrite-type FeOOH, meaning that less H_2O exists in the η phase.

Because of the difficulty in measuring the content of H in py-FeOOH, which is not quenchable at 1 bar(Hu *et al.*, 2016), Hu et al., 2016 used the unit-cell volume difference between the dry form of FeO_2 and hydrated form and attributed the difference to the effect of H. We conducted similar calculations here. For the ϵ and η phases, no dry form is known unlike the py phase. Because the ϵ and η phases can be written in a form of $Fe_2O_3 \cdot xH_2O$, we adapted ppv-Fe_2O_3, which is stable at the stable pressures for the η phase, as a dry form (Shim *et al.*, 2009). The approach has clear limitations in that the dry forms in Fe_2O_3 and hydrous forms have different crystal structures in this case. Nevertheless, the calculation presented below provides some qualitative insights into the content of H_2O in the η phase.

At 60 GPa, we found the unit-cell volume of ϵ-FeOOH is 25.12 Å^3 for V/x(Fe) (Fig. 3.2), which is a unit-cell volume divided by the number of Fe atoms in the unit cell. The value is consistent with (Gleason *et al.*, 2013). At the pressure, the post-perovskite type structure (ppv) became stable in Fe_2O_3, which we take as a dry form. The ppv-Fe_2O_3 has $V/x(\mathrm{Fe}) = 18.55$ Å^3 at 60 GPa. The volume difference between the ϵ-FeOOH and the ppv-Fe_2O_3 can be roughly attributed to the volume occupied by H_2O in the crystal structure of the ϵ phase. Therefore, we can obtain $\Delta V/x(\mathrm{Fe}) = 6.57$ Å^3 for $\frac{1}{2}H_2O$.

The η phase has a larger unit-cell volume than ppv by $\Delta V/x(\mathrm{Fe}) = 0.62$ Å^3 at

60 GPa. Then, we calculated the unit-cell volume for the η phase with one Fe atom to be 26.69 Å^3 at 60 GPa. If the rate of the unit-cell volume change we measured above between the ϵ phase and ppv-Fe_2O_3 was applicable between the η phase and ppv phase, we can estimate $0.06H_2O$ for 1 mol of $FeO_{1.5}$.

The estimation we made above ignored a few important possibilities. For example, the Fe-O framework of the η phase is different from the Fe-O framework of the ϵ phase and ppv, and therefore a certain amount of the difference we discussed above should be attributed to the difference in the volume of the Fe-O framework.

We estimated from the crystal structure of the η phase: $Fe_{12}O_{18.72}H_{1.44}$ ($0.06H_2O$ per $FeO_{1.5}$), or $Fe_{12}O_{19}H_2$ ($0.08H_2O$ per $FeO_{1.5}$) for an ideal composition. We note that the differences for water content lie in the crystal structure site "Ow" in (Table 3.5). The Rietveld refinement gave a water content that was in general agreement with the volume calculation. Although, the exact amount of H_2O remains uncertain due to the limitations in our data, the volume comparison we made here support the existence of H_2O in the η phase and the smaller amount of H_2O in the η phase than either ϵ-FeOOH or py-FeOOH.

The sample was synthesized from a Fe_2O_3 + H_2O mixture at 62 GPa and 1600 K in LHDAC. In order to enhance the Mössbauer signal, we used ^{57}Fe enriched (67%) Fe_2O_3. X-ray diffraction of the sample indicates that the majority of the sample is the η phase with a small amount of the ϵ phase. Nuclear forward scattering was conducted at sector 3 of APS. We focused a 14.4-keV X-ray beam on an area of $6\times6\,\mu m^2$ in the sample. The storage ring was operated in top-up mode with 24 bunches separated by 153 ns. We measured nuclear resonant scattering in a time window of 15–130 ns with a data collection time of 30 min. We measured SMS at high pressure after temperature quench.

The spectral fitting was performed for the measured spectrum using the CONUSS

package(Sturhahn, 2000). In order to avoid non-uniqueness of the fit results, we conducted Monte-Carlo search in CONUSS in the beginning of all the fittings we performed. Because we detected a small amount of the ϵ phase we included the Mössbauer parameters of the phase from a separate measurement for pure ϵ Mössbauer measurements. For the isomer shift, we measured a separate spectrum with the sample and $FeSO_4 \cdot 7H_2O$.

Our Mössbauer measurements for the η phase identified three different Fe sites shown in (Fig. 3.6 and Table 3.6). Two of the three sites have Mössbauer parameters consistent with low-spin Fe^{3+} with a 1:0.8 ratio between them in fraction. The third site appears to be a high-spin Fe^{3+} site, but its fraction is close to the estimated uncertainty while the other two η sites are more than 10 times greater in fractions and therefore more dominant. The fractions of these two dominant sites and their Mössbauer parameters are consistent with our crystal structure model of the ϵ phase from experimental data and DFT results in that: (1) there exists largely two Fe sites with similar fractions, and (2) Fe in those sites are likely low-spin Fe^{3+}.

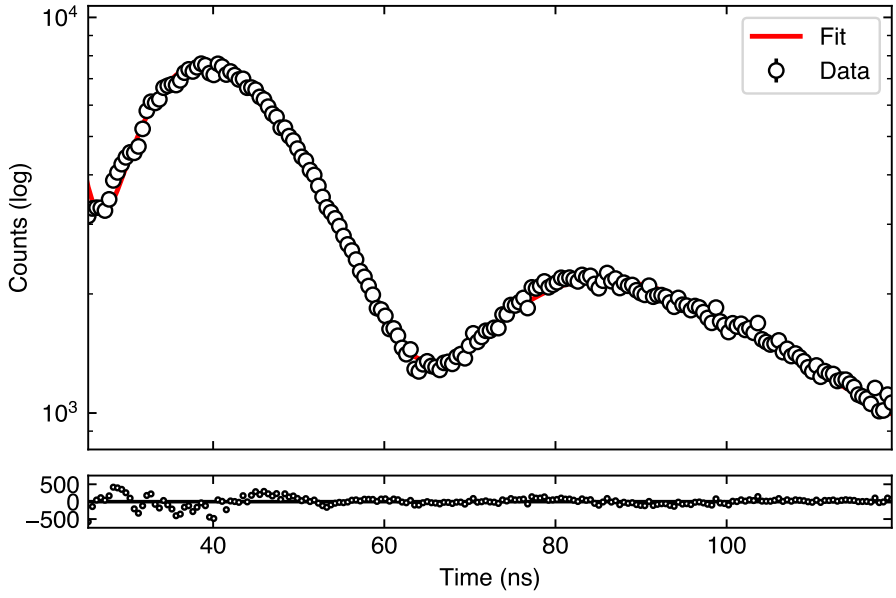

Figure 3.6: Synchrotron Mössbauer Spectrum of the η Phase.

The sample was synthesized at 62 GPa and 1600 K (circles, measured intensities; curves, fitted spectra). We show the fit residue at the bottom part of the figure.

Table 3.6: Fitting Results for the Mössbauer Spectrum of the η Phase.

We obtain a χ^2 of 4.3 for the fitting; Wt: fraction of the site; IS: isomer shift (mm/s) with respect to that of $FeSO_4 \cdot 7H_2O$ at 1 bar; QS: quadruple splitting (mm/s). The numbers in parentheses are the 1σ estimated uncertainties. A small amount of the ϵ phase was detected in diffraction pattern. Therefore, we subtracted the small effects of the ϵ phase by fitting the fraction of the phase while we fix other parameters of the ϵ phase ($Wt = 0.01$, $IS = -0.15$ mm/s, $QS = 1.34$ mm/s for site 1; $Wt = 0.03$, $IS = -0.78$ mm/s; $QS = 0.08$ mm/s; manuscript in preparation).

	site 1	site 2	site 3
Wt	0.53(2)	0.39(2)	0.03(2)
IS (mm/s)	0.11(5)	-0.13(5)	-0.51(5)
QS (mm/s)	1.80(3)	0.79(3)	0.17(3)

First-principles calculations were performed within the framework of density functional theory (DFT)(Hohenberg and Kohn, 1964; Kohn and Sham, 1965), as implemented in Vienna Ab initio Simulation Package (VASP) code (Kresse and Furthmüller, 1996). Projector augmented wave (PAW) potentials (Blöchl, 1994) were used in all the calculations to describe the interactions between core and valence electrons. Considering the good agreement between the experimental and the simulated lattice parameters in a Fe–O–H system in a previous study (Lu and Chen, 2018), we implemented Perdew Burke and Ernzerhof (PBE) functional(Perdew *et al.*, 1996) for the exchange-correlation interactions of electrons. Plane-wave basis with a cutoff energy of 500 eV and k-point sampling of $2\pi\times$ 0.025 Å^{-1} were employed to obtain the precise total energy at 0 K (without zero-point vibration) and 40 to 85 GPa (approximately to experimental pressures). We relaxed the crystal structure until all the stress forces of atoms were smaller than 0.01 eV/Å.

From the DFT calculation, we found that the crystal structure from calculations agreed well with the structure model from our experiments with a $P6_3/m$ space group with a starting composition $Fe_{12}O_{18}$. However, without H_2O in the crystal structure, the enthalpy of η-$Fe_{12}O_{18}$ was higher than ppv-Fe_2O_3, implying that the new η-$Fe_{12}O_{18}$ phase is thermodynamically less stable than ppv-Fe_2O_3, if H_2O is not included. From our experimental results, 0.5–1 mole of H_2O may exist in the η phase. Thus, we relaxed the crystal structure with 0.5 and 1 mole H_2O. We assumed that the channel could contain O and H in a ratio of 1:2.

After structural optimization, the $P6_3/m$ cell was retained in the $Fe_{12}O_{18.5}H$ if we ignore the H atom positions. However, when we relaxed the $Fe_{12}O_{19}H_2$, it transformed to a triclinic cell with $\alpha = 89°$, $\beta = 91°$, and $\gamma = 119.1°$. The magnitudes of the a and c parameters of the triclinic cell is in agreement with the hexagonal parent cell as shown in (Fig. 3.7). Overall, the unit-cell volume and the unit-cell parameters

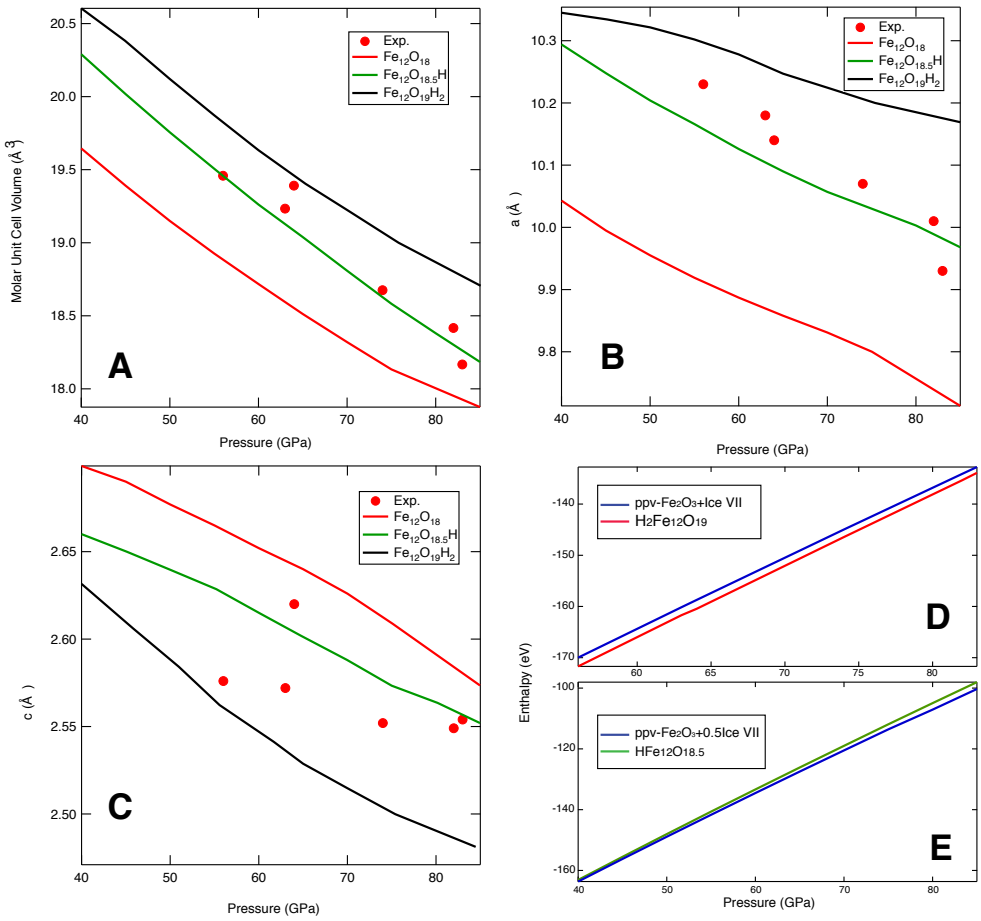

Figure 3.7: The Unit-cell Volume and Enthalpy of the η Phase from Our DFT Calculations.

The parameters are compared with our experimental results (Exp., red circles). The red, green, and black lines are for $Fe_{12}O_{18}$, $Fe_{12}O_{18.5}H$, and $Fe_{12}O_{19}H_2$, respectively, in A, B and C. The enthalpies of these compositions were also compared in D and E with ppv-Fe_2O_3 + Ice VII (blue).

observed in our experiments lie in between those of $Fe_{12}O_{18.5}H$ and $Fe_{12}O_{19}H_2$. The similarity in the unit-cell parameters supports our inference on 0.5–1 mole H_2O in the η phase from our experimental results.

The two crystallographic sites of Fe were also confirmed: two sites with 6 and 7 coordination numbers in the low-spin state which is consistent with our Mössbauer data. The O–H bonding at 80 GPa is 0.97 Å, where hydrogen lies in between the O–O atoms but asymmetrically in the channel at the four side edges of the unit cell in (Fig 2.) The hydrogen coordinate is (0,0, 0.59) and (0,0,0.36) with half occupancy at 80 GPa from calculations of $Fe_{12}O_{18.5}H$.

$Fe_{12}O_{19}H_2$ has a hydrogen position (0.96, 0.97, 0.18) off centered at 80 GPa and the O–H bonding distance is 0.97 Å. The Fe–O bonding distance in FeO_6 is 1.73–1.84 Å from calculations, which are comparable to the value we obtained from experiments (1.78–1.88 Å) at 80 GPa. The anisotropic Fe–O bond distances are required to form a channel that is also observed in the NAL phase(Miura *et al.*, 2000). The trigonal prism FeO_6 had the Fe–O bonding of 1.93–1.96 Å from calculation, while Rietveld refinements yielded 1.90–1.97 Å. The trigonal prism FeO_6 contain another Fe–O bonding with a distance of 2.03 and 2.05 Å in calculations and experimental results, respectively at 80 GPa. Overall, the Fe–O bonding from Rietveld refinements agrees with the DFT calculations.

The calculated enthalpy of the $Fe_{12}O_{19}H_2$ phase is lower than ppv-Fe_2O_3 and Ice VII, while $Fe_{12}O_{18.5}H$ has slightly higher energy (e.g., 48 meV/atom) than ppv-Fe_2O_3 + 0.5 Ice VII in (Fig. 3.7 D and E). However, considering high-temperature conditions in our experiments, the thermal energy (e.g. 138 meV/atom at 1600 K) is comparable to the energy difference evaluated at 0 K by DFT. At least, the close energy between the η phase and ppv-Fe_2O_3 + ice VII supports the existence of H_2O in the crystal structure of the η phase and its estimated H_2O content (0.5–1 mol).

We note that the exact description of strongly correlated electron systems, such as ppv-Fe_2O_3 and the η phase present here, is still challenging in DFT (Meng *et al.*, 2016). Also, the precise total energy calculations through DFT can be limited by the structural uncertainty derived from the varying ratios of H_2O and positions of extra O and H atoms in the η phase. However, our theoretical results generally align with our experimental results (both lattice parameters and energy differences) and support the hydrous η phase.

3.4 Conclusion

Despite its importance, transport of hydrogen to the Earth's deep interior remains uncertain. Our experiments found a new hexagonal iron hydroxide (η-$Fe_{12}O_{18+x/2}H_x$) between the stability fields of the ϵ- and pyrite-type FeOOH at 60–80 GPa and high temperatures. The new phase contains less H_2O, limiting the H_2O transport from the shallow to the deep mantle in the Fe–O–H system. The crystal structure of the new phase explains the enigmatic hexagonal phases observed in mantle-related chemical systems at higher pressures and temperatures: H-phase and HH-phase.

Therefore, we propose that the η phase is an important hydrous phase to consider in understanding the deep H_2O cycle because of its potential stability for a larger depth–temperature range through forming solid solutions with important chemical components in the lower mantle. The H_2O content in the η phase could also set a limit for the total H_2O content in the deep mantle. It is unlikely that the lowermost mantle would have an H_2O content higher than 0.16 wt% or 1600 ppm, assuming the weight content of iron oxide is 8 wt% in the mantle (McDonough and Sun, 1995).

Chapter 4

THE O-O BONDING AND HYDROGEN STORAGE IN THE PYRITE-TYPE PTO_2

4.1 Introduction

Several Pt oxides, such as PtO, β-PtO_2, and Pt_3O_4, have been synthesized through decomposition of chloroplatinic acid or compression to high pressures (Adams and Shriner, 1923; Muller and Roy, 1968; Moore Jr and Pauling, 1941; Range *et al.*, 1987). A multi-anvil study reported that PtO_2 synthesized at 17 GPa and 1273 K has a $Pa\bar{3}$ type structure (Shirako *et al.*, 2014). While the structure is very similar to pyrite, FeS_2, it was argued that $Pa\bar{3}$-type PtO_2 does not have sufficient anion-to-anion interaction expected in the pyrite type. It was instead assigned to a PdF_2-type structure found at high pressure (hp-PdF_2 type), which does not include any significant anion-to-anion interaction.

The argument against the anion-to-anion interaction in $Pa\bar{3}$-type PtO_2 is based on the bond distances constrained through Rietveld refinements of the powder X-ray diffraction patterns measured for the recovered sample at 1 bar and 300 K (Shirako *et al.*, 2014). Although higher-quality measurements are possible at 1 bar and the symmetry of the phase is higher (and therefore smaller number of parameters to fit), powder diffraction can still suffer from a range of problems for structure determination, including large degree of preferred orientation which could be severe in the materials synthesized at high pressures.

The significance of resolving this issue is that the anion–anion bonding in crystal structure could dramatically increase the bulk modulus of materials (also possibly

strength) and that pyrite-type PtN_2 has already been shown to contain pernitride unit, $[N–N]^{4-}$ and consequently possess a very high bulk modulus (347 GPa) (Zhao *et al.*, 2016; Salamat *et al.*, 2013; Crowhurst *et al.*, 2006; Wessel and Dronskowski, 2010). Can Pt dioxide with the same type of crystal structure possess an O–O bonding (similar to the N–N bonding in py-PtN_2) and a high bulk modulus? Very large bulk moduli have been documented in OsO_2 and RuO_2 in similar crystal structure (PdF_2 or pyrite type) (Haines *et al.*, 1998; Léger *et al.*, 1994; Lundin *et al.*, 1998). However, it still remains controversial whether the anion-to-anion interaction is responsible for the observations (Shirako *et al.*, 2014).

Strong anion-anion interaction has been also found in dichalcogenides (MQ_2 where M = Pt or Pd and Q = S or Se) with pyrite or distorted pyrite structures (Soulard *et al.*, 2004). Therefore, it is important to investigate a range of compounds with pyrite-type crystal structures.

Recently, pyrite-type FeO_2 has been synthesized from α–FeOOH at 92 GPa and 2050 K (Hu *et al.*, 2016). Subsequently, it was proposed that py-FeO_2 can be partially hydrogenated, (py-FeO_2H_x, $0 \leq x \leq 1$) (Hu *et al.*, 2017). However, some later studies (Nishi *et al.*, 2017; Yuan *et al.*, 2018) have questioned the stabilities of py-FeO_2 and its hydrogenated forms and instead argued for the existence of a fully hydrated form in a pyrite-type structure, py-FeOOH. These two views lead to dramatically different consequences for the deep planetary storage of volatiles. The stability of py-FeO_2H_x with the peroxide bonding (Hu *et al.*, 2016, 2017) will result in a release of hydrogen at high temperature, i.e., dehydrogenation. Consequently, the deep interior could store a large amount of oxygen in a form of peroxide unit. In contrast, if fully hydrated without a peroxide unit, py-FeOOH will be stable and therefore its thermal decomposition will lead to supply of H_2O instead, i.e., dehydration, in the deep planetary interiors (Nishi *et al.*, 2017).

4.2 Methods

We prepared pure Pt or α-PtO_2 (Alfa-Aesar) in a pre-pressed foil form. The foil was then loaded in a 90 μm diameter hole in a pre-indented rhenium gasket. We injected H_2O as a medium to the sample chamber and compressed in a symmetric-type diamond-anvil cell (DAC) (Table 4.1). Diamond anvils with a culet size of 200 μm were used to compress the samples to high pressure. A small chip of pure elemental gold was loaded near the PtO_2 sample foil for in-situ pressure measurements. For the Pt + H_2O samples (runs 101 and 203), we used the equation of state of Pt to calculate pressure from its measured unit-cell volume (Ye *et al.*, 2017). We placed several spacers less than 10 μm (either pure Pt or α-PtO_2) below and above the sample foil to form a layer of H_2O between the sample and diamond anvils for thermal insulation during laser heating.

We measured in-situ X-ray diffraction (XRD) patterns in the laser-heated DACs at beamline 13ID-D in the GeoSoilEnviroCARS (GSECARS) sector (Prakapenka *et al.*, 2008a) at the Advanced Photon Source. Monochromatic X-ray beam was focused to a beam size of $3\times4\,\mu m^2$ at the sample in the DAC. Two near-infrared laser beams (a wavelength of $\sim$1 μm) were focused on the sample through two opposite sides of DAC with a hot spot size of 20–25 μm diameter Temperatures for laser heating were calculated by fitting the measured thermal radiation spectra to the Planck equation from both sides of the sample after subtracting backgrounds. We maintained the same temperature for both sides of sample by adjusting laser power. The laser beams were aligned coaxially with the X-ray beam, in order to measure diffraction patterns at the center of the heating spot. We have collected diffraction data with an X-ray wavelength of 0.3344 or 0.4133 Å. The diffraction setup, including X-ray energy and detector tilts, was calibrated by measuring the diffraction patterns of a LaB_6

standard.

We used a Pilatus detector for 2D diffraction image measurements. In a typical run, we compressed the sample to a target pressure and then heated for 10 mins. After laser heating, we measured high-quality diffraction patterns after removing laser mirrors. X-ray exposure time varies between 1 and 5 seconds depending on the sample loading. We integrated the 2D images into 1D diffraction patterns in the Dioptas package (Prescher and Prakapenka, 2015). We performed phase identification and peak fitting to a pseudo-voigt profile shape function in the PeakPo package (Shim, 2017).

We have measured Raman spectra for the recovered samples from runs 101 and 417 at ASU. The Raman scattering was excited by a 532-nm wavelength beam from a frequency doubled Nd:YAG laser. Considering the reflectivity and absorption from the optical components in our Raman system and diamond anvils, the beam intensity should be less than 30 mW at the surface of the sample. We conducted measurements at spectral ranges of 400–1200 cm^{-1} for the lattice vibrations and 2900–3600 cm^{-1} for the OH modes, using a 1800 grooves/mm grating. The spectrometer was calibrated using the neon emission spectra. To remove the pixel-to-pixel sensitivity differences in the CCD detector, we measured a spectrum of a glass with known fluorescence intensities at different wavenumbers. Spectral data were collected for 200 seconds.

We performed density functional theory (DFT) calculations for the crystal structure and bulk modulus of py-PtO_2. All DFT calculations were conducted with periodic boundary conditions with a plane-wave basis set using the Vienna Ab-Initio Simulation Package (VASP) (Kresse and Hafner, 1993; Kresse *et al.*, 1996). Initial atomic coordinates for PtO_2 were obtained from the experimental results (space group: $Pa\bar{3}$, No. 205) (Shirako *et al.*, 2014). The projector augmented wave (PAW) method (Blöchl, 1994) as implemented by Kresse and Joubert (Kresse, 1999) are

used as the electron-ion interactions. The valence electron configuration for the Pt pseudopotential was $5p^6 5d^9 6s^1$. The exchange correlation functional parameterized in the generalized gradient approximation (GGA)(Langreth and Perdew, 1980) by Perdew, Burke, and Ernzerhof (PBE) (Perdew *et al.*, 1996) was used, with and without the Heyd-Scuseria-Ernzerhof (HSE) screened hybrid functional (Krukau *et al.*, 2006). The plane wave cutoff energy was set to 450 eV, and the stopping criteria for self-consistent loops were 1 meV per cell for electronic and ionic relaxation. The conventional cell for py-PtO_2 (4Pt and 8O atoms) is used in the structure relaxation and the EOS calculations with a $15 \times 15 \times 15$ Monkhorst-Pack (Monkhorst and Pack, 1976) k-point grid for GGA and a $5 \times 5 \times 5$ Monkhorst-Pack k-point grid for HSE. The volume and energy convergence of HSE are checked with $9 \times 9 \times 9$ Monkhorst-Pack k-point grid. The volume difference of relaxed crystal between $5 \times 5 \times 5$ and $9 \times 9 \times 9$ k-point grids is 0.003 Å^3/atom, and the energy difference between them is < 0.15 meV/atom. Therefore, the calculation results under $5 \times 5 \times 5$ k-point grids are converged to the given scales. The bulk modulus of $Pa\bar{3}$-type RuO_2 is also obtained from the same calculation approaches and settings to further compare the results from different potential functionals.

Table 4.1: Summary of Experimental Runs at High Pressure and High Temperature . SM: starting material, P: pressure, T: temperature.

Run#	SM	P (GPa)	T (K)	Product
101	Pt + H_2O	62(2)	1250–1900	py-PtO_2
203	Pt + H_2O	50(2)	1400–2100	py-PtO_2
417	α–PtO_2+H_2O	55(2)	1300–1500	py-PtO_2, py-PtO_2H_x

Rietveld refinements were performed in the general structure analysis system (GSAS-II).We refined phase fractions first, then atomic positions, lattice parame-

ters and spherical harmonic terms for preferred orientation. After reaching a good visual fit, we refined all the parameters together, in order to further reduce fit residue.

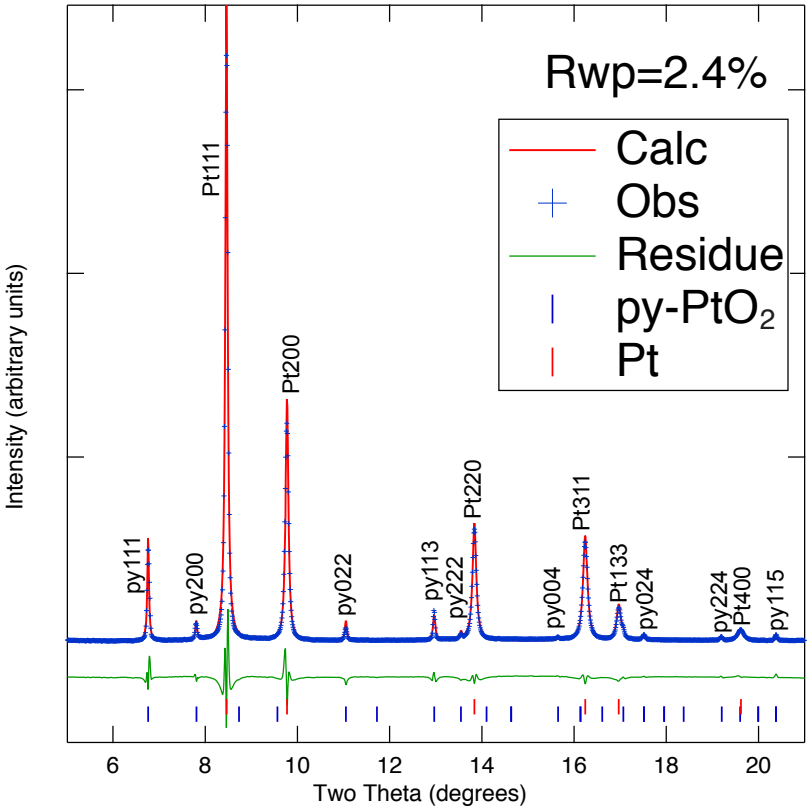

Figure 4.1: Rietveld Refinement of a Diffraction Pattern Measured for py-PtO_2 after Recovery to 1 bar and 300 K.

The unit cell parameter is: $a = 4.91103(1)$ Å. The shortest O–O bond distance is 2.13334(1) Å.

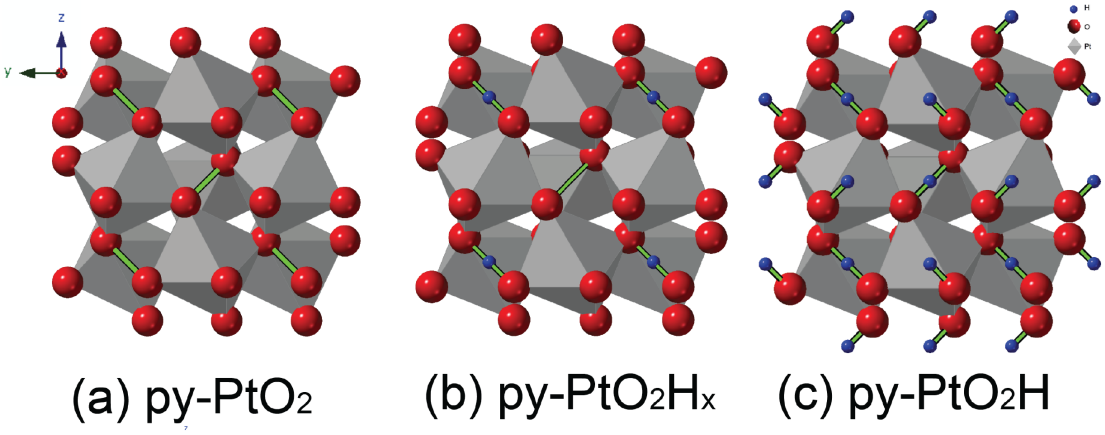

Figure 4.2: Crystal Structure Models of py-PtO_2 and Its Hydrogenated Forms. **a**, py-PtO_2, **b**, py-PtO_2H_x ($0<x<1$), and **c**, py-PtO_2H. The O–O bondings are highlighted as green lines in **a** and **b**. The hydrogen atom (blue spheres) may be inserted between the oxygen atoms in the hydrogenated form, i.e., **b** and **c**.

4.3 Results and Discussion

In our experiments in laser-heated diamond-anvil cell, several new peaks appeared in diffraction patterns within 10 min of heating for a Pt + H_2O starting mixture at 1250–1900 K and 60 GPa (run 101 in Tab. 4.1). These sharp peaks can be well indexed with a cubic unit cell. The existence of the 021 diffraction line at $\sim$9.2°2θ confirms a $Pa\bar{3}$-type structure for the new phase rather than a face centered cubic structure (Figure 4.3). During the laser heating, the peaks gained intensities but no additional lines appeared in the patterns. After quenching to 1 bar and 300 K, the diffraction pattern remained essentially the same except for the shifts in the peak positions to lower 2θ angles due to decompression, demonstrating that the new structure is quenchable to ambient conditions. For this pattern, we conducted Rietveld refinements (Toby and Von Dreele, 2013) on the crystal structure at 1 bar as shown in Figure 4.1. We obtained a unit cell volume of 118.45(1) Å^3. The shortest oxygen-to-oxygen distance was 2.13 Å (run 101 in Tab. 4.1).

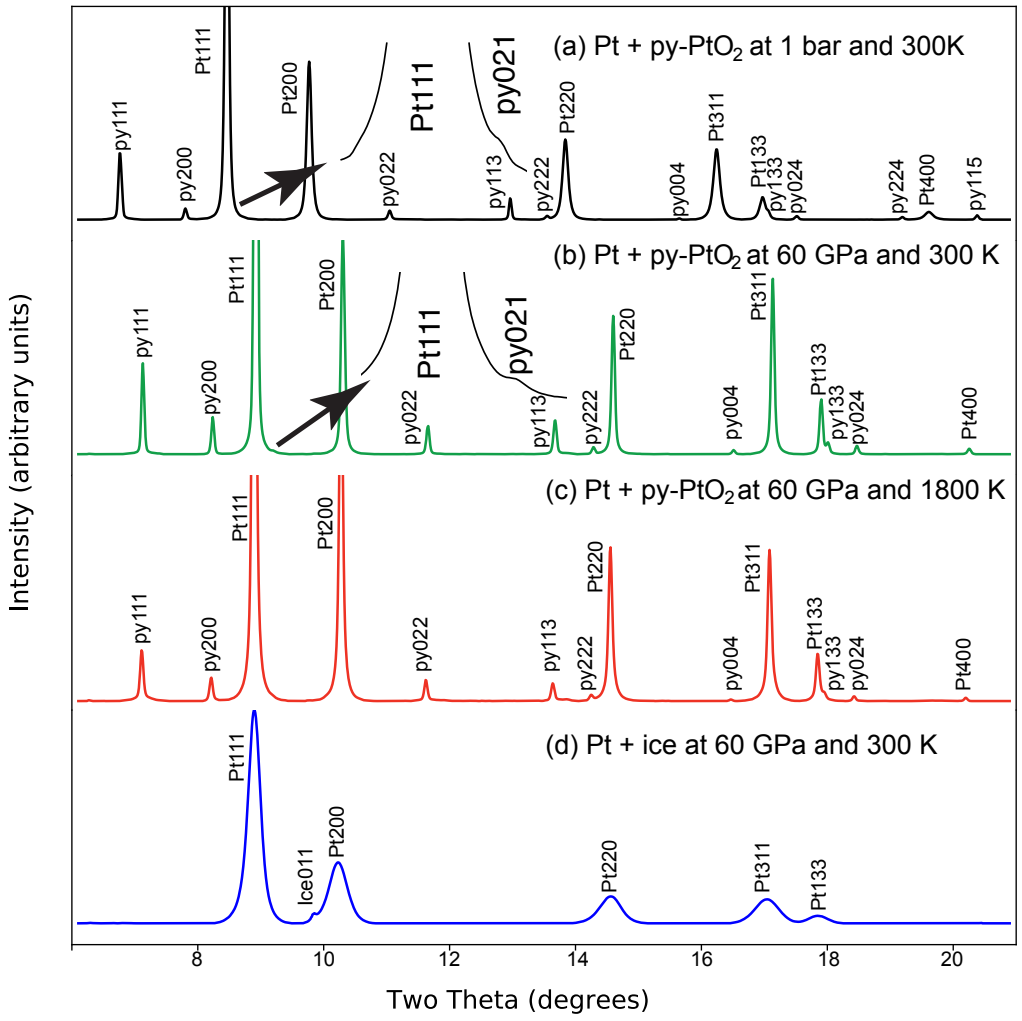

Figure 4.3: In-situ X-ray Diffraction Patterns Measured During an Experiment on a Pt + H_2O Starting Mixture at 60 GPa.

d, before **c**, during, and **b** after laser heating to 1250–1800 K. **a**, We also measured diffraction patterns after decompression at 1 bar and 300 K. The wavelength of the X-ray beam is 0.3344 Å. The insets show the 021 peak of py-PtO_2.

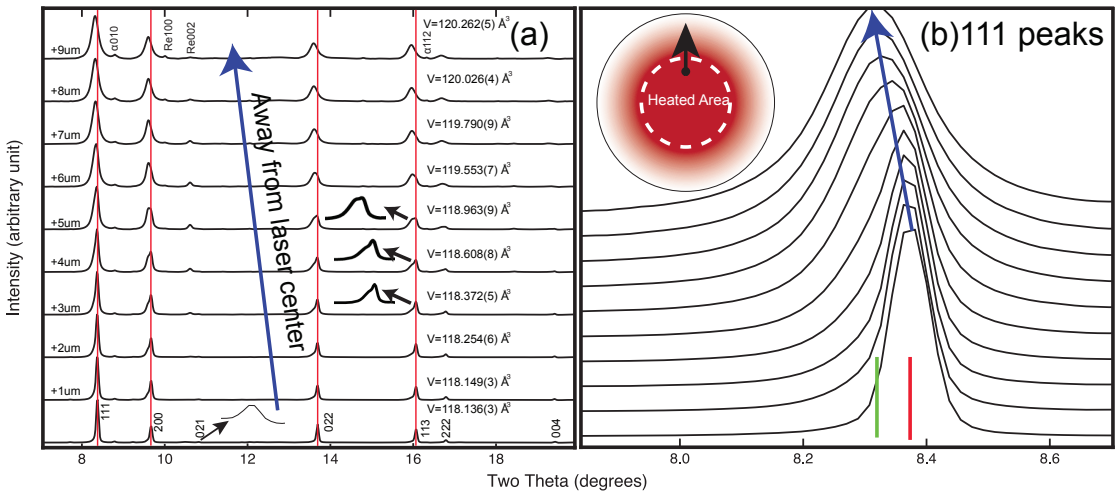

Figure 4.4: X-ray Diffraction Patterns of py-PtO_2 and py-PtO_2H_x.

a diffraction measurements of py-PtO_2 at 1 bar and 300 K. The sample was synthesized at 50 GPa and 1400 K. The bottom most diffraction pattern is for the hot spot and the rest of the patterns are from areas outside of the hot spot as schematically shown in an inset in **b**. Diffraction peaks from α-PtO_2 and the Re gasket are also labeled. **b** the 111 peaks of py-PtO_2 also measured at different distances from the laser-heated spot.

In a separate experiment (run 417) with an oxidized starting material instead, α-PtO_2 + H_2O, we also observed the formation of the same phase at 1300–1500 K and 55 GPa. The sample was also successfully quenched to 1 bar and 300 K (Figures 4.4. Within the laser-heated area, all the spots we examined showed a zero pressure unit-cell volume of 118.136±0.003 Å^3. This value is essentially the same as the value reported for $Pa\bar{3}$-type PtO_2 synthesized at 17 GPa and 1273 K under anhydrous conditions (Shirako *et al.*, 2014), 118.1418±0.0002 Å^3. However, we found a systematically higher unit-cell volume (by 0.3%) for the same phase synthesized from the Pt + H_2O starting material, 118.45±0.01 Å^3 (Figure 4.1) This volume is similar to that reported for $Pa\bar{3}$-type PtO_2 synthesized at lower pressure (Shirako *et al.*, 2014), but larger than our samples from run 417 considering the estimated uncertainty. The larger unit-cell volume of the $Pa\bar{3}$-type PtO_2 phase in run 101 likely results from hydrogen atoms incorporated into the crystal structure, which we will discuss later.

Possible O–O bonding has been inferred from the O–O distances measured from X-ray diffraction (Haines *et al.*, 1996). The shortest O–O distance from our Rietveld refinements is 2.13 Å at 1 bar (Figure 4.1). Our O–O distance is slightly smaller than the value reported for the $Pa\bar{3}$-type PtO_2 phase synthesized at lower pressures under anhydrous conditions (Shirako *et al.*, 2014). However, as we discussed earlier, it is challenging to constrain the bond distance reliably and the inference to the existence of bonding is indirect and uncertain.

Raman spectroscopy is sensitive to covalent bonds. In pyrite-type PtN_2, N–N bonding had been successfully identified with the technique (Crowhurst *et al.*, 2006). The quenchability of $Pa\bar{3}$-type PtO_2 allows us to measure the Raman spectra reliably at 1 bar. Raman spectra show two intense vibrational modes (860 and 748 cm^{-1}) together with two much weaker modes (674 and 891 cm^{-1} in Figure 4.5). An intense mode at 860 cm^{-1} has a frequency near the the O–O symmetric stretch mode (A_g)

(750–850 cm^{-1}) reported for a number of solid peroxides (Eysel and Thym, 1975). For hydrogen peroxide, the mode exists at 880 cm^{-1}, again supporting the assignment of the mode at 860 cm^{-1} in $Pa\bar{3}$-type PtO_2 to O–O bonding (therefore now we call pyrite-type PtO_2 instead of $Pa\bar{3}$-type PtO_2). The E_g mode at 748 cm^{-1} has also been documented in pyrite-type phases (Crowhurst *et al.*, 2006). We also measured Raman spectra for α-PtO_2, which was one of our starting materials. α-PtO_2 has two modes at 505 and 544 cm^{-1}. Thus, none of the existing Raman modes for py-PtO_2 are related to starting α-PtO_2. It is notable that the Raman spectrum of py-PtO_2 is very similar to that of py-PtN_2(Crowhurst *et al.*, 2006). It is likely because the $[N–N]^{4-}$ bonding (Wessel and Dronskowski, 2010) is isoelectronic to $[O–O]^{2-}$. Therefore, our Raman data further support the pyrite type for the high-pressure polymorph of PtO_2. A former study assigned hp-PdF_2 as a possible structure for $Pa\bar{3}$-type PtO_2 (Shirako *et al.*, 2014). However, the study did not measure Raman spectra for the sample and the synthesis conditions are different from ours: much higher pressure and hydrous conditions in our study.

In laser-heated diamond-anvil cell, the size of the heated area is limited, in our case 20–25 μm in diameter. Outside of the heated area, temperature decreases with distance and reaches ultimately 300 K at a sufficient distance (inset in Figure 4.4). We measured diffraction patterns as we moved away from the heating area for the sample recovered from run 417. In Figure 4.4, the bottom most diffraction pattern is for the hot spot and the rest of the patterns are from areas outside of the hot spot as schematically shown in an inset in b. With an increase in distance, temperature should decrease roughly by 50–100 K/μm. The diffraction lines of the py-PtO_2 shift to lower 2θ angles (or higher d-spacings) with an increase in distance from the heated area, suggesting an increase in unit-cell volume at lower temperature spots (Figure 4.4). For example, at a spot 9 μm away from the heated area (estimated temperature of

500–1000 K during heating), we found the largest unit-cell volume (1.6% higher than that at the heated area) for the py-PtO_2 at 1 bar and 300 K (Prakapenka *et al.*, 2008a). While we move out of the heated spot, we found 2–3 additional diffraction lines. They can be indexed with the peaks expected for unreacted α-PtO_2 and Re (gasket). We note that those peaks did not exist within the heated area at high pressure.

At pressures above ∼80 GPa, FeO_2 and FeOOH are shown to have the same crystal structure, pyrite type. However, py-FeOOH has a ∼1.6 Å^3/f.u. higher volume than py-FeO_2, suggesting a volume expansion by hydrogen incorporation in the crystal structure (Hu *et al.*, 2016; Nishi *et al.*, 2017). Therefore, we can attribute the volume difference found between the cold and hot areas in run 417 to the existence of hydrogenated py-PtO_2 at low temperature areas (py-PtO_2H_x).

The py-PtO_2 sample was examined further with Raman spectroscopy (Figure 4.5c). At the lower-temperature areas, we detected two peaks at 3255 and 3550 cm^{-1} in the O–H stretching vibration region at 1 bar. The wavenumber range is well known for the O–H vibration in a range of compounds with hydroxyl group. The existence of those two modes is direct evidence for the structurally incorporated hydrogen bonded with oxygen atoms in py-PtO_2. Hydrogen may attack the O–O bonds in pyrite-type structure and be incorporated there at the center of the O–O bond (i.e., a bond symmetrization), as suggested in computations (Zhu *et al.*, 2017; Tsuchiya and Tsuchiya, 2011; Nishi *et al.*, 2017). Hydrogen bond symmetrization has also been observed in high-pressure H_2O ice (Goncharov *et al.*, 1996) where hydrogen is bonded with two oxygen atoms in contrast to single oxygen atom at 1 bar in water. The O–H stretching vibration frequency for such configuration is expected to be much lower (Tsuchiya *et al.*, 2008). However, we note that our Raman measurements were conducted for the samples metastably decompressed to 1 bar. Therefore, even if symmetrized O–

H–O existed at high pressure, the hydrogen atom can move away from the center position during decompression and consequently the O–H vibrational frequency can be significantly higher at 1 bar.

The lattice modes from the lower-temperature areas also show systematic shifts to lower frequencies (Figure 4.5c). Such decreases can be interpreted as a consequence of hydrogen incorporation, because hydrogen will likely be located between the oxygen atoms in the structure, weakening the O–O bonding. An additional mode was found in this sample at 690 cm^{-1}. Pyrite type has five Raman active modes (Vogt *et al.*, 1983) and this may be the fifth mode which was not observed in our much less hydrogenated py-PtO_2 sample (Figure 4.5a). It is feasible that hydrogen incorporation and consequent distortion in the crystal structure may make the mode more visible in more hydrogenated py-PtO_2. Therefore, our Raman results support our interpretation for the observed the gradual unit-cell volume increase in XRD: an increase in hydrogenation of py-PtO_2 at lower temperatures (py-PtO_2H_x).

From the observations of the unit-cell volume lying between those expected for py-FeO_2 and py-FeOOH, incorporation of varying amounts of hydrogen has been inferred for py-FeO_2 (Hu *et al.*, 2017). Such comparison is only possible at pressures above 80 GPa for py-FeO_2, because of its limited stability at lower pressures. A later study did not find such volume behaviors (Nishi *et al.*, 2017) and argued that other factors, such as deviatoric stresses and pressure gradient, in high pressure experiments can contribute to the observations. In the case of PtO_2, owing to the quenchability of the pyrite-type phase to 1 bar, we were able to characterize such volume behaviors more reliably in the absence of stress. More importantly, the existence of hydrogen or hydroxyl is probed directly through Raman spectroscopy for py-PtO_2, while such measurements remain to be performed for py-FeO_2.

Because the unit-cell volume is unknown for fully hydrogenated py-PtO_2H, it is

difficult to estimate the degree of hydrogenation of our py-PtO_2 samples through the measured unit-cell volumes. However, owing to the quenchability, more direct quantification of hydrogen can be performed in future experiments for py-PtO_2H through a series of hydrothermal syntheses at different temperatures. The peak splittings found in some of the diffraction patterns in Figure 4.4a are likely due to the existence of py-PtO_2 phases with different amounts of hydrogen. It remains an interesting question whether py-PtO_2 can be hydrogenated gradually or stepwise (existence of a few energetically favored amounts for hydrogen). However, the behavior of the most intense 111 peak shown in the figure seems to indicate a more gradual change in the amount of hydrogen in py-PtO_2. The most robust observation for PtO_2 is the existence of both pyrite-type structured peroxide and its hydrogenated version.

We measured the unit-cell volume of py-PtO_2 synthesized in runs 101 and 203 during decompression from 65 GPa to 1 bar. The data were fit to the Birch-Murnaghan equation (Birch, 1947) with the measured volume at 1 bar (V_0) and a fixed pressure derivative of bulk modulus of 4. We found indeed a high bulk modulus of 314(4) GPa (Table 4.2 and Figure 4.6). Because these samples are slightly hydrogenated (inferred from their larger unit-cell volume at 1 bar) and hydrogenation may decrease the bulk modulus (Nisr *et al.*, 2017a), we believe the bulk modulus for dehydrogenated form, py-PtO_2, can be even greater. The value we found for py-PtO_2H_x is similar to the high bulk modulus of pyrite structured materials, in particular PtN_2 (347 GPa) (Crowhurst *et al.*, 2006).

We calculated the bulk modulus of py-PtO_2 using density functional (DFT) theory (both GGA and HSE; Table 4.2). We also calculated for RuO_2 in the $Pa\bar{3}$ structure which is also known to have a high bulk modulus (Haines *et al.*, 1996). We note that the $Pa\bar{3}$-type RuO_2 has the same crystal structure as py-PtO_2, but the existence of strong O–O interaction is still under debate (therefore, $Pa\bar{3}$-type RuO_2). Our

calculation results of the relaxed crystal structures show good agreements with both experiments and other calculations (Shirako *et al.*, 2014; Haines *et al.*, 1996; Jain and Ong, 2013; Tse *et al.*, 2000). However, the bulk moduli calculated by HSE are 50–80 GPa larger than by GGA for both $Pa\bar{3}$-type RuO_2 and py-PtO_2. This discrepancy is because the calculated energies by GGA and HSE have large discrepancy from to the use of hybrid functional in HSE. Although still lower, HSE provides a bulk modulus in better agreement with the experimentally measured value for the $Pa\bar{3}$-type RuO_2 (Haines *et al.*, 1996). It was also found that the bulk modulus of py-PtO_2 from HSE agrees better with our experimental value and therefore support a high bulk modulus of py-PtO_2.

4.4 Implications

Through Raman spectroscopy and X-ray diffraction for the recovered samples, we have shown that py-PtO_2 has a strong O–O interaction. In addition, we showed that py-PtO_2 can store hydrogen. Together with the similar case suggested for py-FeO_2H_X (Hu *et al.*, 2017, 2016), it can be hypothesized that the energy difference may be sufficiently small between the peroxide configuration, $[O–O]^{2-}$, and the symmetrized hydrogen configuration, $[O–H–O]^{3-}$ in the transition metal dioxides (Figure 4.2c). In addition, the flexible oxidation states (+2, +3 and +4 respectively) of transition metals should also contribute to such behaviors. Considering the fact that the $Pa\bar{3}$ type phase has already been found in some transition metal dioxides (Shirako *et al.*, 2014), it is of particular interest if this behavior can be common among the transition metal dioxides.

It is of interest if the hydrogen atom in the pyrite-type transitional dioxides can be symmetrized at high pressure. The oxygen-oxygen bonding distance at 1 bar is about 2.13 $\mathring{A}$ in py-PtO_2, and the distance at 80 GPa is 1.94 $\mathring{A}$ in py-FeO_2 (Hu *et al.*, 2016).

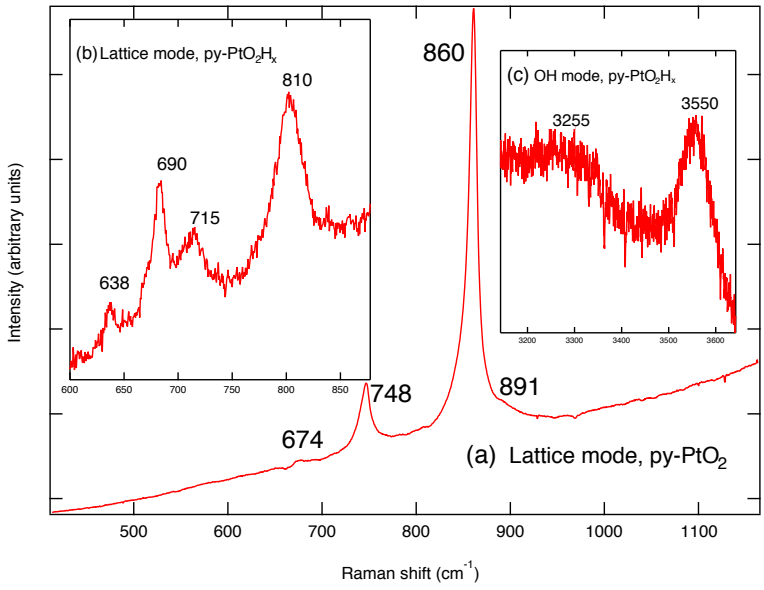

Figure 4.5: Raman Spectrum of the Recovered PtO_2 Samples at 1 bar and 300 K. **a**, the lattice mode region for py-PtO_2 from run 101 with the smallest V_0, and **b** the lattice mode **c** the OH mode regions for py-PtO_2H_x from run 417.

These distances are larger than the O–O dimmer distance (1.49 $\mathring{A}$) at 1 bar (Eysel and Thym, 1975), which might be caused or favored by having hydrogen atom between the oxygen atoms in the crystal structure. The $[O–H–O]^{3-}$ could be symmetrized at high pressure as the symmetric hydrogen bonding will have an O–O distance of 2.42 $\mathring{A}$ for the case of H_2O ice (Goncharov *et al.*, 1996). However, with decompression, it is more likely to have asymmetric regular hydrogen bonding as indicated in the case of high-pressure H_2O ice (Goncharov *et al.*, 1996) and our Raman observation for py-PtO_2H_x.

PtO_2 with a $Pa\bar{3}$ structure has been synthesized at pressures as low as 17 GPa (Shirako *et al.*, 2014). Given the fact that the stability of the lower-pressure polymorphs had been so far demonstrated only up to 6–7 GPa (Range *et al.*, 1987), py-PtO_2 could

be made at even lower pressures than 17 GPa, opening up possibilities for synthesizing larger amounts of the sample. The most intriguing property we found is the partial hydrogenation of py-PtO_2 together with the incompressibility. The synthesis of the partially hydrogenated version of py-PtO_2 was demonstrated to be straightforward: hydrothermal synthesis with temperature control as shown in our experiments. The high incompressibility of py-PtO_2 makes such hydrogen storage capability even more intriguing. Furthermore, the partial hydrogenation may open up the possibility to control the properties of py-PtO_2, such as strength, through hydrogenation (i.e., through weakening of the O–O bonding). It is important to further investigate if hydrogen storage can be found in other transition metal dioxides or even dinitrides, particularly with lighter transition metals, with anion-anion bonds in future studies. For designing such materials, it will be key to understand the electronic configurations of the cations and the anion-anion dimers in pyrite-type structures. While such efforts have been made recently for py-FeO_2 (Liu *et al.*, 2019; Boulard *et al.*, 2019), because of its limited stability only at high pressures, detailed investigation is difficult. The quenchability and the accessible synthesis pressure for a large amount of sample in py-PtO_2 will provide unique opportunities to understand the properties we discussed above in much more detail at room conditions.

If such anion-to-anion covalency enhances with compression, it would also have implications for Earth and the large Earth-like exoplanets, super-earths. Together with the implications for the oxygen and hydrogen geochemistry discussed in a previous study (Hu *et al.*, 2016), if such behavior is common in transition metal dioxides, the increased covalent anion-to-anion bonding at high pressure will impact the geochemical behaviors, such as partitioning of transition metals (Ir, Ru, Rh, and Os) which are often used as tracers to understand the deep processes. Oxygen is the main anion for the phases stable in such planets. Therefore, the possibility of increased co-

valency would affect the equations of state of the phases (such as compressibility) and consequently alter the mass-radius relations which are fundamental tools in inferring the composition of the exoplanets in astrophysical measurements. It can also imply that the geochemical cycle of the super-earths could be fundamentally different from that of smaller versions (e.g., Earth) if such pressure driven processes (dimerization of anions) can alter the chemical behaviors of materials at high pressures.

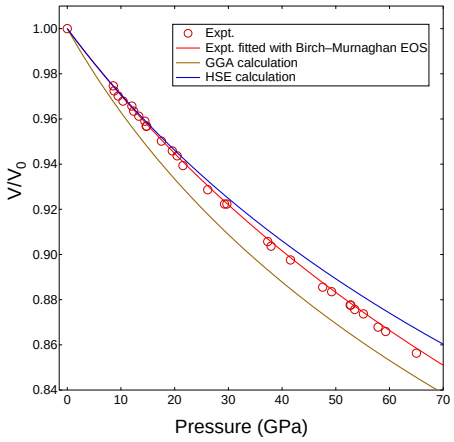

Figure 4.6: Compressibility of the py–PtO_2.

We plotted the normalized unit-cell volume with respect to the volume at 1 bar, V/V_0, as a function of pressure for pyrite-type PtO_2.The red circles are experimentally measured volumes at high pressure and 300 K, and the red curve is the fitting result with the Birch-Murnaghan equation.The yellow and blue curves are the compression of py-PtO_2 from our GGA and HSE calculations, respectively.

Table 4.2: The Equation of State and Crystal Structure of py-PtO_2 Constrained From Our High-pressure Experiments (Expt) and Density Functional Theory (DFT) Calculations (Calc).

We also performed similar calculations for $Pa\bar{3}$-type RuO_2 for comparison. We present other works for comparisons (Haines *et al.*, 1996; Jain and Ong, 2013; Tse *et al.*, 2000); a_0: unit-cell parameter, V_0: unit-cell volume, O(8c): the fractional coordinate for O in 8c, (x, x, x), B_0: bulk modulus, and B_0': pressure derivative of bulk modulus at 1 bar (* fixed during fitting).

	a_0 ($\AA$)	V_0 ($\AA^3$)	O(8c)	B_0 (GPa)	B_0'
Pyrite ($Pa\bar{3}$)-type PtO_2					
Expt(Shirako *et al.*, 2014)	4.91	118.1	0.34	-	-
Expt, this work	4.91	118.3	0.375	314	4.0*
Calc (GGA)(Jain and Ong, 2013)	5	125	0.341	-	-
Calc (GGA), this work	4.97	122.7	0.345	237	5.9
Calc (HSE), this work	4.89	116.1	0.343	312	5.3
$Pa\bar{3}$-type RuO_2					
Expt(Shirako *et al.*, 2014)	4.85	114.2	0.35	-	-
Expt(Haines *et al.*, 1996)	4.83	112.8	0.347	399	3.5
Calc (GGA)(Jain and Ong, 2013)	4.9	117.5	0.351	-	-
Calc (GGA)(Tse *et al.*, 2000)	4.88	116.5	0.344	299	3.9
Calc (GGA), this work	4.88	116	0.35	279	4.8
Calc (HSE), this work	4.81	111.3	0.351	326	4.8

4.5 Conclusion

We have synthesized pyrite-type PtO_2 (py-PtO_2) at 50–60 GPa and successfully recovered it at 1 bar. The observed O–O stretching vibration in Raman spectra provides direct evidence for inter-oxygen bonding in the structure. We also identified the O–H vibrations in py-PtO_2 synthesized from the low temperature areas, indicating hydrogenation, py-PtO_2H_x ($x \leq 1$). Diffraction patterns are consistent with a range of degrees of hydrogenation controlled by temperature. We found that py-PtO_2 has a high bulk modulus, 314 ± 4 GPa.

Chapter 5

COMPRESSIBILITY AND CRYSTAL STRUCTURE OF $CASIO_3$ PEROVSKITE AT 28–62 GPA AND 300 K UNDER QUASI-HYDROSTATIC STRESS CONDITIONS

5.1 Introduction

Perovskite-structured $CaSiO_3$ (CaPv) is stable from the transition zone to the lowermost mantle (Shim *et al.*, 2000b; Ohta *et al.*, 2008), and it is believed to be the third most abundant mineral (5–7 wt%) in the pyrolitic composition of Earths lower mantle (Kesson *et al.*, 1998b; Murakami, 2005). Mid-oceanic ridge basalt (MORB) in subducting slabs contains ∼23 wt% of CaPv in the lower mantle, becoming similar to the amount of bridgmanite∼35 wt% (Hirose *et al.*, 2005b; Ricolleau *et al.*, 2010).

Existing studies are in agreement in that CaPv has a cubic structure at high temperature (>500 K) (Komabayashi *et al.*, 2007; Noguchi *et al.*, 2013), while it has a non-cubic unit cell at low temperature (T) and high pressure (P) (Shim *et al.*, 2002; Stixrude *et al.*, 1996a). However, there remains a significant discrepancy between computations and experiments on the compressibility and the crystal structure of CaPv at high P and low T. It was believed that CaPv adopts a cubic structure ($Pm\bar{3}m$) at lower-mantle pressures (Liu and Ringwood, 1975; Mao *et al.*, 1989; Tamai and Yagi, 1989; Wang *et al.*, 1996). Tetragonally distorted CaPv was first predicted by *ab initio* calculations with the $I4/mcm$ space group (Stixrude *et al.*, 1996a). The discrepancy with experiments was explained by a subtle distortion of CaPv, the magnitude of which is smaller than the resolution of energy-dispersive diffraction technique used in earlier experiments. The proposed distortion in the crystal struc-

ture of CaPv results from rigid SiO_6 octahedral rotation around the tetragonal c axis (Stixrude *et al.*, 2007).

Using high-resolution angle dispersive diffraction techniques, Shim *et al.* (2002) found that CaPv has a non-cubic unit cell at 28–62 GPa and 300 K. However, they found that the peak positions and intensities of split peaks are more consistent with a longer a-axis than the c-axis, which is opposite to what is expected from the theoretically predicted crystal structure based on octahedral rotation. The longer a-axes cannot be explained by simple octahedral rotation and is more consistent with the SiO_6 octahedra with internal distortion (oblated octahedral shape). However, they could not measure the intensities of entire Debye rings due to the limited aperture of the DAC design they used to measure low d-spacing (or high diffraction angle) peaks at low X-ray energy. The experimental observation has been further confirmed by later experiments where XRD patterns show similar splitting of the cubic CaPv 200_C peak (subscript "C" represent Miller index for a cubic perovskite unit cell) at 27–72 GPa (Komabayashi *et al.*, 2007). Using a peridotitic composition, Ono *et al.* (2004) studied the tetragonal to cubic phase transition in CaPv, and also obtained non-cubic CaPv at 38–106 GPa and 300 K. Starting with a MORB composition, Hirose *et al.* (2005b) showed non-cubic CaPv upon T quench up to 134 GPa. Thus, the distortion in CaPv is also observed in multi-component systems in the lower mantle. These studies have shown that a lower angle line of split 200_C has more intensity, which is consistent with a tetragonal structure with the octahedral distortion suggested by Shim *et al.* (2002). A multi-anvil press experiment identified an orthorhombic CaPv up to 20 GPa and 1600 K (Uchida *et al.*, 2009). However, such low symmetry phase in CaPv has not been identified at higher pressures.

Later *ab initio* studies have confirmed the earlier theoretical study that the tetragonal CaPv structure is caused by octahedral rotation not by direct distortion of the

SiO_6 octahedra (Stixrude *et al.*, 2007). Some theoretical studies suggested an orthorhombic CaPv at low T (Magyari-Köpe *et al.*, 2002). However, they are still induced by the octahedral rotation. Therefore, the crystal structure of CaPv at high P and low T remains controversial.

Shim *et al.* (2002) reported a bulk modulus of 256 GPa for CaPv at 300 K. Ricolleau *et al.* (2009) shows a similar bulk modulus of 244 GPa using pyrolitic composition as a starting material. Noguchi *et al.* (2013) extrapolating cubic CaPv high-T EOS got a smaller bulk modulus 225 GPa. Although a few computational studies have reported similar bulk modulus values (Stixrude *et al.*, 2007; Caracas *et al.*, 2005; Magyari-Köpe *et al.*, 2002; Zhang *et al.*, 2006), a much lower bulk modulus has been reported, 216–228 GPa, by other computational studies (Akber-Knutson *et al.*, 2002; Chizmeshya *et al.*, 1996; Magyari-Köpe *et al.*, 2002; Jung and Oganov, 2005, Tab. 5.1). Such differences existing in the literature (21%) introduce severe uncertainties in the seismic velocities of CaPv in the mantle, in particular Ca-rich heterogeneities, such as MORB.

The measured crystal structure and equation of state (EOS) for Ca-Pv could be sensitive to deviatoric stresses in diamond-anvil cell (DAC). Most experimental studies on CaPv have been conducted in DACs where a pressure medium plays an important role for the stress conditions of the sample. Earlier studies used Ar (Shim *et al.*, 2002) or MgO (Kurashina *et al.*, 2004; Komabayashi *et al.*, 2007) as a pressure medium, and some even conducted without a pressure medium (Ono *et al.*, 2004, 2005), and they all observed non-cubic CaPv upon T quench. Although most of the experiments conducted laser annealing and therefore reduced the deviatoric stress in a DAC, 40–80% of stress can be reintroduced upon T quench using MgO as a pressure medium (Kavner and Duffy, 2001). The deviatoric stress could be particularly severe problem for the compressibility and crystal structure of CaPv, because compu-

tational studies have shown that free energy difference among competing structures are very small (Caracas *et al.*, 2005). In this study, I use Ne as a pressure medium combined with laser annealing to 1700–2300 K in order to ensure much reduced deviatoric stresses and therefore measure the crystal structure and compressibility of CaPv under quasi-hydrostatic stress conditions.

5.2 Experimental Procedures

We synthesized a $CaSiO_3$ glass using the laser levitation method (Tangeman *et al.*, 2001). Ca/Si molar ratio for the starting glass material is confirmed to be 0.993 ± 0.009 by JXA-8530F electron probe microanalyzer (EPMA) integrated with wavelength dispersive X-ray spectrometer (WDS) at Arizona State University. We used 400 μm culet diamonds for experiments with a peak pressure less than 35 GPa, and 200 μm culet diamonds were used above this pressure. The glass starting material was ground and mixed with 10 wt% pure platinum. The sample powder was pressed to a foil and loaded into the Re gasket hole on one side of the cutlets. Several spacers less than 10 μm were made from pure $CaSiO_3$ glass and placed below and above a sample foil to form a layer of Ne between sample and diamonds for thermal insulation. We used platinum as an internal pressure standard (Dewaele *et al.*, 2004) and a laser absorber. A Re gasket was pre-indented and drilled, and then placed between two aligned diamond cutlets. All experiments have been performed in symmetric-type DACs. We used Ne as a pressure medium, and loaded using the gas-loading system at the GSECARS sector (Rivers *et al.*, 2008). In one experiment, a sample foil was loaded without any medium to test how deviatoric stress can impact the crystal structure of CaPv. These data points were not used in the EOS fit.

We measured XRD patterns at in-situ high P–T in the laser heated DAC at beamline 13ID-D in the GSECARS sector (Prakapenka *et al.*, 2008b) and beamline 16ID-B

in the HPCAT sector (Meng *et al.*, 2006) at the Advanced Photon Source. Monochromatic X-ray beams with beam sizes of 3×4 and 5×6 μm^2 at GSECARS and HPCAT, respectively, were focused on the sample and the diffraction patterns were collected using a Mar-CCD detector. Near-infrared laser beams ($\sim$1 μm wavelength) were focused on sample with a hot spot size of 20–25 μm^2 and were aligned coaxially with the X-ray beam. In order to achieve the maximum resolution for the detection of the subtle peak splitting, we have optimized X-ray energy and detector-sample distance. The maximum resolution was achieved at an X-ray energy of 25 keV and a detector distance of 249.92 mm. Temperatures were calculated by fitting thermal radiation spectra to the Planck equation from both sides of the sample after subtracting the effects of the optical systems.

Prior to compression and heating, the amorphous state of $CaSiO_3$ glass was confirmed by XRD. In a typical experiment, we compressed the sample to target pressures at 300 K, and then heated a spot on the sample foil for about 5 minutes. We increased the laser power quickly to reach the target T (1700–2300 K) in less than 1 minute to avoid kinetics problems. Several XRD patterns were measured during and after heating. CaPv forms within 1 minute upon heating above 1700 K and diffraction patterns of CaPv remain essentially the same during heating.

The software package Dioptas (Prescher and Prakapenka, 2015) was used to integrate the diffraction images to diffraction patterns. We identify phases by the software XPEAKPO, and full width at the half maximum (FWHM) of XRD peaks were measured by XPEAKFIT. The diffraction peaks were fitted with pseudo-voigt profile to obtain the peak position. The data obtained from the GSECARS and HPCAT beamlines agreed well with each other for the peak positions and intensities of CaPv.

Rietveld refinements of XRD patterns was performed using the general structure analysis system (GSAS) combined with EXPGUI (Toby, 2001). We obtained lattice

parameters and atomic positions of Ca, Si and O for $P4/mmm$ and $I4/mcm$ crystal structures from Tanaka *et al.* (1993); Caracas and Wentzcovitch (2006). The starting lattice parameters was calculated from XPEAKPO. We defined the background for each diffraction pattern with 14 terms in Chebyshev polynomial. We used the same background parameters for fitting $I4/mcm$ and $P4/mmm$ structure to help us compare which structure fit experimental XRD patterns better. We refined phase fractions first. Then we fit atomic positions and lattice parameters. Each step, we only refine one parameter, and we refine all parameters from above simultaneously until we get a good fit between calculated and observed diffraction patterns. Then we fixed all parameters except for profile terms. We gradually increase the terms for different phases in peak shape function. Subsequently, we only refine spherical harmonic terms for preferred orientation. After reaching a good visual fit, we refine all terms together to achieve smaller residuals after background subtraction, $R_{wp-bknd}$. For the purpose of comparing fitting from different CaPv structures, we used the same parameters for Pt and Ne in the same pattern. Thus differences in residues only come from different structures of CaPv.

5.3 Results

Although a few different crystal structures have been proposed for CaPv, we focus mainly on resolving the differences among two cases: octahedral distortion ($P4/mmm$) (Shim *et al.*, 2002) and octahedral rotation (such as $I4/mcm$) (Stixrude *et al.*, 2007). We focus particularly on splitting of the CaPv 200_C diffraction line, because it shows the largest difference between the two structures. Octahedral rotation alone can result in a few different tetragonal structures, such as $I4/mcm$, $P4/mbm$, and $I4/mmm$. However, because differences are subtle in powder diffraction patterns among the three structures (see Fig. 1 in Shim *et al.* (2002)), we use $I4/mcm$ as a

proxy for the tetragonal crystal structure of CaPv induced by octahedral rotation.

The 200_C diffraction line of CaPv splits the most in both tetragonal diffraction patterns (Fig. 5.1). However, the intensities of tetragonal CaPv 200_C diffraction peaks differ depending on space groups. The lower angle split peak of the 200_C line has a smaller intensity in $I4/mcm$, while it has a higher intensity in the $P4/mmm$ structure. It is also important to note that the lower angle split line of 200_C exist at a similar diffraction angle as the original cubic 200 line for the octahedral rotation cases, while it is the higher angle split line for the octahedral distortion case ($P4/mmm$). The 110_C, 211_C, and 220_C lines also show splitting but with smaller degrees in both $I4/mcm$ and $P4/mmm$ structures.

During laser heating of the starting material, XRD patterns show formation of CaPv. We did not observe any splitting at T between 1700 and 2300 K (Fig. 5.2), supporting the stability of the cubic structure at high T (Kurashina *et al.*, 2004). After T-quench, we have observed clear peak splitting of the 200_C line in CaPv as shown in Fig. 5.2b at all pressures between 25 and 62 GPa at an X-ray wavelength of 0.4066 Å. With smaller wavelengths of X-ray, it was difficult to observe the splitting (such as 0.3344 Å). Instead, we observed the selective broadening of the 200_C diffraction line.

Although we observe peak splitting for the 200_C line, unlike the previous studies (Shim *et al.*, 2002), we found that the higher-angle diffraction line of the split 200_C line has a greater intensity throughout the pressure range at 300 K. As shown in (Figure 5.2), our new results obtained under a Ne pressure medium is more consistent the XRD patterns expected for tetragonal structures induced by octahedral rotation than octahedral distortion. In order to detect the 200_C line with a higher X-ray wavelength, Shim *et al.* (2002) used a slot-shaped DAC aperture. However, slot-shaped DAC aperture only allow for 10–20° portion of the Debye rings. In this study, we were able to measure full Debye rings by using conical aperture of DAC. Due to

the full coverage in this study, our diffraction intensities should be less affected by preferred orientation.

We performed Rietveld refinements on diffraction patterns measured at pressures between 28 and 62 GPa at 300 K after laser heating. We only choose diffraction patterns measured under the best resolution setup (Figure 5.3). These refinements were performed with two different crystal structures for CaPv: $I4/mcm$ (octahedral rotation Stixrude *et al.*, 1996a) and $P4/mmm$ (octahedral distortion Shim *et al.*, 2002). The atomic positions in the $I4/mcm$ structure are obtained from Caracas and Wentzcovitch (2006).

Through rotations of the SiO_6 octahedra in the (001) plane, the c_p axis (subscript "p" represents pseudo-cubic unit cell) becomes longer than the a_p axis in the $I4/mcm$ structure. However, depending on distortion in the SiO_6 octahedra, the c_p/a_p ratio can be smaller than 1 in the $P4/mmm$ space group (Shim *et al.*, 2002). The c_p/a_p of CaPv obtained from our Rietveld refinement is 1.0054±0.0005 without significant change with pressure (Fig. 5.4). Shim *et al.* (2002) reported $c_p/a_p = 0.993-0.996$. Through *ab initio* calculations, Stixrude *et al.* (2007) suggested an increase in c_p/a_p from 1.013 to 1.020 with an increase in pressure from zero to 140 GPa at 0 K. Because our pressure range is much smaller, such small increase over the larger pressure interval would be difficult to resolve from our data. Because the value from *ab initio* calculation is performed for 0 K, thermal effect could further decrease c_p/a_p. Stixrude *et al.* (2007) estimated that the value would decrease to 1.0094 at 25.2 GPa 300 K. Therefore, our new results are consistent with theoretical predictions on the crystal structure of Ca-Pv with octahedral rotation.

We fit the pressure–volume data at 300 K to the Vinet equation (Vinet *et al.*, 1989). For the Pt scales of Dewaele *et al.* (2004) or Holmes *et al.* (1989), we obtained isothermal bulk modulus (B_0) of 220(1) and 234(1) GPa, respectively (Figure 5.5). In

Table 5.1: Model Parameters for EOS of CaPv

CaPv	V_0 (Å^3)	B_0 (GPa)	B_0'	EOS[a]	Symmetry[b]	P scale[c]	Medium
Experimental studies							
This work	46.31(3)	220(1)	4[f]	V	Tet.	Pt-D	Ne
This work	46.37(3)	234(1)	4[f]	V	Tet.	Pt-H	Ne
Wang *et al.* (1996)	45.58 (4)	232(8)	4.8[f]	BM	Cub.	NaCl	NaCl
Shim *et al.* (2002)	45.58[f]	255(5)	4[f]	BM	Tet.	Pt-H	Ar
Shim *et al.* (2002)	45.58[f]	256(1)	4[f]	V	Tet.	Pt-H	Ar
Ricolleau *et al.* (2009)[e]	45.60[f]	244(1)	4[f]	BM	Tet.	Au-F	Ne
Noguchi *et al.* (2013)	45.80	225	4[f]	BM	Cub.	Pt-F	NaCl
Theoretical caculations							
Magyari-Köpe *et al.* (2002)	45.69	216	4.82	V	Orth.		
Jung and Oganov (2005)	46.89	219	4.08	BM	Tet.		
Chizmeshya *et al.* (1996)	45.62	227	4.29	BM	Cub.		
Akber-Knutson *et al.* (2002)	45.90	228	4.3	BM	Orth.		
Zhang *et al.* (2006)	45.58	242	4.18	BM	Cub.		
Caracas *et al.* (2005)[d]	44.537	249	4.09	BM	Tet.		
Stixrude *et al.* (2007)[d]	44.00	252	4.1	BM	Tet.		

[a] V and BM represent Vinet and third order Birch-Murnaghan equations, respectively

[b] Cub., Tet., and Orth. represent cubic, tetragonal, and orthorhombic structures, respectively

[c] Pt-D refers to Pt scale by Dewaele *et al.* (2004). Pt-H refers Pt scale by Holmes *et al.* (1989). Au-F and Pt-F refer to Au and Pt scales by Fei *et al.* (2007).

[d] Bulk modulus calculated at 0 K.

[e] They used pyrolitic composition as a starting material.

[f] These values were fixed during EOS fit.

the fitting, we fixed the pressure derivative of the isothermal bulk modulus (B_0') to 4.0, while we didn't fit the volume at 1 bar and 300 K (V_0), because CaPv is unstable at the conditions and therefore V_0 is unknown. Comparison with Shim *et al.* (2002), we found much smaller B_0 when we use the same pressure scale (Table 5.1). Considering different pressure medium in these two studies, it is likely that the improved stress conditions in this study yields a smaller B_0 (Klotz *et al.*, 2009). The differences between this study and Wang *et al.* (1996) are due to the fact that they only covered 1 to 10 GPa, where CaPv is metastable.

5.4 Discussion

In this study, we improve the stress conditions of experiments for CaPv by combining a soft pressure medium (Ne) and laser annealing. Under this condition, we obtained significantly lower bulk modulus of CaPv. Furthermore, our XRD indicates that the origin of distortion in CaPv from ideal cubic perovskite structure would be the SiO_6 octahedral rotation instead of distortion in the octahedra under quasi-hydrostatic stress conditions. In order to further understand the role of deviatoric stress, we performed an experiment without a pressure medium. In this experiment, the CaPv 200_C diffraction peaks were much broader and more asymmetrical than runs with Ne at high-T both during and after laser heating (Figure 5.6).

Thermal annealing is known to reduce deviatoric stress in the sample but not completely (Kavner and Duffy, 2001). Without a pressure medium, we observed a doublet for 200_C even at high T (1550 K) and 31.1 GPa. FWHM of CaPv 200_C peak without medium is 2.3 times greater than that in a Ne pressure medium at similar P–T (Fig. 5.6). This clearly shows that non-hydrostatic pressure would cause the broadening of the 200_C peak which could also have been misinterpreted as an equilibrated, distorted non-cubic structure.

The shear strength of a pressure medium is important for non-hydrostatic stress conditions in the sample chamber of a DAC. Magnesium oxide (MgO), which is used in Komabayashi *et al.* (2007) for CaPv, is not a hydrostatic medium, with a 10 GPa shear strength at pressures of 60–100 GPa (Duffy *et al.*, 1995).

The shear strength of Ar, which was used in Shim *et al.* (2002), is about 0.8 GPa at 65 GPa when the stress is not thermally annealed, while thermal annealing at 700 K reduces the stress to 0.56 GPa at 65 GPa (Marquardt *et al.*, 2013). Using Ne as a pressure medium, the values of pressure gradient from different ruby spheres are less

than 0.5 GPa at a pressure of 50 GPa without annealing (Klotz *et al.*, 2009). Although noble gas media in general support smaller deviatoric stresses, CaPv appears to be still sensitive to deviatoric stress in the media. This is perhaps because free energy differences among the candidate structures for CaPv are very small (Caracas *et al.*, 2005), and therefore metastable structure can appear easily even with small deviatoric stress in this phase.

We note that we found significantly lower bulk modulus in this study. It is likely the effects of reduced deviatoric stress. However, it is also possible that the higher bulk modulus in previous experiment could be because of different compressibilities of metastable crystal structures of CaPv, which further highlights the importance of hydrostaticity in high pressure determination of materials properties.

5.5 Geophysical Implications

We have calculated the density and bulk sound speed of CaPv as a single mineral phase and MORB at lower-mantle pressures along the geotherm by Brown and Shankland (1981b) using the Burnman toolkit (Cottaar *et al.*, 2014b) (Fig. 5.7). We used two different sets of compressibility parameters: this study and Shim *et al.* (2002). The thermodynamic parameters of CaPv are obtained from Noguchi *et al.* (2013). We also have conducted the calculation using the thermodynamic parameters of CaPv by Stixrude and Lithgow-Bertelloni (2011), but did not find any significant differences in the results. For the thermoelastic parameters of other minerals in MORB, such as bridgmanite, stishovite, and Ca-ferrite type phase, we combined datasets from existing studies (Lundin *et al.*, 2008; Catalli *et al.*, 2011; Stixrude and Lithgow-Bertelloni, 2011). Our calculation here assumes that the compressibility parameters do not change significantly between the tetragonal phase stable at lower T and the cubic phase stable at higher Ts. Noguchi *et al.* (2013) measured the compressibility

of cubic CaPv at T higher than 700 K.

Their projected bulk modulus to 1 bar and 300 K is 225 GPa, which agrees well with the value we obtained in this study under quasi-hydrostatic stress conditions, validating our assumption.

The new compressibility parameters from this study results in slightly lower and greater density of CaPv than PREM (Preliminary Reference Earth Model) at the shallower and deeper lower mantle, respectively. We found more significant changes by our new compressibility measurements in bulk sound speed profile (Fig. 5.7). Compared with Shim *et al.* (2002), the bulk sound speed of CaPv decreases by 3.6–5.4% throughout lower-mantle pressures, making it more similar to or slightly lower than that of PREM. Such a severe decrease would impact the bulk sound speed of Ca-rich mantle heterogeneities, such as MORB where CaPv represents ∼25 wt% (Hirose *et al.*, 2005b).

Our new results do not severely change the density profile of MORB within the estimated uncertainty and leave the density of MORB significantly higher than that of the lower mantle. Therefore, MORB remains negatively buoyant throughout the lower mantle. However, our new compressibility parameters decrease the bulk sound speed of MORB by 1–1.3% compared with Shim *et al.* (2002), making the bulk sound speed of MORB smaller than PREM by 1–2% throughout the lower mantle. The effect is particularly significant at depths between 700 and 2000 km. Therefore, MORB in the mid to lower mantle should contribute to slower bulk sound speed anomalies. MORB may have smaller shear velocities than PREM in the lower mantle (Kawai and Tsuchiya, 2015). Therefore, MORB will appear as low velocity anomalies in the lower mantle in bulk sound speed, P-wave speed, and S-wave speed seismic imaging.

Table 5.2: Lattice Parameters of CaPv Determined by Rietveld Refinements

Rietveld data	P (GPa)[a]	Structure	a ($Å^3$)	c ($Å^3$)
71013	28.547	$I4/mcm$	4.8896 (3)	6.9677 (8)
		$P4/mmm$	3.4690 (2)	3.4496 (4)
81021	28.853	$I4/mcm$	4.8941 (1)	6.9546 (4)
		$P4/mmm$	3.4685 (3)	3.4582 (5)
81043	30.651	$I4/mcm$	4.8714 (1)	6.9209 (4)
		$P4/mmm$	3.4546 (1)	3.4409 (2)
81030	32.077	$I4/mcm$	4.8805 (2)	6.9611 (8)
		$P4/mmm$	3.4610 (2)	3.4477 (4)
81057	39.79	$I4/mcm$	4.8282 (1)	6.8641 (4)
		$P4/mmm$	3.4253 (2)	3.4099 (3)
71050	41.53	$I4/mcm$	4.8351 (1)	6.8683 (3)
		$P4/mmm$	3.4297 (1)	3.4134 (2)
81066	47.301	$I4/mcm$	4.8070 (2)	6.8354 (3)
		$P4/mmm$	3.4119 (1)	3.3922 (3)
81074	53.816	$I4/mcm$	4.7870 (2)	6.8065 (4)
		$P4/mmm$	3.3978 (2)	3.3784 (3)
71088	62.669	$I4/mcm$	4.7535 (1)	6.7571 (3)
		$P4/mmm$	3.3737 (1)	3.3546(2)

The numbers in the parentheses are 2σ uncertainties. We only use 300 K data points. Pressure was calculated by EOS of Pt from (Dewaele *et al.*, 2004).

5.6 Conclusion

We have investigated the equation of state and the crystal structure of $CaSiO_3$ perovskite (CaPv) at 28–62 GPa and 300 K under quasi-hydrostatic stress conditions in a Ne pressure medium with laser annealing in a diamond-anvil cell (DAC) combined with synchrotron X-ray diffraction (XRD). We found that the bulk modulus of CaPv is significantly lower (220 GPa) than previous experiments which have been conducted under less hydrostatic stress conditions (250–260 GPa). We observed clear splitting of the CaPv 200 diffraction peaks. Rietveld refinements show significant improvement in fitting if starting model is a tetragonal perovskite-type structure with the SiO_6 octahedral rotation along the c axes, unlike previous experiments under less hydrostatic conditions, but consistent with first-principles studies. The higher bulk modulus reported in previous studies is likely due to deviatoric stress combined with formation of a metastable CaPv structure under non-hydrostatic stress conditions. We found that the lower bulk modulus of CaPv reduces the bulk sound speed of mid-oceanic ridge basalt (MORB) in the lower mantle, making it a candidate for low-velocity anomalies found in seismic studies in the region.

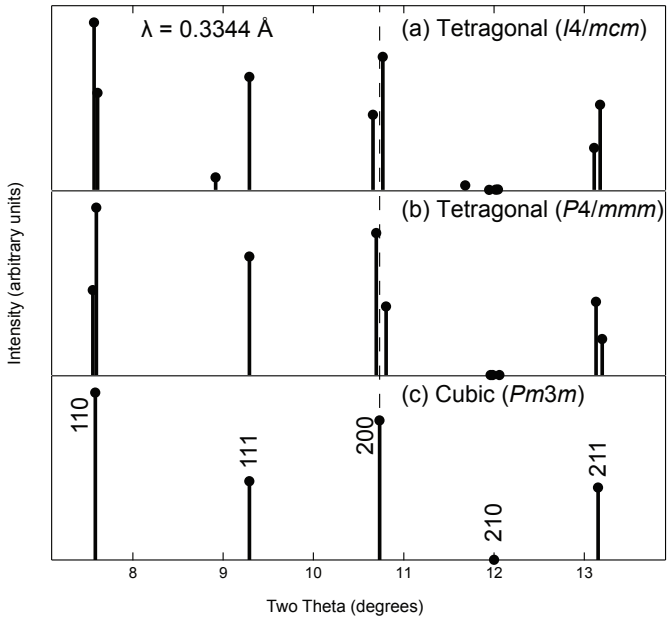

Figure 5.1: Calculated XRD Patterns of CaPv in Different Crystal Structures at 1 bar and 300 K,

We assume $V_0 = 45.58\,\text{Å}^3/\text{Z}$ (X-ray wavelength = 0.3344 Å): (a) cubic $Pm\bar{3}m$ (Caracas and Wentzcovitch, 2006). In (a), XRD peaks are indexed by cubic $Pm\bar{3}m$ space group. (b) tetragonal $P4/mmm$ (a = 3.5781 Å and c = 3.5601 Å) (Shim *et al.*, 2002) and (c) tetragonal $I4/mcm$ (a = 5.0426 Å and c = 7.1658 Å) (Caracas and Wentzcovitch, 2006) For the two tetragonal cases in (b) and (a), we assumed the same magnitude of distortion ($c_p/a_p = 0.995$ for (b) and $c_p/a_p = 1.005$ for (a). The thin vertical dashed line extended from the 200_C diffraction peak highlights the different angle shifts expected for the split lines in $I4/mcm$ and $P4/mmm$.

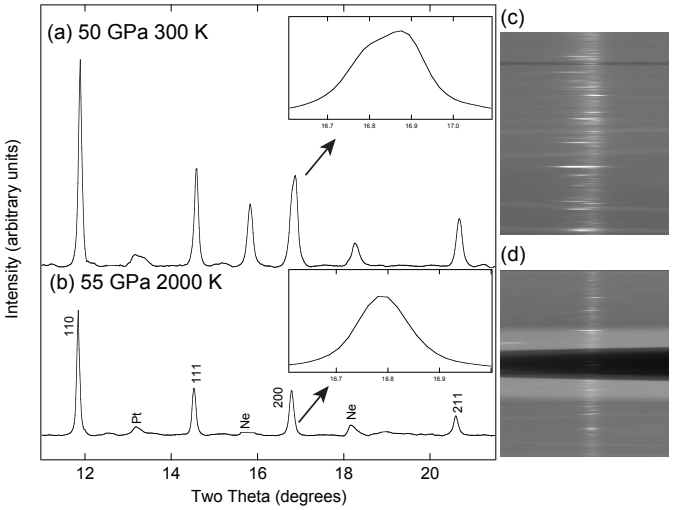

Figure 5.2: XRD Patterns of CaPv at 50–55 GPa and 300 K (a) and 2000 K (b). The samples include $CaSiO_3$ perovskite (CaPv), platinum (Pt, laser coupler) and neon (Ne, pressure medium). The peaks are indexed with cubic $Pm\bar{3}m$ space group. The inset images show the (a) splitting and (b) no-splitting of the 200_C diffraction peak at 300 K and 2000 K, respectively. The wavelength of the X-ray beam is 0.4959 Å. Unrolled projection of the 2D raw diffraction images of CaPv 200 peak are shown for T at (c) 300 K, and (d) 2000 K. In (d), the black image in the middle is from mirrors for laser heating at high temperature.

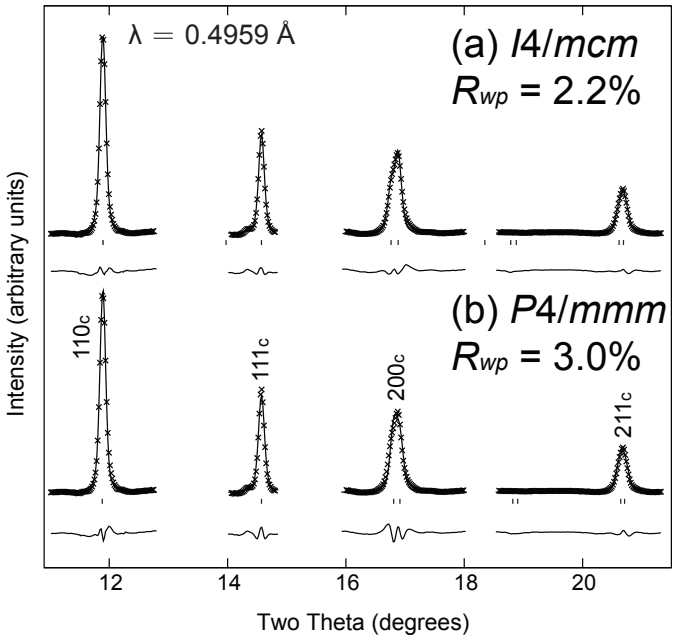

Figure 5.3: Rietveld Refinements of the XRD Pattern of CaPv at 53.8 GPa and 300 K with the $I4/mcm$ space group (a) and $P4/mmm$ space group (b). X-ray wavelength is 0.4959 Å. Crosses are observed intensities and the line behind crosses is the calculated diffraction patterns. Differences between observed and calculated intensities are plotted below. Bars in between represent calculated CaPv peak positions. We did not include the angular ranges for the Pt and Ne peaks in the Rietveld refinements.

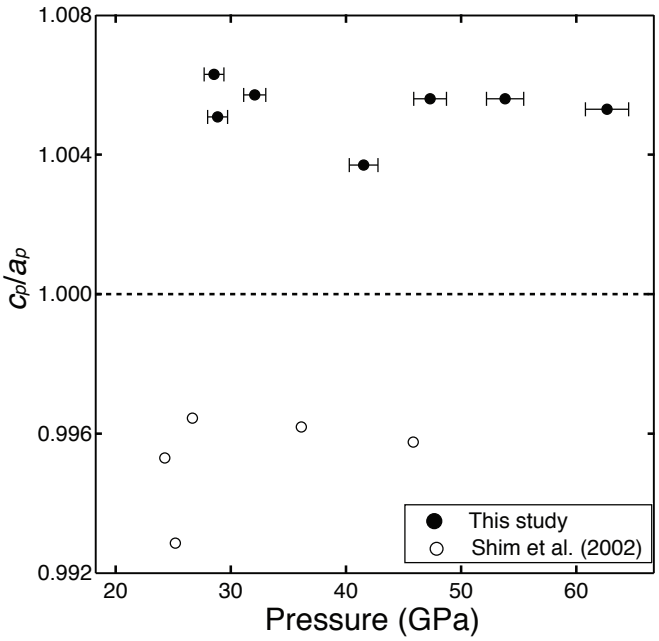

Figure 5.4: Axial Ratios (c_p/a_p) of Tetragonal CaPv Unit Cell From Shim *et al.* (2002)

(open circles) and this study (close circles). Error bars represent $1\,\sigma$ uncertainties.

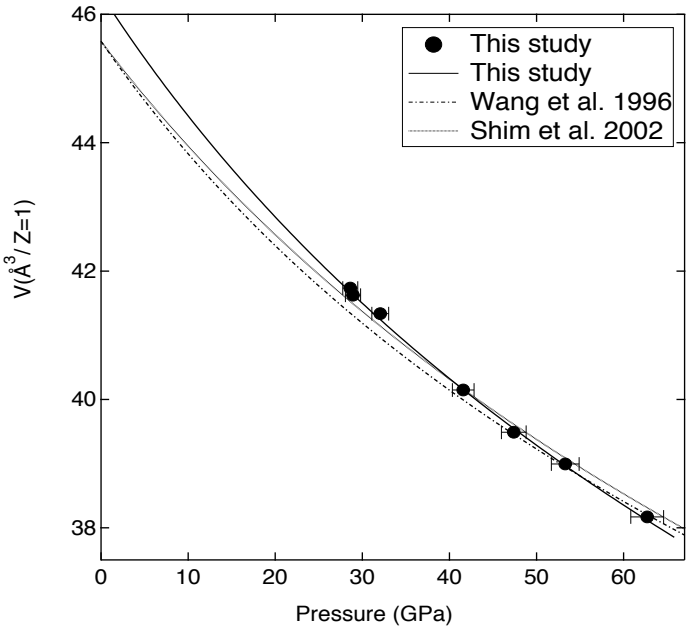

Figure 5.5: Volumes of Pseudo Cubic Unit Cell of CaPv Measured at High Pressure (circles).

Vinet EOS parameters for tetragonal CaPv in this plot: $B_0 = 220\,\mathrm{GPa}$, $B_0' = 4.0$, $V_0 = 46.17\,\mathrm{\AA}^3/\mathrm{Z}$. Pressure was calculated from Dewaele *et al.* (2004). We also plot EOS from Shim *et al.* (2002) and Wang *et al.* (1996) for comparison. Error bars for pressure represent 1σ uncertainties. Error bars for volume is smaller than size of the marker.

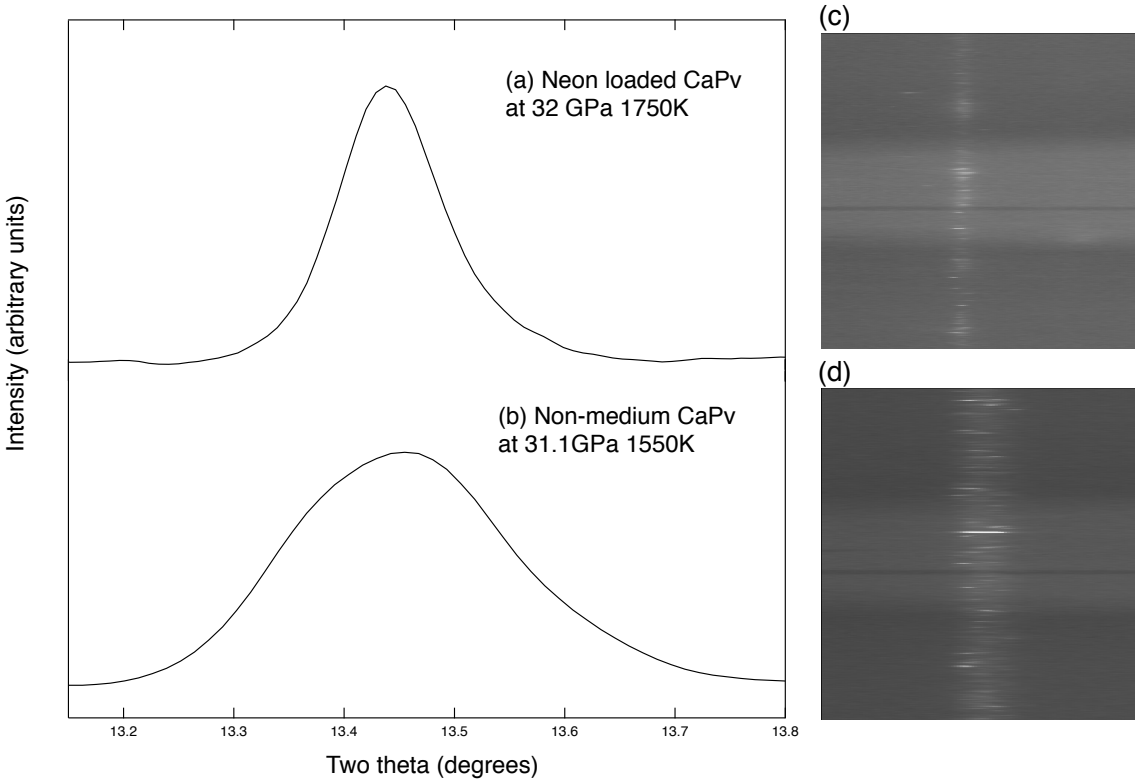

Figure 5.6: Cubic 200 Diffraction Peaks of CaPv Measured With Ne or Without Pressure Mediums

With an X-ray wavelength of 0..3344 Å and detector distance of 196.56 mm. (a) at high T, symmetrical cubic CaPv 200 diffraction peak was observed using Ne as a pressure medium. (b) broader and asymmetrical CaPv 200 diffraction peak was shown without pressure medium. Unrolled projection of 2D raw diffraction image of CaPv 200 peak (c) with a Ne pressure medium and (d) without a pressure medium.

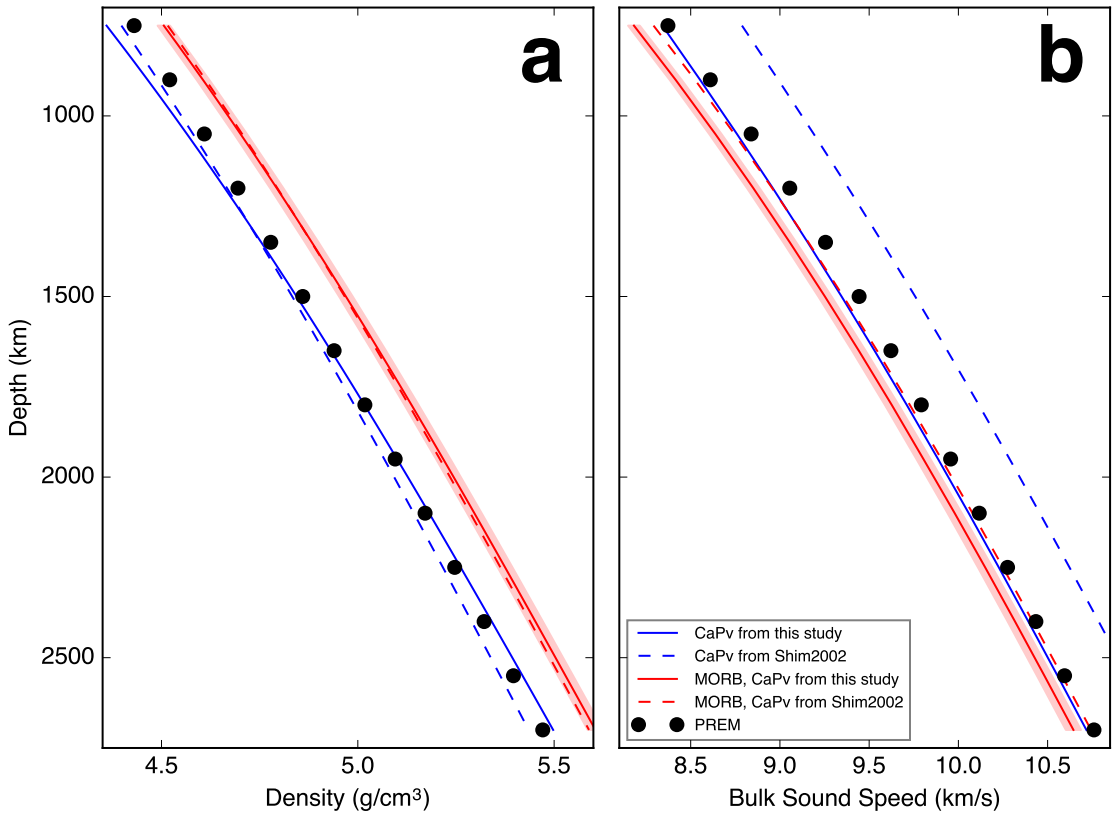

Figure 5.7: One-dimensional Profiles of (a) Density and (b) Bulk Sound Speed. The blue solid and dashed curves are the profiles of pure CaPv calculated using EOS from this study and Shim *et al.* (2002), respectively. The red solid and dashed curves are the profiles of MORB calculated using the EOS of CaPv from this study and Shim *et al.* (2002), respectively. The solid circles represent values from PREM (Dziewonski and Anderson, 1981).

Chapter 6

POSSIBLE H_2O STORAGE IN THE CRYSTAL STRUCTURE OF $CASIO_3$ PEROVSKITE

6.1 Introduction

H_2O can play an important role in controlling the viscosity and melting temperature of minerals and thus greatly affect mantle convection (Bercovici and Karato, 2003). Some amount of water could be transported to the mantle by subducting slabs (van Keken *et al.*, 2011). Recently, diamond with hydrous ringwoodite as inclusion was found in nature. The ringwoodite contains about 1.4 wt% water (Pearson *et al.*, 2014). Another study documented diamond containing free ice VII as inclusion at the upper lower mantle pressure up to 25 GPa (Tschauner *et al.*, 2018), indicating that the lower mantle at least up to 25 GPa might not be completely dry. Alternatively, this diamond might come from slabs dehydration when it penetrated into the lower mantle, which might also mean that the lower mantle is mostly dry (Schmandt *et al.*, 2014; Tschauner *et al.*, 2018).

The capabilities of mantle minerals to store water are the keys to understand the possible existence and concentration of hydrogen in deep mantle. This can be done through high pressure and high temperature experiments. Oxygen is the major anion species in the mantle. I will not distinguish water, H_2O, H or hydrogen in this chapter. Hydrous minerals are candidate for water storage in the mantle (Ohtani, 2015). Several hydrous phases have been discovered from experiments, for example phase egg (Eggleton and Ringwood, 1978), δ–AlOOH (Sano *et al.*, 2008), phase D (Frost and Fei, 1998), Phase H (Nishi *et al.*, 2014) and FeOOH (Nishi *et al.*, 2017).

However, most of them would dehydrate at mantle geotherm related temperatures (Sano *et al.*, 2008; Nishi *et al.*, 2014). Suducting slabs are much cooler and thus these hydrous phases might be able to carry some amount of water to the deep interior (van Keken *et al.*, 2011).

The nominally anhydrous minerals (NAMs) are also important water carriers in the mantle. Some NAMs have capabilities to hold 20 to 30000 ppm water. The upper mantle minerals have relatively low water storage capabilities compared with the transition zone minerals. For example, olivine and garnet in the upper mantle can hold about 200 ppm water (Smyth *et al.*, 2006), while wadlesyite and ringwoodite in the mantle transition zone could contain up to 3 wt% water (Ye *et al.*, 2010; Inoue *et al.*, 1995). The possible water content in the lower mantle has not been well studied, despite the fact that the lower mantle composes about 70 wt% volume of the mantle. The most dominant mineral bridgmanite could only contain less than 200 ppm water (Bolfan-Casanova *et al.*, 2000), and ferroperoclase might contain no more than 20 ppm water (Bolfan-Casanova *et al.*, 2003). Thus, it has been believed that the lower mantle is relative dry (Bolfan-Casanova *et al.*, 2003; Panero *et al.*, 2015). However, to our knowledge, $CaSiO_3$ pervoskite (CaPv) as the third most abundant phase in the lower mantle (Kesson *et al.*, 1998a) had not been studied in terms of water solubility. Thus, studying the possible water solubility in CaPv is important to constrain the water distribution in the deep interior.

CaPv is not quenchable to 1 bar, which prevents high precision measurement for the recovered sample (Chen *et al.*, 2018). The‘measurements of water for unquenchable phases remain technically challenging. Thus, in-situ high pressure measurement is needed to study the possible water storage capabilities in unquenchable phases.

Infrared spectroscopy is sensitive the O–H vibration mode from trace amount of structurally incorporated water. From infrared spectra, the water content in a

mineral can be estimated using the existing equations, for example, Paterson's method (Paterson, 1982). The unit-cell volumes of crystalline materials are sensitive to the content of water which tends to expand the unit cell (Spektor *et al.*, 2011; Panero *et al.*, 2015; Spektor *et al.*, 2016b). The change in the unit-cell volume at different pressures would also impact the compressibility of the minerals (Panero *et al.*, 2015). Thus, in-situ infrared spectroscopy and X-ray diffraction can be used to constrain the possible water solubility in the unquenchable phases, because quenchable phases would still show similar behaviour.

CaPv adopt a cubic structure at high pressure and high temperature condition (Shim *et al.*, 2002). The tetragonal CaPv was found to be stable at low temperature and high pressure condition which also agrees with first principle calculations (Shim *et al.*, 2002; Stixrude *et al.*, 1996b). The rotation of the SiO_6 octahedra resulted in the distortion of CaPv from the cubic structure to the tetragonal structure (Stixrude *et al.*, 1996b; Shim *et al.*, 2002; Chen *et al.*, 2018). Hydrogen is known to influence crystal structure or phase transition pressure (Lakshtanov *et al.*, 2007b). Thus, it is intriguing to test whether the incorporation of hydrogen into the CaPv would affect the crystal structure and phase transition of CaPv.

6.2 Experimental Methods

$CaSiO_3$ glass was made using the laser levitation method (Tangeman *et al.*, 2001). Xonotlite was synthesized from CaO, SiO_2 (Alfa-Aesar) and water at 1 GPa and 500 °C using piston cylinder at the Depth of the Earth lab in Arizona State University. We used 2010F (JEOL) electron microbe to confirm the composition of suolunite to be pure $CaSiO_3$. Synchrotron X-ray diffraction was also used to study the crystal structure of suolunite and xonitlite, which are found to be in good agreement with the reported diffraction patterns (Ma *et al.*, 1999; Shaw *et al.*, 2000). $CaSiO_3$ glass,

suolunite or xonitlute were mixed with 10 wt% Pt (internal pressure standard (Ye *et al.*, 2017) and laser coupler) and then pressed to a foil. The foil was loaded into the Re gasket hole in DAC. Several spacers less than 10 μm from pure sample were placed below and above the sample foil to form a layer of Ne between sample and diamonds for thermal insulation. We loaded Ne as a pressure medium using the the gas-loading system at the GeoSoilEnviroConsortium for Advanced Radiation Sources (GSECARS) sector (Rivers *et al.*, 2008). For some runs, pure water was used as a pressure medium. Starting materials are listed in Table 6.1.

Table 6.1: Experimental Run Conditions.

SM: starting materials, Suo: Suolunite, Xon: Xonotlite, Glass: $CaSiO_3$ glass. "n/a" means not available here. T: Tetragonal, C: Cubic, Medium: Pressure Medium and P: Pressure.

Run	SM	product	Structure	Medium	P (GPa)	T (K)	water content (wt%)
s320	Suo	CaPv	T	water	30	1700	n/a
s111	Suo	CaPv	T	Ar	19	1400	0.5–1
s110	Suo	CaPv	T	Ne	60	1300–2100	n/a
s431	Suo	CaPv	T	Ne	45	1500–2200	n/a
s332	Suo	CaPv	T	Ne	120	2300	n/a
s411	Suo	CaPv	T	Ne	60	2000–2300	n/a
x231	Xon	CaPv	C	Ne	115	2000–2600	n/a
x310	Xon	CaPv	C	Ne	31	1300–1700	n/a
g211	Glass	CaPv	T	water	30	1400	n/a
g320	Glass	CaPv	T	water	60	1400–1600	n/a
al211	Al-Glass	CaPv + AlOOH	T	water	60	1400	n

We measured XRD patterns in the laser heated DACs at beamline 13ID-D in the GSECARS sector (Prakapenka *et al.*, 2008b) and beamline 16ID-B in the High Pressure Collaborative Access Team (HPCAT) sector (Meng *et al.*, 2006) at the Advanced

Photon Source. Monochromatic X-ray beams with beam sizes of 3×4 and $5\times6\,\mu m^2$ at GSECARS and HPCAT, respectively, were focused on the sample and the diffraction patterns were collected using a Mar-CCD detector.

Two near-infrared laser beams ($\sim$1 μm wavelength) were focused on sample through two opposite sides of DAC with a hot spot size of 20–25 μm^2. The laser beams were aligned coaxially with the X-ray beam. We found that the detection of the subtle peak splitting in a quasi-hydrostatic medium is very challenging. It requires a high resolution setup with an X-ray energy of 25 keV. The use of the low energy limits the measurable d-spacing range to 1.557 Å, but enabled us to detect the subtle peak splittings from CaPv. With smaller X-ray wavelengths (such as 0.3344 Å), it was difficult to observe the splitting. Instead, we observed the selective broadening of the lines indicative of splitting below the resolution of the peaks. Temperatures were calculated by fitting thermal radiation spectra to the Planck equation from both sides of the sample after subtracting backgrounds.

In a typical experiment, we compressed the sample to target pressures at 300 K, and then conducted heating. We increased the laser power quickly to reach the target T (1400–2300 K) in less than 1 minute to avoid formation of metastable phases. CaPv forms within 1 minutes upon heating above 1400 K and diffraction patterns of CaPv remain essentially the same during heating. The room-T diffraction was then acquired on the heated spot at each target pressure. We also conducted separate CO_2 heating experiments. For the separate CO_2 heating experiments which we did not use any laser coupler to synthesize a single CaPv phase without laser heating coupler, we cryogenically loaded an Ar medium in a DAC. A ruby chip was loaded at the edge of the sample chamber for pressure measurements but away from the sample foil in order to avoid any chemical reaction. We compressed the samples with type-II diamond anvils and focused a CO_2 laser beam on the sample foil in the DAC. Single-

sided heating was conducted at 1200–2420 K using a laser heating system at Arizona State Unviersity. The size of the laser heating spot was ∼50 μm. Temperatures were calculated by fitting the measured thermal radiation spectra to the Planck equation from one side of the sample after the subtracting backgrounds from optics in the system. Pressure was measured from ruby fluorescence line shift or the first-order Raman mode from the tips of the diamond anvils (Mao *et al.*, 1978; Akahama and Kawamura, 2006).

We used the Dioptas package (Prescher and Prakapenka, 2015) to integrate the diffraction images to 1D patterns. We performed peak fitting using a pseudo-Voigt profile shape function (Shim, 2017). The data obtained from the GSECARS and HPCAT beamlines agreed well with each other.

All high-pressure synchrotron infrared spectra in this study were collected at the beamline 1.4 of the Advanced Light Source using a Nicolet Magna 760 FTIR spectrometer with a custom microscope. A HgCdTe detector was used for data collection. In a typical experiment, pure suolunite together with 5 μm ruby grains were loaded into sample chamber. We used CO_2 laser heating for infrared spectra measurement. Ar was loaded cryogenically as a pressure medium. Sample was heated with a CO_2 laser with 50 μm spot size, custom built at Arizona State University. The resolution of FTIR spectrometer is 4 cm^{-1}. Typically spectra presented here contain 256 scans. Ruby fluoresce in the sample chamber was used as the pressure calibration (Mao *et al.*, 1978). Pseudo-Voigt profile shape function from Newville *et al.* (2015) was used to do curve fitting the position and width of infrared peaks.

Paterson method (Paterson, 1982) was used to calculated water content from the infrared spectra.

$$C_{H_2O} = \frac{X_i}{150\zeta} \int \frac{k(v)}{3780 - v} dv, \tag{6.1}$$

Where C_{H_2O} is water content in ppm (part per million). X_i is the density factor for

CaPv, which we used 2127. $X_i = 10^6 \times (18/2d)$, where d is the mineral density (in g/l) (Paterson, 1982). We used 1 bar unit cell volume to calculate the density for CaPv (Shim *et al.*, 2002). ζ is the crystal orientation factor and in this case we used 1/3, assuming that CaPv crystals are randomly oriented in the DAC. $k(v)$ is absorption coefficient for infrared in cm^{-1}. v is the absorption wavenumber.

6.3 Result and Discussion

CaPv synthesized from dry condition show the phase transition from cubic to tetragonal during temperature quench in our experiments. In our experiments, CaPv adopted a cubic structure at high temperature while the quenched pattern show tetragonal structure (Chen *et al.*, 2018; Shim *et al.*, 2002; Stixrude *et al.*, 1996b). When we used xonotlite with 2.5 wt% water as a staring material, CaPv showed similar behaviour as the experiments using dry glass (Figure 6.1c and d) (Chen *et al.*, 2018; Shim *et al.*, 2002; Stixrude *et al.*, 1996b). We observed a doublet instead a singlet after temperature quench at high pressure, indicating a cubic to tetragonal phase transition during temperature quench (Chen *et al.*, 2018; Shim *et al.*, 2002; Stixrude *et al.*, 1996b).

Using suolunite with 13 wt% water as a starting material, we observed distorted tetragonal structure of CaPv after temperature quench. At high temperature up to 1800 K, the diffraction patterns showed clear peak splitting of the 200 peak, suggesting the stability of the tetragonal structure at high temperatures. In the case of suolunite, water might distorted crystal structure of CaPv at high temperature casued by some amount of water incorporated into CaPv. To further explore the effect of water on the crystal structure of CaPv, we load $CaSiO_3$ glass with water. We still observed the peak splitting at 1400–1600 K and 30–60 GPa in this water saturated conditions.

The reason that xonotlite does not showing any detectable distortion could be

that there were not enough water in the system or the distortion in CaPv by water is related to water content in starting material. Thus, it is likely that the distortion of CaPv from water is small in the experiment with xonotlite as a starting materials. It is also possible that the small amount of water could not distort the structure. Xonotlite contains 2.5 wt% water, while suolunite contains more than 13 wt% water (Ma *et al.*, 1999; Shaw *et al.*, 2000).

For CaPv glass with water as a medium, the synthesized CaPv is under water saturated condition. The distortion of CaPv crystal structure were confirmed at high temperature in suolunite and water saturated experiment. It can be concluded that water affects the crystal structure of CaPv while it is still uncertain whether the possible cubic structure of CaPv from xonoilite starting material is related to the resolution of X-ray or the real cubic structure. From the water content measurement, we believe that the reason might be the resolution of X-ray, since even 2.5 wt% water is likely to be more than the maximum water solubility in CaPv which we will constrain from infrared spectra later.

The bulk moduli of water bearing minerals tend to be smaller than the dry counterparts (Panero *et al.*, 2015; Smyth *et al.*, 2003). We fitted the bulk modulus of CaPv synthesized from experiments with suolunite in a neon medium. We measured the unit-cell volumes of CaPv together with volumes of Pt and Neon. Pressure was calculated from equation of state (EOS) of Pt (Ye *et al.*, 2017). We fit the EOS of CaPv using the Birch–Murnaghan equation. The 1 bar volume of CaPv is fixed to 45.58 $Å^3$ during least square fitting, which is the unit cell volume of anhydrous CaPv projected to 1 bar (Shim *et al.*, 2002). We fixed the pressure derivative to 4.0 during fitting.

The bulk modulus is 231(2) GPa in Figure 6.2, which is smaller than reported value of dry CaPv, 255(5) GPa (Shim *et al.*, 2002). It is important to note that

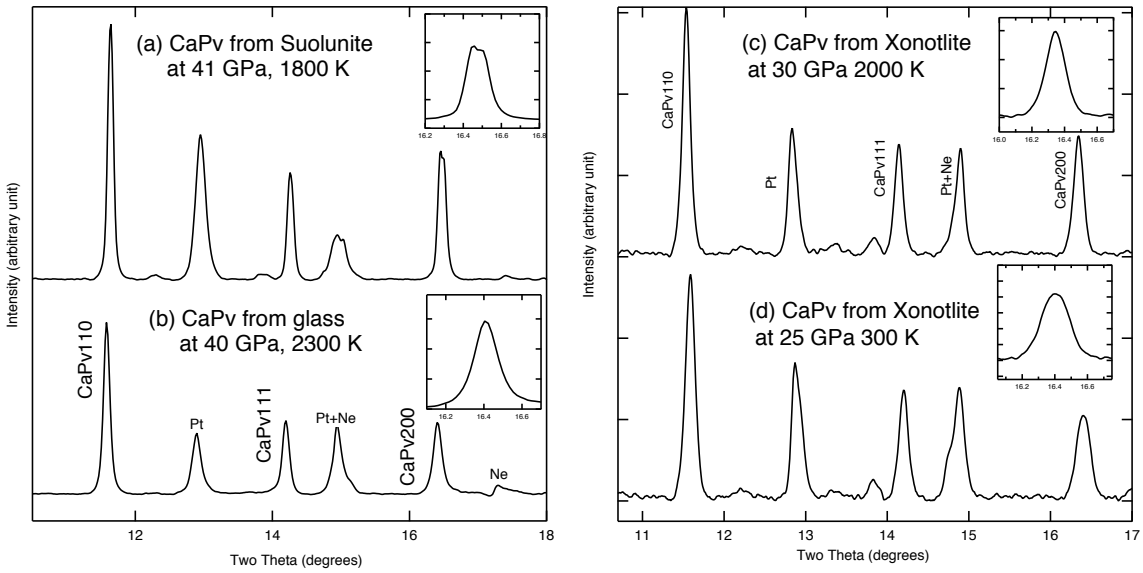

Figure 6.1: X-ray Diffraction Patterns of CaPv at High pressures and Temperatures. (a) CaPv at 40 GPa and 1800 K synthesized from suolunite, (b) CaPv at 40 GPa and 2300 K synthesized from $CaSiO_3$ glass, (c) CaPv synthesized from xonitlite at 30 GPa and 2000 K, (d) temperature quench pattern of CaPv from (c). The diffraction lines include $CaSiO_3$ perovskite (CaPv), platinum (Pt, laser coupler) and neon (Ne, pressure medium). The peaks are indexed with cubic $Pm\bar{3}m$ space group. The insets showed the 200_{pc} diffraction peak. The wavelength of the X-ray beam is 0.4959 Å.

the unit cell volume of hydrated crystals could be bigger than the dry counterpart if water is incorporated (Spektor *et al.*, 2011; Smyth *et al.*, 2006). However, we could not measure the unit cell volumes of CaPv at 1 bar due to the fact that it is not recoverable at 1 bar. And, the 1 bar volume is supposed to be higher since the incorporation of hydrogen such as hydrous stishovite (Spektor *et al.*, 2011). This would further decrease the bulk modulus of CaPv when we use a bigger unit cell volume as the 1 bar reference point. We also conducted least square fitting of BirchMurnaghan

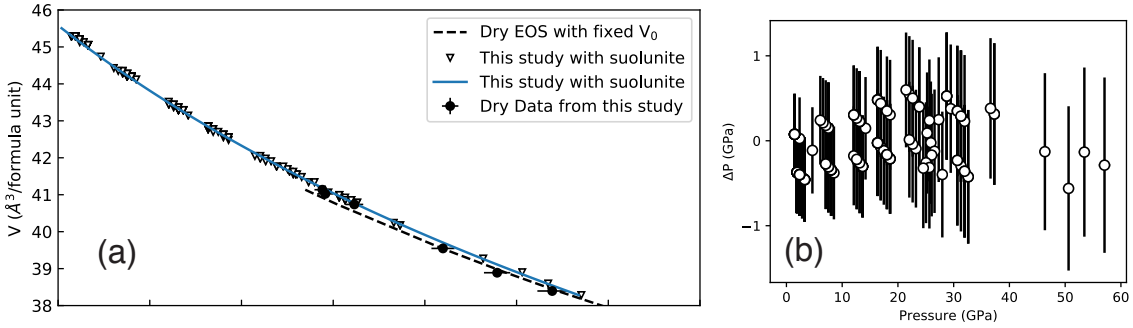

Figure 6.2: Equation of State for $CaSiO_3$ Synthesized From Suolunite. Bulk modulus K_0 is 231 GPa from the fitting of data. The bulk modulus from dry CaPv used in Chen *et al.* (2018) were included in a. Pressure derivative was set to 4.0 in order to compare bulk modulus with other studies (Shim *et al.*, 2002).

equation of state for hydrous CaPv without constraining the 1 bar unit cell volume. The fitting result gave the 1 bar unit cell volume to be 45.97(5) $Å^3$ and the bulk modulus was 208 GPa when the pressure deritive was fixed to 4.0. The higher 1 bar unit cell volume of hydrous CaPv (45.97 $Å^3$) compared the dry counterpart (45.58 $Å^3$) is caused by hydrogen incorporated into the crystal structure(Spektor *et al.*, 2016b). It is extremely diffcult to constrain the hydrogen content in the CaPv by comparing the unit cell volumes. Fomer studies attribute one hydrogen atom to have an effect of expanding 2.0 $Å^3$ for the crystal structure(Hu *et al.*, 2017). Here we found that the chemical system $CaSiO_3$ might contain 0.1 molar water ie CaSiO3 $0.1H_2O$ which equal to 1.5 wt% water. The bulk modulus with the new unit cell volume is 47 GPa lower than the dry CaPv (255 GPa), implying the possible hydrogen storage in the system similar to the case for hydrous stishovite (Nisr *et al.*, 2017a).

The possible storage of hydrogen in CaPv could be related to the silicon vacancies.

Spektor *et al.* (2011) had shown that the mechanism which four hydrogen substitute one Si might be related to the hydrogen storage in stishovite ($4\ H^+ = Si^{4+}$). For the CaPv, we assume a similar mechanism might be related to the hydrogen storage, which the 12 fold coordinated calcium sites in CaPv might be too big for two hydrogen atoms ($2\ H^+ = Ca^{2+}$). Further density functional theory calculations would be needed to clarify the mechanism for the distortion.

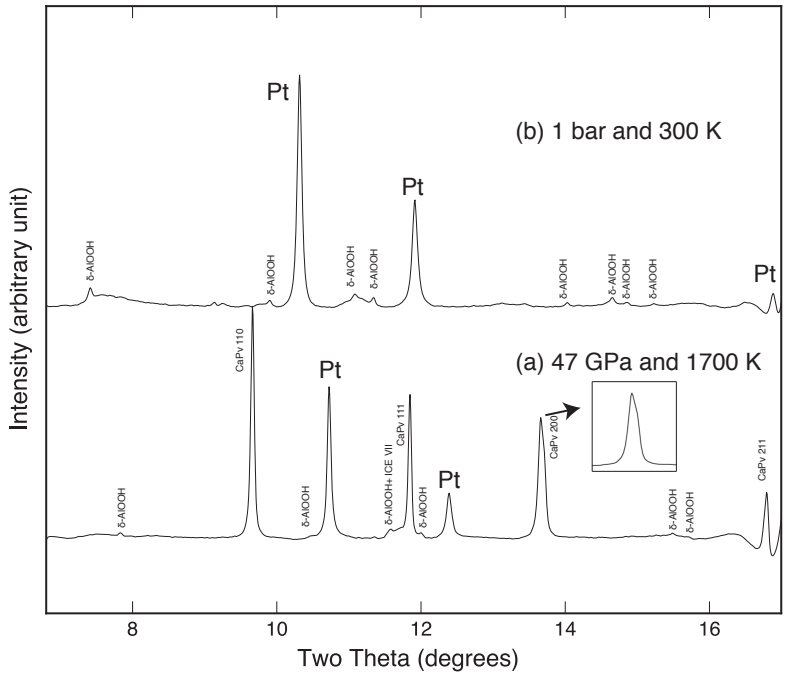

Figure 6.3: X-ray Diffraction Patterns of CaPv With δ–AlOOH at 47 GPa 1700 K Synthesized From Aluminum Bearing $CaSiO_3$ Glass

(a) and quenched products (b). The samples include $CaSiO_3$ perovskite (CaPv), platinum (Pt, laser coupler) and ice VII (water as a pressure medium). The peaks are indexed with cubic $Pm\bar{3}m$ space group. The inset image shows the CaPv 200 peak splitting. The unit cell volumes for δ–AlOOH is 56.408 $Å^3$ at 1 bar. The wavelength of the X-ray beam is 0.4066 Å.

Aluminum is potentially an important chemical component to consider for the deep water storage (Ohira *et al.*, 2014; Pamato *et al.*, 2015). In particular, aluminum bearing phase D greatly expand its temperature stability fields (Pamato *et al.*, 2015). Aluminum also expands the pressure stability fields of Phase H (Nishi *et al.*, 2014; Ohira *et al.*, 2014). In order to study the effect of aluminum on water storage capabilities of CaPv, 5 mol% alumina (Al_2O_3) was added before the synthesis of another the $CaSiO_3$ glass as a starting material. We used water as a pressure medium for the aluminum bearing $CaSiO_3$ glass sample. 'During experiments at high pressure and high temperatures, we saw the formation of δ–AlOOH (Sano *et al.*, 2008) together with CaPv at 47 GPa and 1700 K in Figure 6.3 within 10 mins of heating. CaPv has the capabilities to accommodate aluminum into the structure up to 10 wt% (Gréaux *et al.*, 2011). Surprisingly, the aluminum did not form a solid solution with CaPv, rather it grew its own phase δ–AlOOH with a presence of H_2O. The existence of water changed how major elements aluminum behavior in the CaPv systems, in which the δ–AlOOH is favored rather than forming a solid solution with CaPv in the system. The formation of δ–AlOOH should be more energetically favorable than the formation of Al bearing CaPv for the CaO–Al_2O_3–SiO_2–H_2O system. This observation also indicated that the $Al^{3+} + H^{+} = Si^{4+}$ mechanism is unlikely favorable in the CaPv system similar to bridgmanite (Ohira *et al.*, 2014).

In phase egg, one aluminum and one hydrogen replace one silicon atoms which satisfy the charge balance and the atomic size (Eggleton and Ringwood, 1978). This mechanism was found in the lower mantle chemical systems, which stishovite were found to form a possible solid solution with δ–AlOOH (Panero and Caracas, 2017). However, for CaPv, Si vacancies might be more likely to exist for CaPv to accommodate water into the structure. It is remain to be explored for bridgmanite even though the possible water storage content is low (Panero *et al.*, 2015).

To estimate water content in CaPv, we performed CO_2 laser heating on the CaPv synthesized from the suolunite sample at 19 GPa, 1400 K. We used Ar as a pressure medium. We did not use any platinum metal to make a pure CaPv sample at high pressure. After confirming the CaPv with X-ray diffraction at 300 K after laser heating, we measured the infrared spectra of CaPv in-situ at 19 GPa. We found an intense broad band at a wavenumber range of 3100–3600 cm^{-1} from the heated area shown in Figure 6.4a. For the broad O-H vibration feature at high pressure, we cound not constrain whether it is from one single O-H bonding environment or several different O-H bonding contribute to the feature.

The existence of hydrogen bonding could make the O-H bonding at the wavenumber around 3400 cm^{-1} as a broad feature (Paterson, 1982). The shift to higher frequency of the O-H bonding had been observed in high pressure ice during decompression (Goncharov *et al.*, 1996). Hydrogen symmetrization is likely the casue for the frequency decrease during decompression with other infrared active modes (Goncharov *et al.*, 1996). The symmetric O–H bonding would have a centered hydrogen in between two oxygens. The possible transition from symmetric to asymmetric H-O-H could be responsible for the strengthening O-H bonding during decompression, which we observe the similar trend in water bearing CaPv samples. Thus the wavenumber shifts to the higher frequency during decompression as shown in Figure6.4a and b. The trend of shift in the wavenumber would change before and after hydrogen symmetrization. When hydrogen is symmetrized at higher pressure, the trend for O-H bonding will be reversed that is shift to higher frequency during compression after hydrogen symmetrization. According to study of hydrogen symmetrization with ice, the reverse trend would likely happen above 60 GPa based on the oxygen–oxygen distance for hydrogen bonding (Goncharov *et al.*, 1996).

We note that during laser heating some amounts of water could be released from

the sample to the surrounding pressure medium when the maximum solubility of water in CaPv were reached. Thus the ice released and then condensed after laser heating might also contribute to the IR band we observed. We also plotted the fitted position of the infrared band from our experiments together with ice infrared from other studies in Figure 6.4b (Goncharov *et al.*, 1996). At high pressure, OH mode from CaPv behaves very differently from pure H_2O in terms of the location of the O-H band. However, when we approach to 1 bar, the band position from the position of the O-H band in CaPv merged to the band position of ice. CaPv transforms into a glass state at about 1 GPa. It can be anticipated to have infrared peaks of water after CaPv amorphized at lower pressures less than 1 GPa. We saw the infrared band of the recovered sample to be at the same band position as the room pressure water in Figure 6.4b. Thus, the high pressure infrared spectra should be contributed from CaPv but some amount of ice may also contribute to the O–H band.

We attempted to calculated the water content from high pressure infrared spectra using the Paterson method (Paterson, 1982). As we will note later, this value can only be viewed as the upper bound for water in CaPv that is combined with infrared spectra from ice in the system because the OH intensity may have been contributed from both CaPv and ice. We calculated the water content in CaPv to be about 0.5–1 wt% using the Paterson's method (Paterson, 1982). Paterson's method used room temperature and pressure infrared spectra of minerals to calculate water conent in an mineral with unknown water solubility (Paterson, 1982). We note that compression decreases high pressure decrease the infrared OH band frequench to a lower value in the case for CaPv from 3350 at 1 bar to 2950 cm^{-1} at 19 GPa. Thus the water content could be different if high pressure infrared band was calibrated using a room pressure infrared spectra as a standard method. However it is difficult to calibrate the infrared spectra at high pressure which we will discuss later including the factors

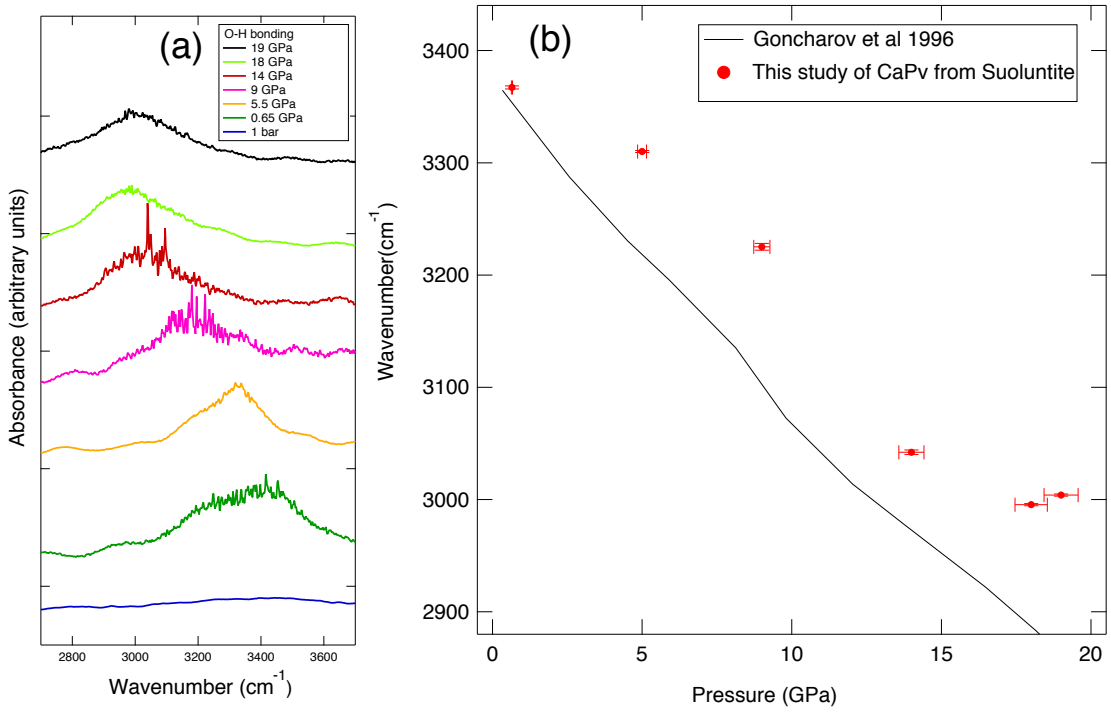

Figure 6.4: Infrared Spectra of CaPv Synthesized from Suolunite at 19 GPa and 1700 K, Which O-H mode Was Plotted.

Infrared spectra were taken during decompression (a). Comparison of the O-H mode from the infrared spectra from (a) and water infrared from Goncharov *et al.* (1996) (b).

that could influence the water content calculation of infrared spectra other than the shift of the wavenumber.

We assume a thickness of 10–20 microns for the sample at both high pressure and recovered sample. A smaller thickness might overestimate the water content from Paterson equation (Paterson, 1982). After pressure quench, the sample foil was about 12 micron and it was 20 micron before loading. The thickness measurement would affect the water content from CaPv by a factor of 2 when we assume the thickness is between 10 and 20 microns. For the water content measurement from

infrared spectra, the sample thickness, sample environment with possible ice and the limitation of Paterson equation would all contribute to the uncertainties of the water content from CaPv. The water content in CaPv was estimated to be between 0.5–1 wt% which is likely to overestimate the possible storage content in CaPv. However, it is impossible to qualitatively constrain the possible overestimate or underestimate of the water content in CaPv. If the Paterson's equation can be applied to higher pressure measurements and the thickness is can be measured precisely, the possible water storage in CaPv would be inferred from the infrared signal at high pressure. After subtracting of the O-H virbration signal of the possible ice from the total infrared O–H band, we would indeed derive the correct water content for CaPv. The O-H vibration signal from ice had several infrared bands that are impossible distinguish due to hydrogen bonding and the possible O-H bonding in CaPv also might have O-H bonding environment that are overlapping with high pressure ice. Thus, the results here might be served as an upper bond for water concentrations in CaPv.

6.4 Implication

Bridgmanite and ferropericlase contain less than 200 ppm water at the lower-mantle pressure and temperature conditions (Panero *et al.*, 2015; Bolfan-Casanova *et al.*, 2002, 2003) Compared with bridgmanite and ferropericlase, CaPv with possible 0.15–1 wt% water is so far the most water rich component among the NAMs in the lower mantle. And the lower mantle should not to be completely dry if the water content in CaPv is considered (Panero *et al.*, 2015). Few ppm of water would greatly decrease the rock viscosity and enhance the mantle convection (Karato, 1990; Richard *et al.*, 2002).

The aluminum partitioning behaviour in CaPv is also important to understand

the mineralogy of the lower mantle, which we found that the partitioning behavior of aluminum is sensitive to water in the lower mantle. Both in bridgamnite and CaPv, aluminum is not favored to incorporate into the pervoskite crystal structure when water is present (Ohira *et al.*, 2014).

The possible phase transition of CaPv from cubic to a tetragonal structure at high pressure and temperature would also affect the physical properties of CaPv, for example the bulk modulus, shear modulus and possible transport properties (Karato, 1990). The partitioning of aluminum in the CaPv can be affected by water which might be used to study and constrain the deep water storage in the future.

6.5 Conclusion

The water solubility in the lower mantle has not been constrained well. Bridgmanite and ferropericlase in the lower mantle have little water solubility while possible hydrogen storage in the third most abundant mineral in the lower mantle–$CaSiO_3$ perovskite (CaPv) had not been studied. Herein, we reported the possible solubility of H_2O in CaPv inferred from high pressure infrared spectra and unit-cell parameters from X-ray diffraction. We synthesized CaPv from suolunite (10 wt% water), xonotlite (2.5 wt%) and $CaSiO_3$ glass + water at 19–120 GPa and 1400–2200 K as starting materials. In the water rich environment using suolunite and $CaSiO_3$ glass + water, we observed the tetragonal CaPv from X-ray diffraction, indicating that water could induce a phase transition or distortion of CaPv from the cubic to tetragonal structure even at high temperatures. From high pressure infrared spectra of the sample, about 0.5–1 wt% water might be stored in CaPv, making it a candidate for deep water storage. The bulk modulus for CaPv synthesized from water bearing environment is 231(2) GPa, which is smaller than the dry counterpart 255(5) GPa, supporting the existence of hydrogen in CaPv. We also conducted experiments on an

aluminum bearing $CaSiO_3$ glass starting material with water as a pressure medium where we observed the formation of δ–AlOOH together with CaPv at 60 GPa and 1400 K. CaPv could coexist with the potential hydrous phases in the mantle similar to the case for bridgmanite. Thus, the water solubility in the lower mantle would be determined from the maximum water content in nominally anhydrous mineral (NAM) for example, bridgmanite, ferropericlase, and CaPv. If the water content exceed the maximum water storage capacities of the lower mantle NAMs, hydrous minerals would be formed to hold the water.

REFERENCES

Adams, R. and R. Shriner, "Platinum oxide as a catalyst in the reduction of organic compounds. iii. preparation and properties of the oxide of platinum obtained by the fusion of chloroplatinic acid with sodium nitrate1", Journal of the American Chemical Society **45**, 9, 2171–2179 (1923).

Akahama, Y. and H. Kawamura, "Pressure calibration of diamond anvil Raman gauge to 310 GPa", Journal of Applied Physics **100**, 4, 043516 (2006).

Akber-Knutson, S., M. S. T. Bukowinski and J. Matas, "On the structure and compressibility of CaSiO3 perovskite", Geophys. Res. Lett. **29**, 3 (2002).

Altomare, A., R. Caliandro, M. Camalli, C. Cuocci, C. Giacovazzo, A. G. Moliterni and R. Rizzi, "Automatic structure determination from powder data with expo2004", Journal of Applied Crystallography **37**, 6, 1025–1028 (2004).

Andrault, D., R. J. Angel, J. L. Mosenfelder and T. L. Bihan, "Equation of state of stishovite to lower mantle pressures", American Mineralogist **88**, 2-3, 301–307 (2003).

Bercovici, D. and S.-i. Karato, "Whole-mantle convection and the transition-zone water filter", Nature **425**, 6953, 39–44 (2003).

Birch, F., "Finite elastic strain of cubic crystals", Physical Review **71**, 11, 809 (1947).

Birch, F., "Elasticity and constitution of the earth's interior", Journal of Geophysical Research **57**, 2, 227–286 (1952).

Blöchl, P. E., "Projector augmented-wave method", Physical review B **50**, 24, 17953 (1994).

Boehler, R., "Melting temperature of the earth's mantle and core: Earth's thermal structure", Annual Review of Earth and Planetary Sciences **24**, 1, 15–40 (1996).

Bolfan-Casanova, N., H. Keppler and D. C. Rubie, "Water partitioning between nominally anhydrous minerals in the MgO–SiO_2–H_2O system up to 24 GPa: implications for the distribution of water in the Earth's mantle", Earth and Planetary Science Letters **182**, 3-4, 209–221 (2000).

Bolfan-Casanova, N., H. Keppler and D. C. Rubie, "Water partitioning at 660 km depth and evidence for very low water solubility in magnesium silicate perovskite", Geophysical Research Letters **30**, 17 (2003).

Bolfan-Casanova, N., S. Mackwell, H. Keppler, C. McCammon and D. Rubie, "Pressure dependence of h solubility in magnesiowüstite up to 25 GPa: Implications for the storage of water in the Earth's lower mantle", Geophysical Research Letters **29**, 10 (2002).

Boulard, E., M. Harmand, F. Guyot, G. Lelong, G. Morard, D. Cabaret, S. Boccato, A. Rosa, R. Briggs and S. Pascarelli, "Ferrous iron under oxygen-rich conditions in the deep mantle", Geophysical Research Letters (2019).

Brown, J. and T. Shankland, "Thermodynamic parameters in the earth as determined from seismic profiles", Geophysical Journal International **66**, 3, 579–596 (1981a).

Brown, J. M. and T. J. Shankland, "Thermodynamic parameters in the earth as determined from seismic profiles", Geophys. J. Int. **66**, 3, 579–596 (1981b).

Bykova, E., M. Bykov, V. Prakapenka, Z. Konôpková, H.-P. Liermann, N. Dubrovinskaia and L. Dubrovinsky, "Novel high pressure monoclinic Fe_2O_3 polymorph revealed by single-crystal synchrotron X-ray diffraction studies", High Pressure Res. **33**, 3, 534–545 (2013).

Bykova, E., L. Dubrovinsky, N. Dubrovinskaia, M. Bykov, C. McCammon, S. Ovsyannikov, H.-P. Liermann, I. Kupenko, A. Chumakov, R. Rüffer *et al.*, "Structural complexity of simple Fe_2O_3 at high pressures and temperatures", Nat. Commun. **7**, 10661 (2016).

Caracas, R., R. Wentzcovitch, G. D. Price and J. Brodholt, "CaSiO3 perovskite at lower mantle pressures", Geophys. Res. Lett. **32**, 6, L06306 (2005).

Caracas, R. and R. M. Wentzcovitch, "Theoretical determination of the structures of CaSiO3 perovskites", Acta Crystallogr. B **62**, Pt 6, 1025–1030 (2006).

Catalli, K., S.-H. Shim, P. Dera, V. B. Prakapenka, J. Zhao, W. Sturhahn, P. Chow, Y. Xiao, H. Cynn and W. J. Evans, "Effects of the fe3 + spin transition on the properties of aluminous perovskite—new insights for lower-mantle seismic heterogeneities", Earth Planet. Sci. Lett. **310**, 3–4, 293–302 (2011).

Chen, H., S.-H. Shim, K. Leinenweber, V. Prakapenka, Y. Meng and C. Prescher, "Crystal structure of CaSiO3 perovskite at 28–62 GPa and 300 K under quasi-hydrostatic stress conditions", American Mineralogist: Journal of Earth and Planetary Materials **103**, 3, 462–468 (2018).

Chizmeshya, A. V. G., G. H. Wolf and P. F. McMillan, "First-principles calculation of the equation-of-state, stability, and polar optic modes of CaSiO3 perovskite", Geophys. Res. Lett. **23**, 20, 2725–2728 (1996).

Corma, A., M. Díaz-Cabañas, J. Jiang, M. Afeworki, D. Dorset, S. Soled and K. Strohmaier, "Extra-large pore zeolite (itq-40) with the lowest framework density containing double four-and double three-rings", Proceedings of the National Academy of Sciences **107**, 32, 13997–14002 (2010).

Cottaar, S., T. Heister, I. Rose and C. Unterborn, "Burnman: A lower mantle mineral physics toolkit", Geochemistry, Geophysics, Geosystems **15**, 4, 1164–1179 (2014a).

Cottaar, S., T. Heister, I. Rose and C. Unterborn, "BurnMan: A lower mantle mineral physics toolkit", Geochem. Geophys. Geosyst. **15**, 4, 1164–1179 (2014b).

Crowhurst, J. C., A. F. Goncharov, B. Sadigh, C. L. Evans, P. G. Morrall, J. L. Ferreira and A. Nelson, "Synthesis and characterization of the nitrides of platinum and iridium", Science **311**, 5765, 1275–1278 (2006).

Deng, J. and K. K. Lee, "Viscosity jump in the lower mantle inferred from melting curves of ferropericlase", Nature communications **8**, 1, 1997 (2017).

Dewaele, A., D. Agnès, L. Paul and M. Mohamed, "Equations of state of six metals above 94 GPa", Phys. Rev. B: Condens. Matter Mater. Phys. **70**, 9 (2004).

Dorfman, S. M., Y. Meng, V. B. Prakapenka and T. S. Duffy, "Effects of fe-enrichment on the equation of state and stability of (mg, fe) sio3 perovskite", Earth Planet. Sci. Lett. **361**, 249–257 (2013).

Dorogokupets, P. and A. Dewaele, "Equations of state of MgO, Au, Pt, NaCl-B1, and NaCl-B2: Internally consistent high-temperature pressure scales", High Pressure Research **27**, 4, 431–446 (2007).

Duffy, T. S., R. J. Hemley and H. Mao, "Equation of state and shear strength at multimegabar pressures: Magnesium oxide to 227 GPa", Phys. Rev. Lett. **74**, 8, 1371–1374 (1995).

Dyuzheva, T., L. Lityagina, N. Nikolaev, B. Martynov and N. Bendeliani, "Growth of single crystals of the high-pressure ϵ-FeOOH phase", Crystallogr. Rep. **51**, 2, 342–343 (2006).

Dziewonski, A. M. and D. L. Anderson, "Preliminary reference earth model", Physics of the Earth and Planetary Interiors **25**, 4, 297–356 (1981).

Eggleton, R. and A. Ringwood, "High pressure synthesis of a new aluminium silicate: Al5si5o17 (oh)", Geochemical Journal **12**, 3, 191–194 (1978).

Errandonea, D., R. Boehler, S. Japel, M. Mezouar and L. Benedetti, "Structural transformation of compressed solid Ar: An X-ray diffraction study to 114 GPa", Physical Review B **73**, 9, 092106 (2006).

Eysel, H. and S. Thym, "Raman spectra of peroxides", Zeitschrift für anorganische und allgemeine Chemie **411**, 2, 97–102 (1975).

Favre-Nicolin, V. and R. Černỳ, "Fox,free objects for crystallography': a modular approach to ab initio structure determination from powder diffraction", Journal of Applied Crystallography **35**, 6, 734–743 (2002).

Fei, H., D. Yamazaki, M. Sakurai, N. Miyajima, H. Ohfuji, T. Katsura and T. Yamamoto, "A nearly water-saturated mantle transition zone inferred from mineral viscosity", Science Advances **3**, 6, e1603024 (2017).

Fei, Y., H.-k. Mao and R. J. Hemley, "Thermal expansivity, bulk modulus, and melting curve of h2o–ice vii to 20 gpa", The Journal of chemical physics **99**, 7, 5369–5373 (1993).

Fei, Y., A. Ricolleau, M. Frank, K. Mibe, G. Shen and V. Prakapenka, "Toward an internally consistent pressure scale", Proc. Natl. Acad. Sci. U. S. A. **104**, 22, 9182–9186 (2007).

Fei, Y., Y. Wang and L. W. Finger, "Maximum solubility of FeO in (Mg,Fe)SiO_3-perovskite as a function of temperature at 26 GPa: Implication for FeO content in the lower mantle", Journal of Geophysical Research: Solid Earth **101**, B5, 11525–11530 (1996).

Frost, D. J., "The upper mantle and transition zone", Elements **4**, 3, 171–176 (2008).

Frost, D. J. and Y. Fei, "Stability of phase D at high pressure and high temperature", Journal of Geophysical Research: Solid Earth **103**, B4, 7463–7474 (1998).

Fukao, Y. and M. Obayashi, "Subducted slabs stagnant above, penetrating through, and trapped below the 660 km discontinuity", Journal of Geophysical Research: Solid Earth **118**, 11, 5920–5938 (2013).

Gleason, A., C. Quiroga, A. Suzuki, R. Pentcheva and W. Mao, "Symmetrization driven spin transition in ε-FeOOH at high pressure", Earth and Planetary Science Letters **379**, 49–55 (2013).

Gleason, A. E., R. Jeanloz and M. Kunz, "Pressure-temperature stability studies of FeOOH using X-ray diffraction", Am. Mineral. **93**, 11-12, 1882–1885 (2008).

Goncharov, A., V. Struzhkin, M. Somayazulu, R. Hemley and H. Mao, "Compression of ice to 210 gigapascals: Infrared evidence for a symmetric hydrogen-bonded phase", Science **273**, 5272, 218–220 (1996).

Gréaux, S., Y. Kono, Y. Wang, A. Yamada, C. Zhou, Z. Jing, T. Inoue, Y. Higo, T. Irifune, N. Sakamoto *et al.*, "Sound velocities of aluminum-bearing stishovite in the mantle transition zone", Geophysical Research Letters **43**, 9, 4239–4246 (2016).

Gréaux, S., N. Nishiyama, Y. Kono, L. Gautron, H. Ohfuji, T. Kunimoto, N. Menguy and T. Irifune, "Phase transformations of ca3al2si3o12 grossular garnet to the depths of the earth's mantle transition zone", Physics of the Earth and Planetary Interiors **185**, 3-4, 89–99 (2011).

Gurnis, M. and B. H. Hager, "Controls of the structure of subducted slabs", Nature **335**, 6188, 317 (1988).

Haines, J., J. Léger, M. Schmidt, J. Petitet, A. Pereira, J. Da Jornada and S. Hull, "Structural characterisation of the pa3-type, high pressure phase of ruthenium dioxide", Journal of Physics and Chemistry of Solids **59**, 2, 239–243 (1998).

Haines, J., J. Léger and O. Schulte, "Pa modified fluorite-type structures in metal dioxides at high pressure", Science **271**, 5249, 629–631 (1996).

Hirose, K., N. Takafuji, N. Sata and Y. Ohishi, "Phase transition and density of subducted morb crust in the lower mantle", Earth and Planetary Science Letters **237**, 1-2, 239–251 (2005a).

Hirose, K., N. Takafuji, N. Sata and Y. Ohishi, "Phase transition and density of subducted MORB crust in the lower mantle", Earth Planet. Sci. Lett. **237**, 1–2, 239–251 (2005b).

Hirschmann, M. M., "Water, melting, and the deep Earth H_2O cycle", Annu. Rev. Earth Planet. Sci. **34**, 629–653 (2006).

Hohenberg, P. and W. Kohn, "Inhomogeneous electron gas", Physical review **136**, 3B, B864 (1964).

Holmes, N. C., J. A. Moriarty, G. R. Gathers and W. J. Nellis, "The equation of state of platinum to 660 GPa (6.6 mbar)", J. Appl. Phys. **66**, 7, 2962 (1989).

Hu, Q., D. Y. Kim, J. Liu, Y. Meng, L. Yang, D. Zhang, W. L. Mao and H.-K. Mao, "Dehydrogenation of goethite in Earth's deep lower mantle", Proceedings of the National Academy of Sciences p. 201620644 (2017).

Hu, Q., D. Y. Kim, W. Yang, L. Yang, Y. Meng, L. Zhang and H.-K. Mao, "FeO_2 and FeOOH under deep lower-mantle conditions and Earth's oxygen–hydrogen cycles", Nature **534**, 7606, 241 (2016).

Inoue, T., H. Yurimoto and Y. Kudoh, "Hydrous modified spinel, mg1. 75sih0. 5o4: a new water reservoir in the mantle transition region", Geophysical Research Letters **22**, 2, 117–120 (1995).

Irifune, T., Y. Higo, T. Inoue, Y. Kono, H. Ohfuji and K. Funakoshi, "Sound velocities of majorite garnet and the composition of the mantle transition region", Nature **451**, 7180, 814 (2008).

Ismailova, L., E. Bykova, M. Bykov, V. Cerantola, C. McCammon, T. B. Ballaran, A. Bobrov, R. Sinmyo, N. Dubrovinskaia, K. Glazyrin *et al.*, "Stability of Fe, Al-bearing bridgmanite in the lower mantle and synthesis of pure Fe-bridgmanite", Sci. Adv. **2**, 7, e1600427 (2016).

Jackson, I., "Elasticity, composition and temperature of the Earth's lower mantle: a reappraisal", Geophysical Journal International **134**, 1, 291–311 (1998).

Jain, A. and S. P. Ong, "A. jain, sp ong, g. hautier, w. chen, wd richards, s. dacek, s. cholia, d. gunter, d. skinner, g. ceder, and ka persson, apl mater. 1, 011002 (2013).", APL Mater. **1**, 011002 (2013).

Jung, D. Y. and A. R. Oganov, "Ab initio study of the high-pressure behavior of CaSiO3 perovskite", Phys. Chem. Miner. **32**, 2, 146–153 (2005).

Kaminsky, F., "Mineralogy of the lower mantle: A review of "super-deep" mineral inclusions in diamond", Earth-Science Reviews **110**, 1-4, 127–147 (2012).

Kárason, H. and R. D. Van Der Hilst, "Constraints on mantle convection from seismic tomography", Geophysical Monograph **121**, 277–288 (2000).

Karato, S.-I., "The role of hydrogen in the electrical conductivity of the upper mantle", Nature **347**, 6290, 272 (1990).

Kavner, A. and T. S. Duffy, "Pressure–volume–temperature paths in the laser-heated diamond anvil cell", J. Appl. Phys. **89**, 3, 1907–1914 (2001).

Kawai, K. and T. Tsuchiya, "Small shear modulus of cubic CaSiO3 perovskite", Geophys. Res. Lett. **42**, 8, 2015GL063446 (2015).

Kesson, S., J. F. Gerald and J. Shelley, "Mineralogy and dynamics of a pyrolite lower mantle", Nature **393**, 6682, 252 (1998a).

Kesson, S. E., J. D. Fitz Gerald and J. M. Shelley, "Mineralogy and dynamics of a pyrolite lower mantle", Nature **393**, 6682, 252–255 (1998b).

Klotz, S., J.-C. Chervin, P. Munsch and G. L. Marchand, "Hydrostatic limits of 11 pressure transmitting media", J. Phys. D Appl. Phys. **42**, 7, 075413 (2009).

Kohlstedt, D., H. Keppler and D. Rubie, "Solubility of water in the α, β and γ phases of (mg, fe) 2 sio 4", Contributions to Mineralogy and Petrology **123**, 4, 345–357 (1996).

Kohn, S. C., L. Speich, C. B. Smith and G. P. Bulanova, "FTIR thermochronometry of natural diamonds: A closer look", Lithos **265**, 148–158 (2016).

Kohn, W. and L. J. Sham, "Self-consistent equations including exchange and correlation effects", Physical review **140**, 4A, A1133 (1965).

Komabayashi, T., K. Hirose, N. Sata, Y. Ohishi and L. S. Dubrovinsky, "Phase transition in CaSiO3 perovskite", Earth Planet. Sci. Lett. **260**, 3–4, 564–569 (2007).

Kresse, G., "G. kresse and d. joubert, phys. rev. b 59, 1758 (1999).", Phys. Rev. B **59**, 1758 (1999).

Kresse, G. and J. Furthmüller, "Efficient iterative schemes for ab initio total-energy calculations using a plane-wave basis set", Physical review B **54**, 16, 11169 (1996).

Kresse, G. and J. Hafner, "Ab initio molecular dynamics for liquid metals", Physical Review B **47**, 1, 558 (1993).

Kresse, G. *et al.*, "G. kresse and j. furthmüller, phys. rev. b 54, 11169 (1996).", Phys. Rev. B **54**, 11169 (1996).

Krukau, A. V., O. A. Vydrov, A. F. Izmaylov and G. E. Scuseria, "Influence of the exchange screening parameter on the performance of screened hybrid functionals", The Journal of Chemical Physics **125**, 22, 224106 (2006).

Kunz, M., A. A. MacDowell, W. A. Caldwell, D. Cambie, R. S. Celestre, E. E. Domning, R. M. Duarte, A. E. Gleason, J. M. Glossinger, N. Kelez *et al.*, "A beamline for high-pressure studies at the advanced light source with a superconducting bending magnet as the source", Journal of synchrotron radiation **12**, 5, 650–658 (2005).

Kurashina, T., K. Hirose, S. Ono, N. Sata and Y. Ohishi, "Phase transition in al-bearing CaSiO3 perovskite: implications for seismic discontinuities in the lower mantle", Phys. Earth Planet. Inter. **145**, 1–4, 67–74 (2004).

Kurnosov, A., H. Marquardt, D. Frost, T. B. Ballaran and L. Ziberna, "Evidence for a Fe^{3+}-rich pyrolitic lower mantle from (Al, Fe)-bearing bridgmanite elasticity data", Nature **543**, 7646, 543 (2017).

Lakshtanov, D. L., K. D. Litasov, S. V. Sinogeikin, H. Hellwig, J. Li, E. Ohtani and J. D. Bass, "Effect of Al^{3+} and H^{+} on the elastic properties of stishovite", American Mineralogist **92**, 7, 1026–1030 (2007a).

Lakshtanov, D. L., S. V. Sinogeikin, K. D. Litasov, V. B. Prakapenka, H. Hellwig, J. Wang, C. Sanches-Valle, J.-P. Perrillat, B. Chen, M. Somayazulu *et al.*, "The post-stishovite phase transition in hydrous alumina-bearing SiO_2 in the lower mantle of the Earth", Proceedings of the National Academy of Sciences **104**, 34, 13588–13590 (2007b).

Langreth, D. C. and J. P. Perdew, "Theory of nonuniform electronic systems. i. analysis of the gradient approximation and a generalization that works", Physical Review B **21**, 12, 5469 (1980).

Lee, K. K., B. O'Neill, W. R. Panero, S.-H. Shim, L. R. Benedetti and R. Jeanloz, "Equations of state of the high-pressure phases of a natural peridotite and implications for the earth's lower mantle", Earth and Planetary Science Letters **223**, 3-4, 381–393 (2004).

Léger, J., J. Haines and B. Blanzat, "Materials potentially harder than diamond: quenchable high-pressure phases of transition metal dioxides", Journal of materials science letters **13**, 23, 1688–1690 (1994).

Leinenweber, K. D., J. A. Tyburczy, T. G. Sharp, E. Soignard, T. Diedrich, W. B. Petuskey, Y. Wang and J. L. Mosenfelder, "Cell assemblies for reproducible multi-anvil experiments (the COMPRES assemblies)", American Mineralogist **97**, 2-3, 353–368 (2012).

Litasov, K. and E. Ohtani, "Phase relations and melt compositions in cmas–pyrolite–h2o system up to 25 gpa", Physics of the Earth and Planetary Interiors **134**, 1-2, 105–127 (2002).

Litvin, Y., A. Spivak, N. Solopova and L. Dubrovinsky, "On origin of lower-mantle diamonds and their primary inclusions", Physics of the Earth and Planetary Interiors **228**, 176–185 (2014).

Liu, J., Q. Hu, W. Bi, L. Yang, Y. Xiao, P. Chow, Y. Meng, V. B. Prakapenka, H.-K. Mao and W. L. Mao, "Altered chemistry of oxygen and iron under deep earth conditions", Nature Communications **10**, 1, 153 (2019).

Liu, J., Q. Hu, D. Y. Kim, Z. Wu, W. Wang, Y. Xiao, P. Chow, Y. Meng, V. B. Prakapenka, H.-K. Mao *et al.*, "Hydrogen-bearing iron peroxide and the origin of ultralow-velocity zones", Nature **551**, 7681, 494 (2017).

Liu, L.-G. and A. E. Ringwood, "Synthesis of a perovskite-type polymorph of CaSiO 3", Earth Planet. Sci. Lett. **28**, 2, 209–211 (1975).

Loubeyre, P., F. Occelli and R. LeToullec, "Optical studies of solid hydrogen to 320 gpa and evidence for black hydrogen", Nature **416**, 6881, 613 (2002).

Lu, C. and C. Chen, "High-pressure evolution of crystal bonding structures and properties of feooh", The journal of physical chemistry letters **9**, 9, 2181–2185 (2018).

Lundin, S., K. Catalli, J. Santillan, S.-H. Shim, V. B. Prakapenka, M. Kunz and Y. Meng, "Effect of fe on the equation of state of mantle silicate perovskite over 1mbar", Phys. Earth Planet. Inter. **168**, 1, 97–102 (2008).

Lundin, U., L. Fast, L. Nordström, B. Johansson, J. Wills and O. Eriksson, "Transition-metal dioxides with a bulk modulus comparable to diamond", Physical Review B **57**, 9, 4979 (1998).

Ma, Z., N. Shi, G. Mou and L. Liao, "Crystal structure refinement of suolunite and its significance to the cement techniques", Chinese Science Bulletin **44**, 23, 2125–2130 (1999).

Magyari-Köpe, B., L. Vitos, G. Grimvall, B. Johansson and J. Kollar, "Low-temperature crystal structure of CaSiO 3 perovskite: An ab initio total energy study", Phys. Rev. B: Condens. Matter Mater. Phys. **65**, 19, 193107 (2002).

Mao, H., P. Bell, J. t. Shaner and D. Steinberg, "Specific volume measurements of Cu, Mo, Pd, and Ag and calibration of the ruby R1 fluorescence pressure gauge from 0.06 to 1 Mbar", Journal of Applied Physics **49**, 6, 3276–3283 (1978).

Mao, H. K., L. C. Chen, R. J. Hemley, A. P. Jephcoat, Y. Wu and W. A. Bassett, "Stability and equation of state of CaSiO3-Perovskite to 134 GPa", J. Geophys. Res. [Solid Earth] **94**, B12, 17889–17894 (1989).

Marquardt, H. and L. Miyagi, "Slab stagnation in the shallow lower mantle linked to an increase in mantle viscosity", Nature Geoscience **8**, 4, 311 (2015).

Marquardt, H., S. Speziale, A. Gleason, S. Sinogeikin, I. Kantor and V. B. Prakapenka, "Brillouin scattering and x-ray diffraction of solid argon to 65 GPa and 700 k: Shear strength of argon at HP/HT", J. Appl. Phys. **114**, 9, 093517 (2013).

McDonough, W. F. and S.-S. Sun, "The composition of the Earth", Chemical geology **120**, 3-4, 223–253 (1995).

Meng, Y., X.-W. Liu, C.-F. Huo, W.-P. Guo, D.-B. Cao, Q. Peng, A. Dearden, X. Gonze, Y. Yang, J. Wang *et al.*, "When density functional approximations meet iron oxides", Journal of chemical theory and computation **12**, 10, 5132–5144 (2016).

Meng, Y., G. Shen and H. K. Mao, "Double-sided laser heating system at HPCAT for in situ x-ray diffraction at high pressures and high temperatures", J. Phys. Condens. Matter **18**, 25, S1097–103 (2006).

Michael, P. J., "The concentration, behavior and storage of H_2O in the suboceanic upper mantle: Implications for mantle metasomatism", Geochim. Cosmochim. Acta **52**, 2, 555–566 (1988).

Miura, H., Y. Hamada, T. Suzuki, M. Akaogi, N. Miyajima and K. Fujino, "Crystal structure of camg2al6o12, a new al-rich high pressure form", American Mineralogist **85**, 11-12, 1799–1803 (2000).

Monkhorst, H. J. and J. D. Pack, "Special points for brillouin-zone integrations", Physical Review B **13**, 12, 5188 (1976).

Moore Jr, W. J. and L. Pauling, "The crystal structures of the tetragonal monoxides of lead, tin, palladium, and platinum", Journal of the American Chemical Society **63**, 5, 1392–1394 (1941).

Moresi, L.-N. and V. Solomatov, "Numerical investigation of 2D convection with extremely large viscosity variations", Physics of Fluids **7**, 9, 2154–2162 (1995).

Muller, O. and R. Roy, "Formation and stability of the platinum and rhodium oxides at high oxygen pressures and the structures of Pt_3O_4, β-pto_2 and rho_2", Journal of the Less Common Metals **16**, 2, 129–146 (1968).

Murakami, M., "Post-perovskite phase transition and mineral chemistry in the pyrolitic lowermost mantle", Geophys. Res. Lett. **32**, 3 (2005).

Murakami, M., K. Hirose, K. Kawamura, N. Sata and Y. Ohishi, "Post-perovskite phase transition in mgsio3", Science **304**, 5672, 855–858 (2004).

Newville, M., A. Nelson, T. Stensitzki, A. Ingargiola, D. Allan, Y. Ram, C. Deil, G. Pasquevich, T. Spillane, P. A. Brodtkorb *et al.*, "LMFIT: non-linear least-square minimization and curve-fitting for python", Astrophysics Source Code Library (2016).

Newville, M., T. Stensitzki, D. Allen and A. Ingargiola, "Non-linear least-squares minimization and curve-fitting for python", Chicago, IL (2015).

Nishi, M., T. Irifune, S. Gréaux, Y. Tange and Y. Higo, "Phase transitions of serpentine in the lower mantle", Phys. Earth Planet. Inter. **245**, 52–58 (2015).

Nishi, M., T. Irifune, J. Tsuchiya, Y. Tange, Y. Nishihara, K. Fujino and Y. Higo, "Stability of hydrous silicate at high pressures and water transport to the deep lower mantle", Nature Geoscience **7**, 3, 224–227 (2014).

Nishi, M., Y. Kuwayama, J. Tsuchiya and T. Tsuchiya, "The pyrite-type high-pressure form of FeOOH", Nature **547**, 7662, 205 (2017).

Nishihara, Y. and K. N. Matsukage, "Iron-titanium oxyhydroxides as water carriers in the Earth's deep mantle", Am. Mineral. **101**, 4, 919–927 (2016).

Nisr, C., K. Leinenweber, V. Prakapenka, C. Prescher, S. Tkachev and S.-H. Dan Shim, "Phase transition and equation of state of dense hydrous silica up to 63 GPa", Journal of Geophysical Research: Solid Earth (2017a).

Nisr, C., S.-H. Shim, K. Leinenweber and A. Chizmeshya, "Raman spectroscopy of water-rich stishovite and dense high-pressure silica up to 55 GPa", American Mineralogist **102**, 11, 2180–2189 (2017b).

Noguchi, M., T. Komabayashi, K. Hirose and Y. Ohishi, "High-temperature compression experiments of CaSiO3 perovskite to lowermost mantle conditions and its thermal equation of state", Phys. Chem. Miner. **40**, 1, 81–91 (2013).

Ohira, I., E. Ohtani, T. Sakai, M. Miyahara, N. Hirao, Y. Ohishi and M. Nishijima, "Stability of a hydrous δ-phase, AlOOH–$MgSiO_2(OH)_2$, and a mechanism for water transport into the base of lower mantle", Earth and Planetary Science Letters **401**, 12–17 (2014).

Ohta, K., K. Hirose, T. Lay, N. Sata and Y. Ohishi, "Phase transitions in pyrolite and MORB at lowermost mantle conditions: Implications for a MORB-rich pile above the core–mantle boundary", Earth Planet. Sci. Lett. **267**, 1–2, 107–117 (2008).

Ohtani, E., "Hydrous minerals and the storage of water in the deep mantle", Chemical Geology **418**, 6–15 (2015).

Ono, S., Y. Ohishi, M. Isshiki and T. Watanuki, "In situ x-ray observations of phase assemblages in peridotite and basalt compositions at lower mantle conditions: Implications for density of subducted oceanic plate", J. Geophys. Res. [Solid Earth] **110**, B2 (2005).

Ono, S., Y. Ohishi and K. Mibe, "Phase transition of ca-perovskite and stability of al-bearing mg-perovskite in the lower mantle", Am. Mineral. **89**, 10, 1480–1485 (2004).

Palatinus, L. and G. Chapuis, "Superflip–a computer program for the solution of crystal structures by charge flipping in arbitrary dimensions", Journal of Applied Crystallography **40**, 4, 786–790 (2007).

Pamato, M. G., R. Myhill, T. B. Ballaran, D. J. Frost, F. Heidelbach and N. Miyajima, "Lower-mantle water reservoir implied by the extreme stability of a hydrous aluminosilicate", Nature Geoscience **8**, 1, 75–79 (2015).

Panero, W. R. and R. Caracas, "Stability of phase h in the $MgSiO_4H_2$–AlOOH–SiO_2 system", Earth and Planetary Science Letters **463**, 171–177 (2017).

Panero, W. R., J. S. Pigott, D. M. Reaman, J. E. Kabbes and Z. Liu, "Dry $(Mg,Fe)SiO_3$ perovskite in the Earth's lower mantle", Journal of Geophysical Research: Solid Earth **120**, 2, 894–908 (2015).

Paterson, M., "The determination of hydroxyl by infrared absorption in quartz, silicate glasses and similar materials", Bull Mineral **105**, 20–29 (1982).

Pawley, A. R., P. F. McMillan and J. R. Holloway, "Hydrogen in stishovite, with implications for mantle water content", Science **261**, 5124, 1024–1026 (1993).

Pearson, D., F. Brenker, F. Nestola, J. McNeill, L. Nasdala, M. Hutchison, S. Matveev, K. Mather, G. Silversmit, S. Schmitz *et al.*, "Hydrous mantle transition zone indicated by ringwoodite included within diamond", Nature **507**, 7491, 221–224 (2014).

Perdew, J. P., K. Burke and M. Ernzerhof, "Generalized gradient approximation made simple", Physical review letters **77**, 18, 3865 (1996).

Prakapenka, V., A. Kubo, A. Kuznetsov, A. Laskin, O. Shkurikhin, P. Dera, M. Rivers and S. Sutton, "Advanced flat top laser heating system for high pressure research at gsecars: application to the melting behavior of germanium", High Pressure Research **28**, 3, 225–235 (2008a).

Prakapenka, V. B., A. Kubo, A. Kuznetsov, A. Laskin, O. Shkurikhin, P. Dera, M. L. Rivers and S. R. Sutton, "Advanced flat top laser heating system for high pressure research at GSECARS: application to the melting behavior of germanium", High Press. Res. **28**, 3, 225–235 (2008b).

Prescher, C. and V. B. Prakapenka, "DIOPTAS: a program for reduction of two-dimensional X-ray diffraction data and data exploration", High Press. Res. **35**, 3, 223–230 (2015).

Putz, H., J. Schön and M. Jansen, "Combined method for ab initio structure solution from powder diffraction data", Journal of applied crystallography **32**, 5, 864–870 (1999).

Ranero, C. R., J. P. Morgan, K. McIntosh and C. Reichert, "Bending-related faulting and mantle serpentinization at the middle america trench", Nature **425**, 6956, 367 (2003).

Range, K.-J., F. Rau, U. Klement and A. Heyns, "β-pto_2: High pressure synthesis of single crystals and structure refinement", Materials research bulletin **22**, 11, 1541–1547 (1987).

Richard, G., M. Monnereau and J. Ingrin, "Is the transition zone an empty water reservoir? inferences from numerical model of mantle dynamics", Earth and Planetary Science Letters **205**, 1-2, 37–51 (2002).

Ricolleau, A., Y. Fei, E. Cottrell, H. Watson, L. Deng, L. Zhang, G. Fiquet, A.-L. Auzende, M. Roskosz, G. Morard *et al.*, "Density profile of pyrolite under the lower mantle conditions", Geophysical Research Letters **36**, 6 (2009).

Ricolleau, A., J.-P. Perrillat, G. Fiquet, I. Daniel, J. Matas, A. Addad, N. Menguy, H. Cardon, M. Mezouar and N. Guignot, "Phase relations and equation of state of a natural MORB: Implications for the density profile of subducted oceanic crust in the earth's lower mantle", J. Geophys. Res. **115**, B8, B08202 (2010).

Ringwood, A. E., "Composition and petrology of the earth's mantle", MacGraw-Hill **618** (1975).

Rivers, M., V. B. Prakapenka, A. Kubo, C. Pullins, C. M. Holl and S. D. Jacobsen, "The COMPRES/GSECARS gas-loading system for diamond anvil cells at the Advanced Photon Source", High Press. Res. **28**, 3, 273–292 (2008).

Ross, N. L. and R. M. Hazen, "High-pressure crystal chemistry of $MgSiO_3$ perovskite", Physics and Chemistry of Minerals **17**, 3, 228–237 (1990).

Rossman, G., "Studies of OH in nominally anhydrous minerals", Physics and Chemistry of Minerals **23**, 4-5, 299–304 (1996).

Salamat, A., A. L. Hector, P. Kroll and P. F. McMillan, "Nitrogen-rich transition metal nitrides", Coordination Chemistry Reviews **257**, 13-14, 2063–2072 (2013).

Sano, A., E. Ohtani, T. Kondo, N. Hirao, T. Sakai, N. Sata, Y. Ohishi and T. Kikegawa, "Aluminous hydrous mineral δ-AlOOH as a carrier of hydrogen into the core-mantle boundary", Geophysical Research Letters **35**, 3 (2008).

Sano, A., E. Ohtani, T. Kubo and K.-i. Funakoshi, "In situ X-ray observation of decomposition of hydrous aluminum silicate $AlSiO_3OH$ and aluminum oxide hydroxide d-AlOOH at high pressure and temperature", Journal of Physics and Chemistry of Solids **65**, 8, 1547–1554 (2004).

Schmandt, B., S. D. Jacobsen, T. W. Becker, Z. Liu and K. G. Dueker, "Dehydration melting at the top of the lower mantle", Science **344**, 6189, 1265–1268 (2014).

Shaw, S., S. Clark and C. Henderson, "Hydrothermal formation of the calcium silicate hydrates, tobermorite (ca5si6o16 (oh) 2· 4h2o) and xonotlite (ca6si6o17 (oh) 2): an in situ synchrotron study", Chemical Geology **167**, 1-2, 129–140 (2000).

Shim, S.-H., "PeakPo - A python software for X-ray diffraction analysis at high pressure and high temperature", URL `https://doi.org/10.5281/zenodo.810200` (2017).

Shim, S.-H., A. Bengtson, D. Morgan, W. Sturhahn, K. Catalli, J. Zhao, M. Lerche and V. Prakapenka, "Electronic and magnetic structures of the postperovskite-type Fe_2O_3 and implications for planetary magnetic records and deep interiors", Proc. Natl. Acad. Sci. **106**, 14, 5508–5512 (2009).

Shim, S.-H., T. S. Duffy and G. Shen, "The stability and P–V–T equation of state of $CaSiO_3$ perovskite in the Earth's lower mantle", Journal of Geophysical Research: Solid Earth **105**, B11, 25955–25968 (2000a).

Shim, S.-H., T. S. Duffy and G. Shen, "The stability and P-V-T equation of state of CaSiO 3 perovskite in the earth's lower mantle", J. Geophys. Res. **105**, 25, 955–925 (2000b).

Shim, S.-H., T. S. Duffy and G. Shen, "The post-spinel transformation in Mg_2SiO_4 and its relation to the 660-km seismic discontinuity", Nature **411**, 6837, 571 (2001).

Shim, S.-H., B. Grocholski, Y. Ye, E. E. Alp, S. Xu, D. Morgan, Y. Meng and V. B. Prakapenka, "Stability of ferrous-iron-rich bridgmanite under reducing midmantle conditions", Proceedings of the National Academy of Sciences **114**, 25, 6468–6473 (2017).

Shim, S.-H., R. Jeanloz and T. S. Duffy, "Tetragonal structure of CaSiO3 perovskite above 20 GPa", Geophys. Res. Lett. **29**, 24, 2166 (2002).

Shirako, Y., X. Wang, Y. Tsujimoto, K. Tanaka, Y. Guo, Y. Matsushita, Y. Nemoto, Y. Katsuya, Y. Shi and D. Mori, "Synthesis, crystal structure, and electronic properties of high-pressure pdf2-type oxides mo2 (m= ru, rh, os, ir, pt)", Inorganic Chemistry **53**, 21, 11616–11625 (2014).

Smyth, J., D. Frost, F. Nestola, C. Holl and G. Bromiley, "Olivine hydration in the deep upper mantle: effects of temperature and silica activity", Geophysical Research Letters **33**, 15 (2006).

Smyth, J. R., "A crystallographic model for hydrous wadsleyite (β-Mg_2SiO_4): An ocean in the Earth's interior?", American Mineralogist **79**, 021–1024 (1994).

Smyth, J. R., C. M. Holl, D. J. Frost, S. D. Jacobsen, F. Langenhorst and C. A. Mccammon, "Structural systematics of hydrous ringwoodite and water in Earth's interior", American Mineralogist **88**, 10, 1402–1407 (2003).

Soulard, C., X. Rocquefelte, P.-E. Petit, M. Evain, S. Jobic, J.-P. Itie, P. Munsch, H.-J. Koo and M.-H. Whangbo, "Experimental and theoretical investigation on the relative stability of the pds_2-and pyrite-type structures of $pdse_2$", Inorganic Chemistry **43**, 6, 1943–1949 (2004).

Spektor, K., J. Nylen, R. Mathew, M. Edén, E. Stoyanov, A. Navrotsky, K. Leinenweber and U. Häussermann, "Formation of hydrous stishovite from coesite in high-pressure hydrothermal environments", American Mineralogist **101**, 11, 2514–2524 (2016a).

Spektor, K., J. Nylén, R. Mathew, M. Edén, E. Stoyanov, A. Navrotsky, K. Leinenweber and U. Häussermann, "Formation of hydrous stishovite from coesite in high pressure hydrothermal environments", **101**, 2514–2524 (2016b).

Spektor, K., J. Nylen, E. Stoyanov, A. Navrotsky, R. L. Hervig, K. Leinenweber, G. P. Holland and U. Häussermann, "Ultrahydrous stishovite from high-pressure hydrothermal treatment of SiO_2", Proceedings of the National Academy of Sciences **108**, 52, 20918–20922 (2011).

Stachel, T., G. P. Brey and J. W. Harris, "Inclusions in sublithospheric diamonds: glimpses of deep Earth", Elements **1**, 2, 73–78 (2005).

Stixrude, L., R. E. Cohen, R. Yu and H. Krakauer, "Prediction of phase transition in CaSiO3 perovskite and implications for lower mantle structure", Am. Mineral. **81**, 9, 1293–1296 (1996a).

Stixrude, L., R. E. Cohen, R. Yu and H. Krakauer, "Prediction of phase transition in casio3 perovskite and implications for lower mantle structure", (1996b).

Stixrude, L. and C. Lithgow-Bertelloni, "Thermodynamics of mantle minerals–I. physical properties", Geophysical Journal International **162**, 2, 610–632 (2005).

Stixrude, L. and C. Lithgow-Bertelloni, "Thermodynamics of mantle minerals-II. phase equilibria", Geophys. J. Int. **184**, 3, 1180–1213 (2011).

Stixrude, L., C. Lithgow-Bertelloni, B. Kiefer and P. Fumagalli, "Phase stability and shear softening in ca si O 3 perovskite at high pressure", Phys. Rev. B: Condens. Matter Mater. Phys. **75**, 2, 024108 (2007).

Sturhahn, W., "Conuss and phoenix: Evaluation of nuclear resonant scattering data", Hyperfine Interactions **125**, 1-4, 149–172 (2000).

Syracuse, E. M., P. E. van Keken and G. A. Abers, "The global range of subduction zone thermal models", Physics of the Earth and Planetary Interiors **183**, 1-2, 73–90 (2010).

Tamai, H. and T. Yagi, "High-pressure and high-temperature phase relations in CaSiO 3 and CaMgSi 2 O 6 and elasticity of perovskite-type CaSiO 3", Phys. Earth Planet. Inter. **54**, 3, 370–377 (1989).

Tanaka, M., T. Shishido, H. Horiuchi, N. Toyota, D. Shindo and T. Fukuda, "Structure studies of CeAlO 3", J. Alloys Compd. **192**, 1, 87–89 (1993).

Tangeman, J. A., B. L. Phillips, A. Navrotsky, J. K. R. Weber, A. D. Hixson and T. S. Key, "Vitreous forsterite (Mg2SiO4): Synthesis, structure, and thermochemistry", Geophys. Res. Lett. **28**, 13, 2517–2520 (2001).

Toby, B. H., "EXPGUI, a graphical user interface for GSAS", J. Appl. Crystallogr. **34**, 2, 210–213 (2001).

Toby, B. H. and R. B. Von Dreele, "GSAS-II: the genesis of a modern open-source all purpose crystallography software package", Journal of Applied Crystallography **46**, 2, 544–549 (2013).

Tschauner, O., S. Huang, E. Greenberg, V. Prakapenka, C. Ma, G. Rossman, A. Shen, D. Zhang, M. Newville, A. Lanzirotti *et al.*, "Ice-VII inclusions in diamonds: Evidence for aqueous fluid in Earth's deep mantle", Science **359**, 6380, 1136–1139 (2018).

Tse, J., D. Klug, K. Uehara, Z. Li, J. Haines and J. Leger, "Elastic properties of potential superhard phases of ruo_2", Physical Review B **61**, 15, 10029 (2000).

Tsuchiya, J. and T. Tsuchiya, "First-principles prediction of a high-pressure hydrous phase of alooh", Physical Review B **83**, 5, 054115 (2011).

Tsuchiya, J., T. Tsuchiya and R. M. Wentzcovitch, "Vibrational properties of δ-alooh under pressure", American Mineralogist **93**, 2-3, 477–482 (2008).

Uchida, T., Y. Wang, N. Nishiyama, K.-I. Funakoshi, H. Kaneko, A. Nozawa, R. B. Von Dreele, M. L. Rivers, S. R. Sutton, A. Yamada and Others, "Non-cubic crystal symmetry of CaSiO 3 perovskite up to 18 GPa and 1600 K", Earth Planet. Sci. Lett. **282**, 1, 268–274 (2009).

van Keken, P. E., B. R. Hacker, E. M. Syracuse and G. A. Abers, "Subduction factory: 4. depth-dependent flux of H_2O from subducting slabs worldwide", Journal of Geophysical Research: Solid Earth **116**, B1 (2011).

Vinet, P., J. H. Rose, J. Ferrante and J. R. Smith, "Universal features of the equation of state of solids", J. Phys. Condens. Matter **1**, 11, 1941 (1989).

Vogt, H., T. Chattopadhyay and H. Stolz, "Complete first-order raman spectra of the pyrite structure compounds fes2, mns2 and sip2", Journal of Physics and Chemistry of Solids **44**, 9, 869–873 (1983).

Walter, M., A. Thomson, W. Wang, O. Lord, J. Ross, S. McMahon, M. Baron, E. Melekhova, A. Kleppe and S. Kohn, "The stability of hydrous silicates in Earth's lower mantle: Experimental constraints from the systems MgO–SiO_2–H_2O and MgO–Al_2O_3–SiO_2–H_2O", Chemical Geology **418**, 16–29 (2015).

Wang, Y., D. J. Weidner and F. Guyot, "Thermal equation of state of CaSiO3 perovskite", J. Geophys. Res. **101**, B1, 661–672 (1996).

Waszek, L., N. C. Schmerr and M. D. Ballmer, "Global observations of reflectors in the mid-mantle with implications for mantle structure and dynamics", Nature communications **9**, 1, 385 (2018).

Weerasinghe, G. L., C. J. Pickard and R. Needs, "Computational searches for iron oxides at high pressures", Journal of Physics: Condensed Matter **27**, 45, 455501 (2015).

Weidner, D. J., J. D. Bass, A. Ringwood and W. Sinclair, "The single-crystal elastic moduli of stishovite", Journal of Geophysical Research: Solid Earth **87**, B6, 4740–4746 (1982).

Wessel, M. and R. Dronskowski, "Nature of n- n bonding within high-pressure noble-metal pernitrides and the prediction of lanthanum pernitride", Journal of the American Chemical Society **132**, 7, 2421–2429 (2010).

Wittlinger, J., R. Fischer, S. Werner, J. Schneider and H. Schulz, "High-pressure study of hcp-argon", Acta Crystallographica Section B: Structural Science **53**, 5, 745–749 (1997).

Wolanin, E., P. Pruzan, J. Chervin, B. Canny, M. Gauthier, D. Häusermann and M. Hanfland, "Equation of state of ice VII up to 106 gpa", Phys. Rev. B **56**, 10, 5781 (1997).

Wolf, A. S., J. M. Jackson, P. Dera and V. B. Prakapenka, "The thermal equation of state of (mg, fe) sio3 bridgmanite (perovskite) and implications for lower mantle structures", Journal of Geophysical Research: Solid Earth **120**, 11, 7460–7489 (2015).

Ye, Y., D. A. Brown, J. R. Smyth, W. R. Panero, S. D. Jacobsen, Y.-Y. Chang, J. P. Townsend, S.-M. Thomas, E. H. Hauri, P. Dera *et al.*, "Compressibility and thermal expansion of hydrous ringwoodite with 2.5 (3) wt% H_2O", American Mineralogist **97**, 4, 573–582 (2012).

Ye, Y., V. Prakapenka, Y. Meng and S.-H. Shim, "Intercomparison of the gold, platinum, and Mgo pressure scales up to 140 GPa and 2500 K", Journal of Geophysical Research: Solid Earth **122**, 5, 3450–3464 (2017).

Ye, Y., J. R. Smyth, A. Hushur, M. H. Manghnani, D. Lonappan, P. Dera and D. J. Frost, "Crystal structure of hydrous wadsleyite with 2.8% H_2O and compressibility to 60 GPa", American Mineralogist **95**, 11-12, 1765–1772 (2010).

Yuan, L., E. Ohtani, D. Ikuta, S. Kamada, J. Tsuchiya, H. Naohisa, Y. Ohishi and A. Suzuki, "Chemical reactions between fe and h2o up to megabar pressures and implications for water storage in the earth's mantle and core", Geophysical Research Letters **45**, 3, 1330–1338 (2018).

Zhang, L., Y. Meng, W. Yang, L. Wang, W. L. Mao, Q.-S. Zeng, J. S. Jeong, A. J. Wagner, K. A. Mkhoyan, W. Liu *et al.*, "Disproportionation of (Mg, Fe) SiO_3 perovskite in Earth's deep lower mantle", Science **344**, 6186, 877–882 (2014).

Zhang, L., H. Yuan, Y. Meng and H.-K. Mao, "Discovery of a hexagonal ultradense hydrous phase in (Fe, Al) OOH", Proc. Natl. Acad. Sci. p. 201720510 (2018).

Zhang, Y., D. Zhao, M. Matsui and G. Guo, "Equations of state of CaSiO3 perovskite: a molecular dynamics study", Phys. Chem. Miner. **33**, 2, 126–137 (2006).

Zhao, Z., B. Xu and Y. Tian, "Recent advances in superhard materials", Annual Review of Materials Research **46**, 383–406 (2016).

Zhu, S.-c., Q. Hu, W. L. Mao, H.-k. Mao and H. Sheng, "Hydrogen-bond symmetrization breakdown and dehydrogenation mechanism of feo_2h at high pressure", Journal of the American Chemical Society **139**, 35, 12129–12132 (2017).